

DISSOLUTION KINETICS OF WIDMANSTATTEN Ag_2Al PRECIPITATES

by

KWESI KURENTSIR SAGOE-CRENTSIL

B.Sc., University of Science and Technology, Ghana, 1978

A THESIS SUBMITTED IN PARTIAL FULFILMENT OF
THE REQUIREMENTS FOR THE DEGREE OF
MASTER OF SCIENCE

in

THE FACULTY OF GRADUATE STUDIES
Department of Metallurgical Engineering

We accept this thesis as conforming
to the required standard

THE UNIVERSITY OF BRITISH COLUMBIA

May 1983

© Kwasi Kurentsir Sagoe-Crentsil, 1983

In presenting this thesis in partial fulfilment of the requirements for an advanced degree at the University of British Columbia, I agree that the Library shall make it freely available for reference and study. I further agree that permission for extensive copying of this thesis for scholarly purposes may be granted by the head of my department or by his or her representatives. It is understood that copying or publication of this thesis for financial gain shall not be allowed without my written permission.

Department of METALLURGICAL ENGINEERING

The University of British Columbia
1956 Main Mall
Vancouver, Canada
V6T 1Y3

Date May 20/1983

ABSTRACT

A combination of SEM and electron-probe studies have been conducted on the dissolution of Widmanstätten $\gamma(\text{Ag}_2\text{Al})$ plates in Al-15.3 wt.% Ag between the temperatures 458°C and 494°C. Individual rather than averaged kinetic events have been monitored in all cases. The mechanism of dissolution observed at the plate tip was found to be different from that operative at the broadface. Precipitates shorten linearly at volume diffusion controlled rates according to the Horvay-Cahn, Zener-Hillert and Jones-Trivedi analyses, adapted for the case of dissolution. The kinetics of thinning were observed to be two orders of magnitude slower than volume diffusion controlled rates, indicating an interface-controlled reaction. This interfacial inhibition has further been confirmed by the consistent fall of the interface concentration value below equilibrium solubility values as determined from the electron probe measurements. The electron probe measurements give similar diffusion distances at the tip and broadface and would require short circuit diffusion from the tip to the broadface to be in agreement with the kinetic results. A mechanism to explain the overall reaction has been proposed.

TABLE OF CONTENTS

	<u>Page</u>
Abstract	ii
Table of Contents	iii
List of Tables	v
List of Figures	vi
Acknowledgement	ix
 1. INTRODUCTION	 1
1.1 Mechanism of Dissolution	1
1.2 The Widmanstatten Structure	7
1.3 Experimental Studies on the Dissolution of Widmanstatten Precipitates	 7
1.3.1 Electron Probe Studies	9
1.3.2 Kinetic Studies	10
1.4 Aim of Present Investigation	11
2. EXPERIMENTAL PROCEDURE	12
2.1 Choice of System	12
2.2 Preparation of the Master Alloy.....	12
2.3 Specimen Preparation	14
2.4 SEM : Single Precipitate Measurements	19
2.4.1 Shortening Kinetics	20
2.4.2 Thinning Kinetics	20
2.5 SEM : Population Study	21
2.6 Electron Probe Microanalysis Profiles	22
2.6.1 Tip Profile	23
2.6.2 Broadface and Isoconcentrate Profiles	25
3. RESULTS	26
3.1 Kinetics of Shortening	26
3.1.1 Results	26

	<u>Page</u>
3.1.2 Analysis of Results	29
3.2 Shape Changes and Statistical Analysis of Shortening.	36
3.3 Thinning Kinetics	41
3.4 Electron-probe Microanalysis	46
3.4.1 Introduction	46
3.4.2 Broadface Profile	48
3.4.3 Tip Profile	58
3.4.4 Isoconcentrate Contours	61
4. SUMMARY AND DISCUSSION OF RESULTS	65
4.1 Introduction	65
4.2 Physical Mechanism of Interface Migration -	
The Ledge Theory	70
4.3 Kinetics of Dissolution of $\gamma(\text{Ag}_2\text{Al})$ -	
The Ledge Mechanism	76
4.4 Overall Mechanism of Dissolution	78
5. CONCLUSIONS	81
BIBLIOGRAPHY	83
APPENDIX I Results of Kinetic Measurements : Shortening	86
APPENDIX II Results of Kinetic Measurements : Thinning	92
APPENDIX III Solute Balance Calculation	97

LIST OF TABLES

<u>Table</u>	<u>Page</u>
I Morphology Classification and Relationship to Boundary Misorientation	3
II Compilation of Single Precipitate Results : Shortening .	28
III Comparison of Calculated Mean Diffusivities : Shortening	33
IV Population Kinetics Results	41
V Compilation of Single Precipitate Results : Thinning ...	45
VI Comparison of Calculated Diffusivities : Thinning	47
VII Electron-probe Determination of Interface Concentration (C_I) and Volume Diffusion Coefficients (D_V) for the Broadface	56

LIST OF FIGURES

<u>Figure</u>	<u>Page</u>
1 Schematic phase diagram illustrating precipitation of one solid phase from another	2
2(a) Section of an equilibrium phase diagram showing T_G and T_D for an alloy of composition Co	5
(b) Dissolution composition profile for an alloy of composition Co	5
(c) Composition profile for an interface controlled dissolution reaction	6
(d) Profile for mixed control dissolution	6
3 Ag-Al binary diagram	13
4 Microstructure of the equilibrated Al-Ag alloy	16
5 Population distribution curve for Widmanstatten plates of varying Aspect Ratio	17
6 Optical micrograph of a typical Widmanstatten plate, with contamination marks showing a broadface and tip scan	24
7 Linear time plot of shortening kinetics at 485°C	27
8 Schematic drawing of the steady-state diffusion field near a Widmanstatten precipitate tip according to	
(a) the Horvay-Cahn model	30
(b) the Zener-Hillert model	30
(c) the Jones-Trivedi model	30

<u>Figure</u>		<u>Page</u>
9	Arrhenius plot of D_V (Zener-Hillert) versus $\frac{1}{T}$ (K^{-1}) for dissolving Ag_2Al plates	37
10	Secondary electron image micrographs used to observe shape changes and population shortening kinetics at 466°C	38
11	Shortening kinetics ($ay/2$ -vs- t) for SEM population study	40
12	Secondary electron image of thinning sequence at 485°C.	42
13	Linear time plot of thinning kinetics at 485°C	43
14	Parabolic time plot of thinning kinetics at 485°C	44
15	Concentration profiles on both sides of two precipi- tates dissolved at 485°C for 10 minutes	49
16	Interface concentration C_I versus \sqrt{Dt} at 485°C	51
17	C versus $\text{erf } \frac{x}{2\sqrt{Dt}}$ at 485°C	53
18	Probability plot of $\frac{C(x,t)-C_M}{C_I-C_M}$ versus diffusion distance, x	54
19	Schematic diagram for the flux balance calculation	57
20	Comparison of experimental and calculated (Horvay- Cahn) profile for a tip (solution treated at 485°C for 10 minutes)	59
21	Isoconcentration contours at 485°C and 474°C	62
22	Schematic diagram for solute conservation calculation .	63

<u>Figure</u>		<u>Page</u>
23	Schematic concentration profiles associated with dissolving Ag_2Al precipitates	
(a)	experimentally observed profile	68
(b)	predicted from kinetic measurements - Dumbbell shaped	69
(c)	due to the point effect of diffusion - spheroidal shaped	69
24	Schematic representation of	
(a)	semi-coherent interface containing some dislocations and some strain	71
(b)	coherent interface maintained by elastic strain ..	71
(c)	semi-coherent boundary migrating from XY to X'Y' showing A atoms(•) lodging in the interstices of B	73
25	Growth of lower cph phase from upper fcc by random atomic jumps	75
26	Ledge structure at the edge of a precipitate	77
III-1	Schematic diagram of partially dissolved precipitate and surrounding solute distribution	98
III-2	Schematic diagram of solute distribution profile (485°C/10 minutes)	99
III-3	Solute distribution profiles representing the corners of Fig. III-1	100

ACKNOWLEDGEMENT

I am greatly indebted to Dr. L. C. Brown for the help and guidance throughout this work, and much more for his encouragement which I so often needed.

Thanks are also due to Dr. E. B. Hawbolt for his criticism and suggestions on the final draft of this thesis.

The assistance of the technical staff and in particular that of Miss Mary Mager is greatly appreciated.

The graduate fellowship awarded by the University of British Columbia is gratefully appreciated.

1. INTRODUCTION

Precipitation reactions can occur whenever a single phase material is heated or cooled to a temperature at which a second phase becomes stable (Fig. 1). Precipitation of the new second phase may proceed in a variety of ways as in the aging, massive or proeutectoid decomposition reactions. However only a few distinct precipitate shapes occur and these are listed in Table I.^{1,2} The main shapes are allotriomorphs which form only at grain boundaries and Widmanstätten precipitates which can form either at grain boundaries or, more commonly, in grain interiors. Other precipitate shapes such as sawteeth, idiomorphs and massive structures occur less often.

The kinetics of transformation as well as the interfacial structure of the precipitates have been extensively investigated for specific transformations in several systems. Most of the kinetic studies have been of precipitate growth. The corresponding case of precipitate dissolution has been much less studied. As yet very little is known about the mechanism of dissolution of Widmanstätten plates which forms the basis of this work.

1.1 Mechanism of Dissolution

The process of dissolution involves mass transport from the dissolving second phase to the stable matrix phase.

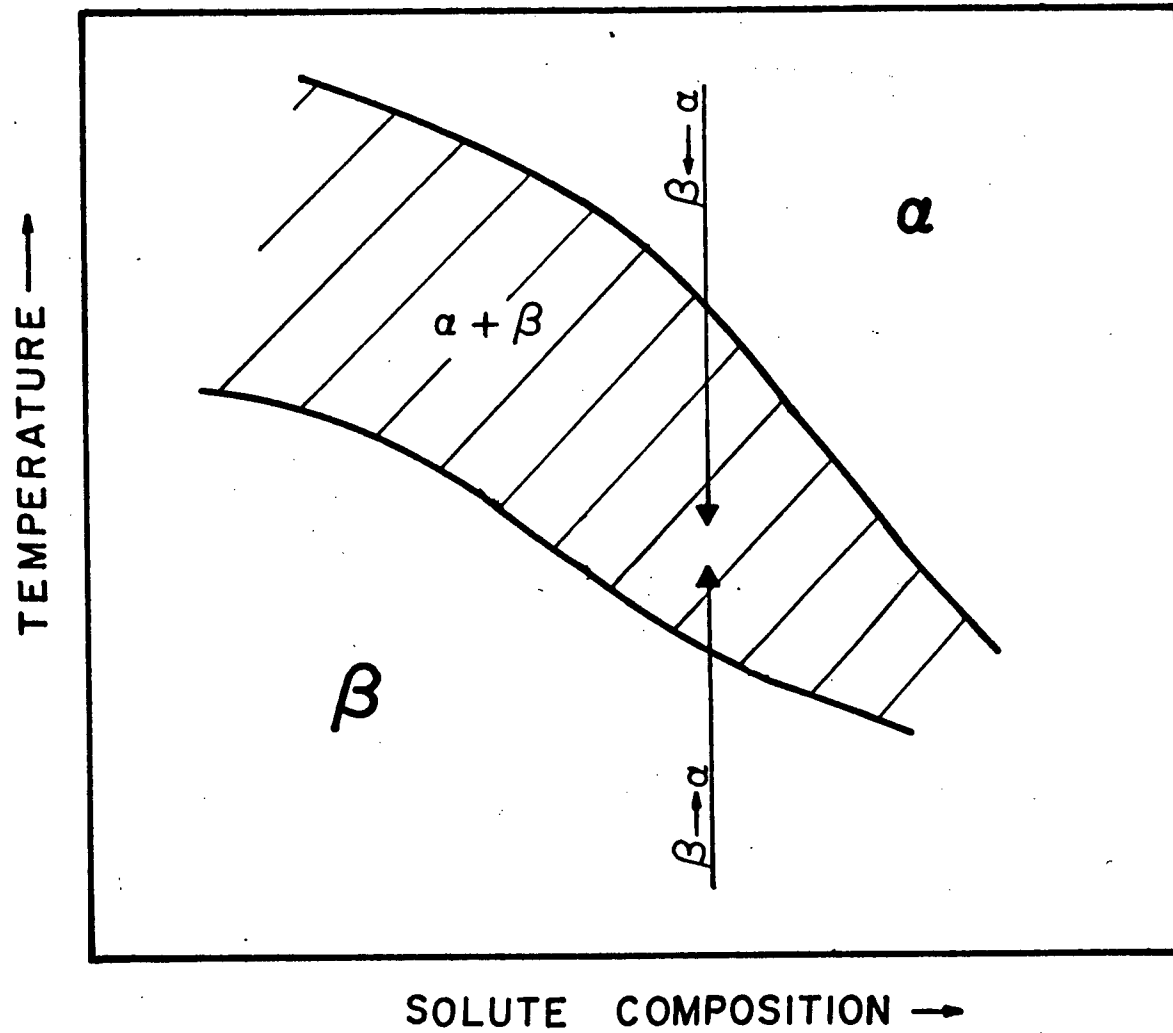



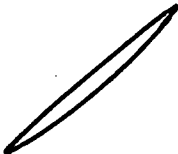

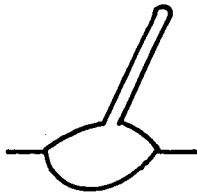



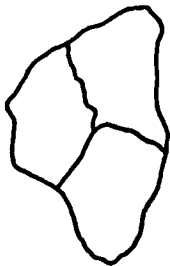


Fig. 1. Schematic phase diagram illustrating precipitation of one solid phase from another.

Table I. The Dube Morphological Classification System.^{1,2}

	Grain Boundary Allotriomorphs	Widmanstatten			Idiomorphs	Massive
		Intra-granular	Primary and Secondary Sideplates	Primary and Secondary Sawteeth		
Morphology	  		 	 		

The dissolution composition profile for an alloy of composition C_0 , after instantaneous heating from T_G to T_D is depicted in Fig. 2.

For a transformation involving long-range solute transport, as in the case above, the diffusion field adjacent to the precipitate can be described by a solution to the field equation:

$$D \nabla^2 C = \frac{\delta C}{\delta t} \quad \dots 1$$

where C is the concentration of solute in the matrix and it is assumed $D \neq D(C)$. The applicable boundary conditions need also be specified. The interface boundary condition is of particular interest in this study.

Consider the case of a constant interphase boundary composition (C_I). In this case, chemical equilibrium exists between the compositions of the two phases in contact with each other, and the reaction is controlled by the volume diffusion of solute through the matrix. Thus the interphase composition is predictable from the corresponding phase diagram and local equilibrium conditions are said to exist.

The assumption of local equilibrium is one limiting form of this boundary condition. The other limiting form is for a sluggish interface, in which case the concentration near the boundary C_I is almost equal to C_M , the initial matrix composition Fig.2(c). The solute flux J across the

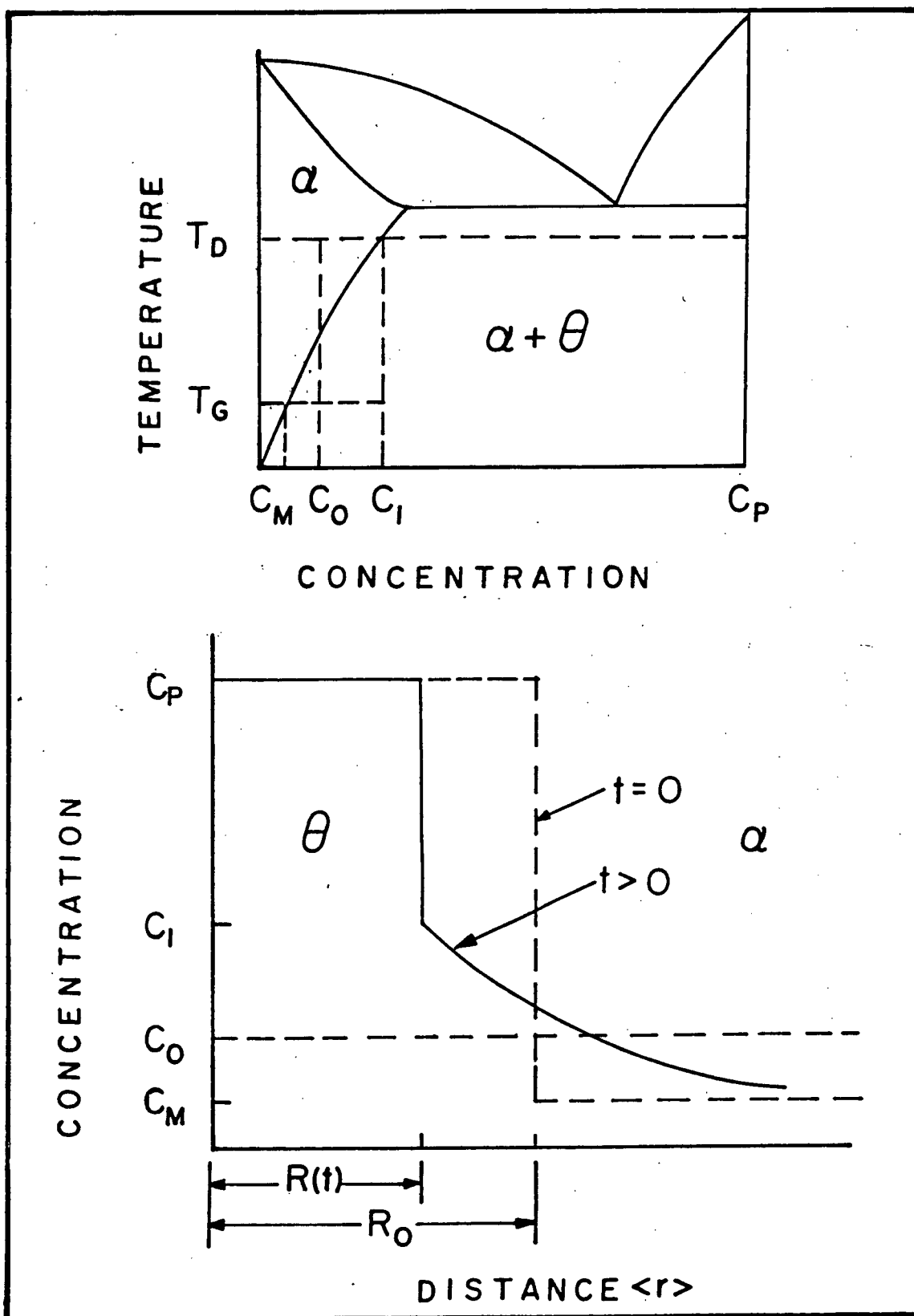


Fig. 2(a). Section of an equilibrium phase diagram showing T_G and T_D for an alloy of composition C_O .

2(b). Dissolution composition profile for an alloy of composition C_O .

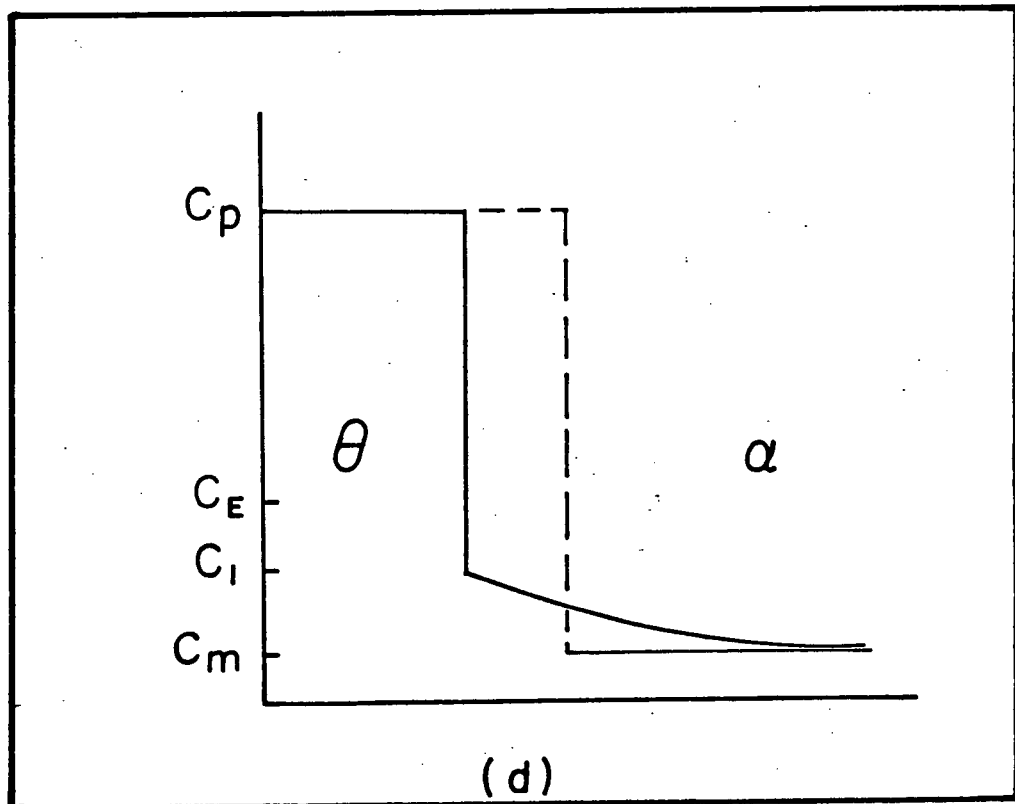
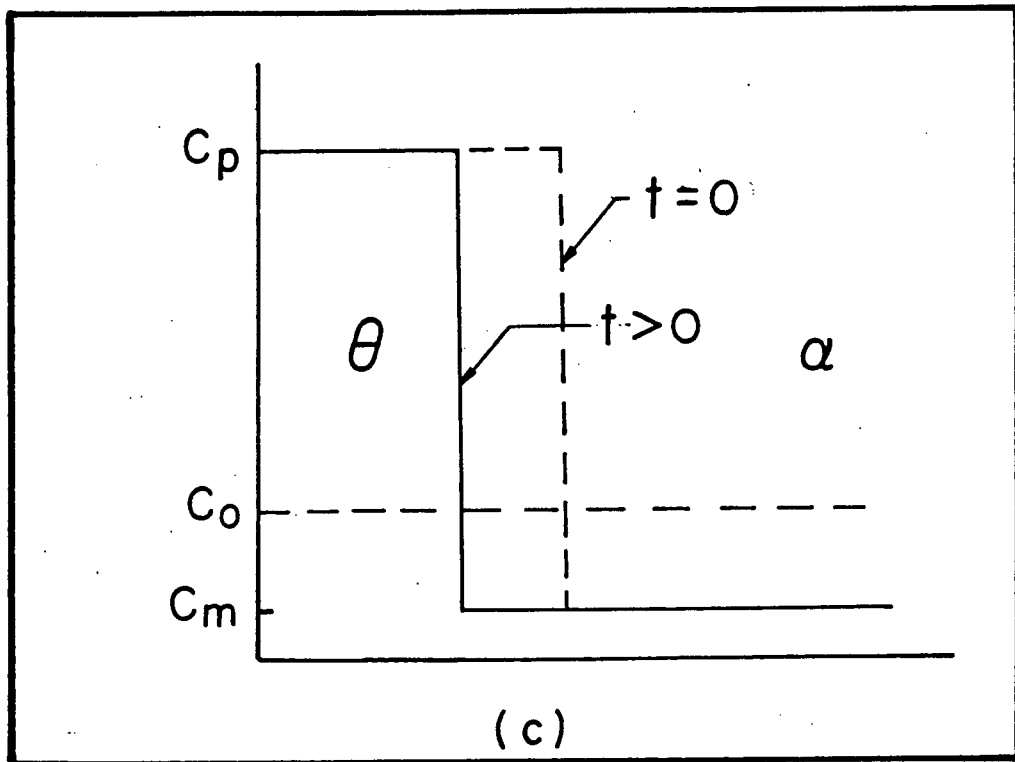


Fig. 2(c). Composition profile for an interface controlled dissolution reaction.

2(d). Profile for mixed control dissolution.

precipitate : matrix interface may then be represented by the equation:

$$J = \alpha (C_E - C_I)$$

where C_E is the equilibrium solubility at the dissolution temperature and α is the reaction rate constant. The rate of reaction will be less than that predicted by the local equilibrium model.

In any real transformation the boundary composition often lies between these extremes Fig. 2(d). In this case, part of the driving force for the reaction i.e. decrease in free energy per unit volume, is used up at the interface and the rest goes to establish a diffusion gradient in the matrix. It is however common and justifiable to approximate reactions by either of the extreme cases.

1.2 The Widmanstatten Structure

The Widmanstatten structure is most readily identified by the observation of elongated precipitates which grow independently along specific crystallographic directions within a grain. It is common for the plates to form on matrix planes of low index and they are usually associated with a large grain size of the matrix and a fair degree of supersaturation.

Much of the interest in Widmanstatten precipitation and

kinetics is due to the effects of the structure on mechanical properties. It may enhance the strength as in Al-Cu alloys or it may reduce the ductility as in Widmanstätten ferrite in steels. There are three basic morphologies, plates, needles and laths, the origins of which are still a matter of controversy. There is however a general acceptance as to the existence of a growth barrier of some kind accompanying the partitioning of elements from solid solution. Earlier theories to explain the growth barrier like the Point Effect of Diffusion and Anisotropy of Interfacial Energy have been extended by more current ones. The two principal models are the Shear Mechanism^{3,4} and the Ledge Theory.^{5,6}

The shear mechanism connotes a non-diffusional, deformation-like process, wherein each solvent atom in the matrix has a predestined site in the precipitate. Displacement of an atom occurs in cooperation with its neighbours. The theory is defended on the basis of successful application of the Phenomenological Martensitic theory⁷ which predicts the observed crystallography and surface relief effects in several systems. For example, plate formation in α - γ Al-Ag,^{8,9} disordered \rightarrow ordered AuCu 11^{10,11} and $\beta^1 \rightarrow \alpha_1$ Cu-Zn.^{12,13} The fact that the theory cannot account for needle shaped precipitates and its other inherent shortcomings have been thoroughly discussed by Aaronson et al.¹⁴

The ledge mechanism has received much wider attention.

Details of the theory are deferred to a later section, but essentially it considers growth or dissolution to occur by the lateral motion of steps with coherent terraces and incoherent ledges. The barrier to migration is then the result of a deficiency in the supply of these ledges. Weatherly¹⁵ has obtained convincing evidence of such ledges in both the Al-Mg₂Si system and the Al-Cu system. Several others¹⁶⁻¹⁸ have since observed these ledges. However their precise role during interface migration is not yet very clear.

1.3 Experimental Studies on the Dissolution of Widmanstätten Precipitates.

1.3.1 Electron Probe Studies.

Very limited work has been done in this area. Eifert et al.¹⁹ obtained the interface composition change for $\beta \rightarrow \alpha$ in Cu-12.5 wt.% Al. They found the transformation to be neither diffusion nor interface reaction controlled, but rather to be a diffusion driven lattice transformation limited reaction. In a rather definitive experiment, Hall and Haworth²⁰ observed the dissolution of the θ phase in Al-5% Cu to be controlled by diffusion in the α -Al matrix. Results of similar studies carried out on γ plates in Al-Ag²¹ and Si plates in Al-0.57%Si²² gave interface composition values less than the equilibrium solubility values. The results in both cases were

interpreted to indicate interface reaction controlled dissolution.

1.3.2 Kinetic Studies

Dissolution kinetic studies carried out so far have been on angular-shaped precipitates following the pioneering work of Thomas and Whelan.²³ There have been no corresponding measurements on plate-shaped precipitates. The case of precipitate growth must therefore be considered here.

Extensive data on the lengthening kinetics of plates are now available in a wide range of alloy systems.^{24,25} From the results available, it appears that the lengthening kinetics can be satisfactorily understood in terms of the volume diffusion control, local-equilibrium model.

Thickening kinetics have been measured using a variety of experimental techniques, for example thermionic emission microscopy (α Fe-C),²⁶ hot-stage polarised light microscopy (κ Cu-Si),²⁶ hot stage transmission electron microscopy (γ Al-Ag)¹⁷ and room temperature transmission electron microscopy (θ' Al-Cu).²⁷ In all these cases as well as several others,^{28,29} thickening kinetics were found to be slower than volume-diffusion controlled rates.

The results have been explained on the basis of shortage of ledges giving rise to the apparent inhibition. Recent studies on γ plates in the Al-Ag system by Doherty and co-workers³⁰⁻³² indicate inhibition to occur only

during the initial stages of precipitation and growth thereafter proceeds by volume diffusion.

1.4 Aim of Present Investigation

The present investigation has been undertaken to elucidate the roles of volume diffusion and interfacial structure in the dissolution of Widmanstätten plates.

The thinning and shortening kinetics of several individual bulk precipitates have been measured by scanning electron microscopy with composition profiles being measured on an electron probe microanalyzer. The experimental approach is basically non-statistical unlike conventional population methods. The resulting data are analyzed on the basis of current analytical models.

An analysis which accounts for the combined effects of precipitate thinning, shortening and interfacial structure is presented. This unified approach will hopefully bring into better perspective the overall mechanism pertaining to the dissolution of $\gamma(\text{Ag}_2\text{Al})$ plates.

2. EXPERIMENTAL PROCEDURE

2.1 Choice of System

Fig. 3 shows the phase diagram for the Ag-Al binary system. Precipitation of the close-packed hexagonal (Ag_2Al) γ -phase takes place on slow cooling the supersaturated Al-rich α -solid solution. The conjugate habit planes $\{0001\}_{\gamma} // \{110\}_{\alpha}$ which form the broadfaces of the Widmanstätten plates have identical atom patterns. However the corresponding atom spacing at the edges, $\langle 1120 \rangle_{\gamma} // \langle 110 \rangle_{\alpha}$ differ slightly.¹⁷

The growth kinetics of both the transition γ' and equilibrium phases have been extensively documented, providing a backlog of ancillary data pertinent to this work.

The system was also considered very suitable because of the following reasons:

(i) the low vapour pressure of the alloy which ensures constant surface composition at the experimental temperatures.

(ii) significant variation in concentration around a dissolving precipitate, due to a rapid solvus composition change with temperature.

(iii) The high degree of accuracy that can be achieved in quantitative analysis of the system using the electron probe microanalyzer. (This accuracy is due to the small correction required to convert the measured Ag X-ray intensity to weight percent Ag present.)

2.2 Preparation of the Master Alloy

A master alloy of nominal composition 15.50 wt.% Ag

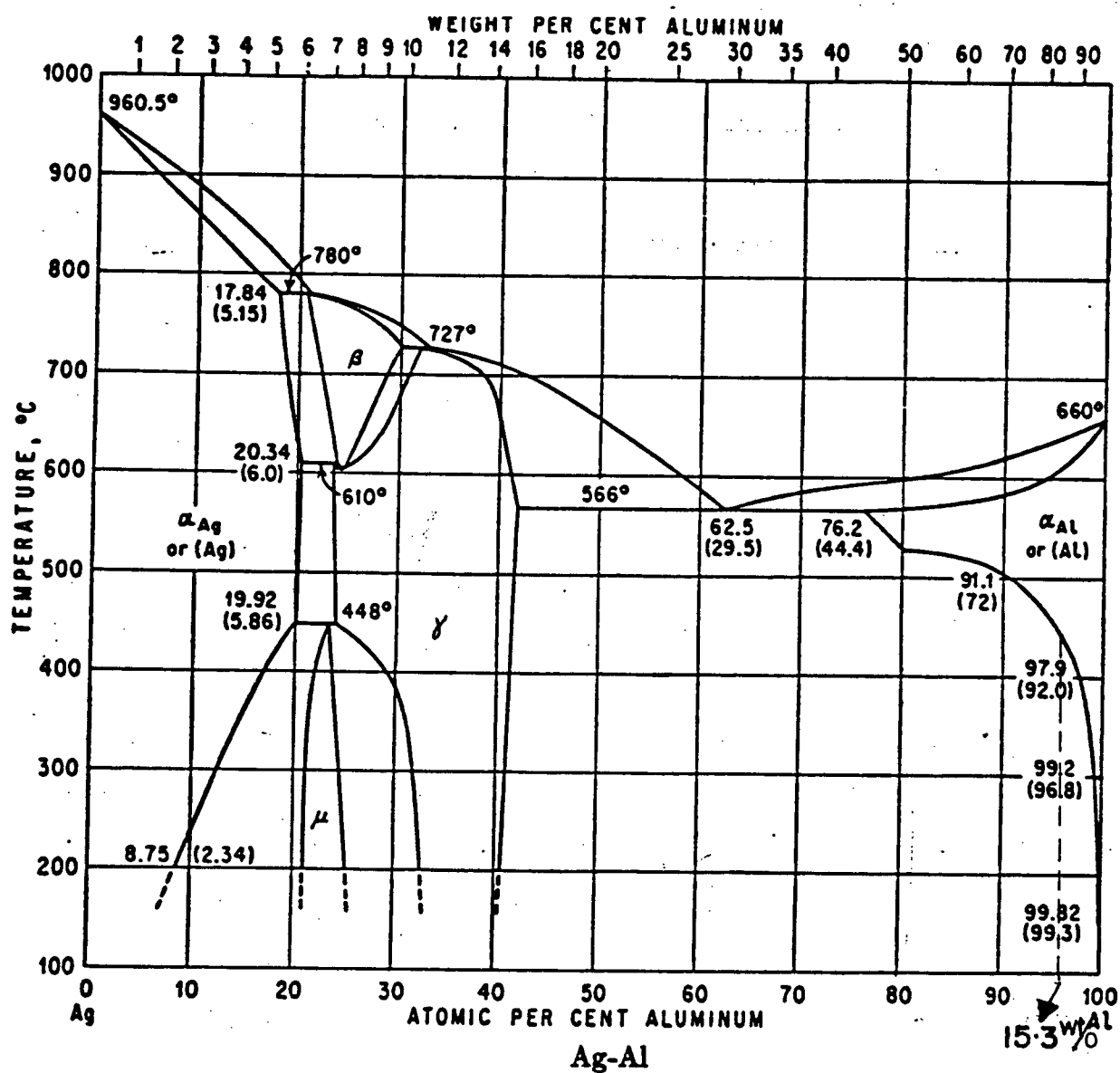


Fig. 3. Ag-Al binary diagram (Hansen⁴⁸).

was prepared by melting fine silver of 99.95% purity and 99.99% pure aluminum in a graphite crucible. A split graphite mould casting produced a slab of dimensions 68 mm x 44 mm x 99 mm. This was then homogenized for one week at 520°C.

The silver content of the alloy was determined on representative samples drilled from different parts of the slab. Analysis performed by Cantest Ltd. using atomic absorption, gave an alloy composition of 15.34wt.% Ag. This value was independently checked by obtaining the exact solvus temperature. The corresponding composition from the equilibrium phase diagram deviated by no more than 1% from the Cantest value. Later scanning of microscopic sections of the alloy in the electron probe microanalyzer showed no significant microsegregation.

Sections of the slab one centimetre wide were cold rolled to a 50% reduction. These were then annealed for 2 hours at 500°C and given a further reduction to 0.1 cm thickness. Pieces cut from this sheet were annealed at 520°C for 3 days and water quenched to room temperature to give a homogeneous α solid solution.

2.3 Specimen Preparation

In order to be able to study dissolution of individual precipitates, a heat treatment procedure had to be developed which would produce large precipitates well separated from each other in order to eliminate diffusion

field overlap. It became evident after several initial trial runs that the desired microstructure could not be produced either by quenching and isothermal ageing or by slow cooling. The isothermal treatment technique of Aaronson et al.³³ proved more suitable. This involved an initial 3 day ageing treatment at 445°C to give complete precipitation of the γ phase. The specimen was then transferred to a furnace at 466°C for 12 minutes to give dissolution of the smaller precipitates and to leave only a few precipitates remaining. Final ageing at 445°C for 5 days caused these remaining precipitates to grow giving large precipitates with a large separation.

Fig. 4 shows a typical microstructure of the equilibrated alloy, whilst Fig. 5 shows the population distribution curve. The mean aspect ratio (length/thickness) is shown to be 96. Precipitates were generally about 50 μm minimum separation.

Specimens were then polished to a 0.5 μm diamond finish and mildly etched in a 5% NaOH solution for 20 seconds. About 2-3 μm of the matrix dissolved leaving the precipitate untouched. A dark amorphous residue left on the specimen surface as a result of the etching was removed by ultrasonic cleaning.

Individual precipitates to be studied were subsequently selected optically using the following criteria, in order of priority;

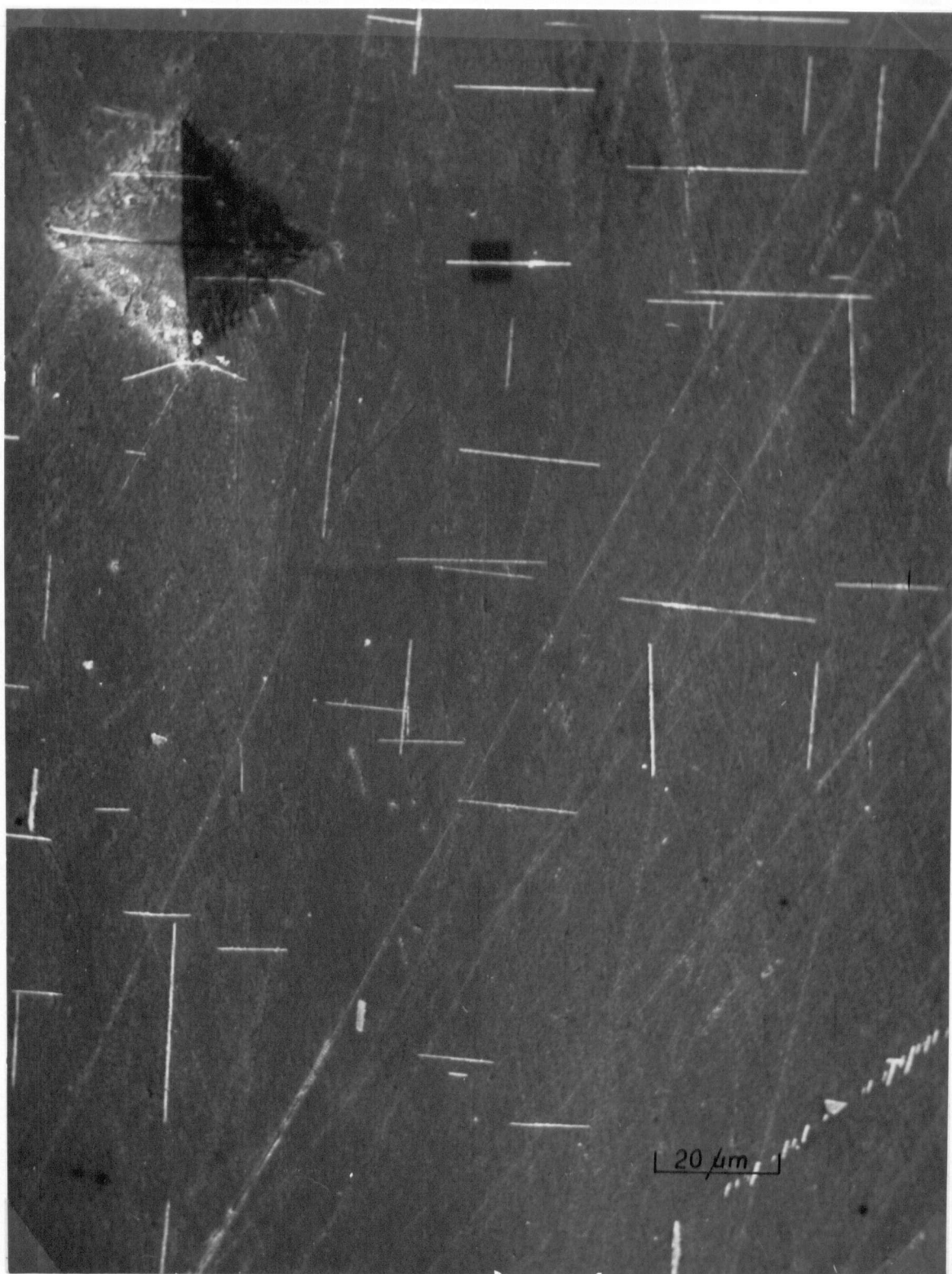


Fig. 4. Microstructure of an equilibrated alloy.

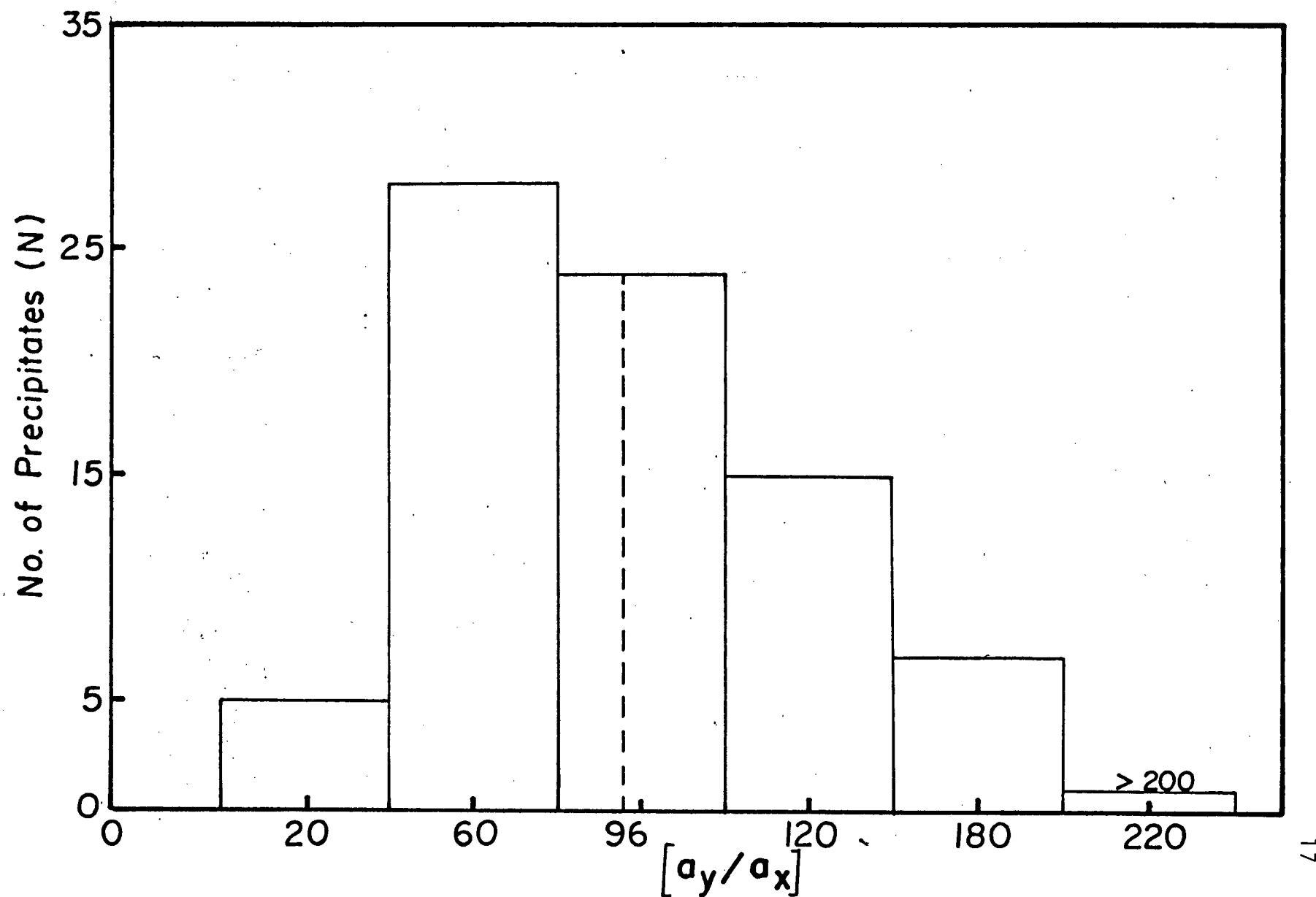


Fig. 5. Population distribution curve for Widmanstatten plates of varying Aspect Ratio.

(i) large separation from neighbouring precipitates and grain boundaries to avoid impingement of diffusion fields. A 60 μm minimum precipitate free zone was easily attainable.

(ii) large sized precipitates (for which sectioning was considered to be close to the center).

(iii) perpendicularity to specimen surface.

This procedure was necessary to facilitate later interpretation of the results although it was not possible to satisfy all three requirements in every single case.

Selected precipitates were identified with micro-hardness indentation marks (see Fig. 4) after which the etching was carefully removed on a 0.5 μm diamond wheel. Polishing scratches introduced in the process proved an indispensable complement to grain boundaries and indentation marks in locating precipitates during the later stages of dissolution.

Before proceeding to the study of dissolution kinetics it was important to first ascertain the effect of surface diffusion on the bulk precipitates observed on the specimen surface. Samples were solution treated at 474°C for 20 minutes to give partially dissolved precipitates. Two experiments were then conducted

(a) Using the SEM, widths of several individual precipitates were measured. Repeated measurements were made following successive removal of a 2-3 μm surface layer

on a 0.5 μm diamond wheel. Thickness values remained constant for more than half a dozen runs indicating identical internal and surface dissolution behaviour.

(b) The second experiment was carried out on the electron probe microanalyzer. This involved measurement of diffusion profiles surrounding partially dissolved precipitates using the same polishing technique described above. There was once again no difference in the diffusion fields at the surface and in the interior of the specimen.

Subsequent profiles obtained on nearly completely dissolved precipitates indicated a diffusion distance of about 30 μm less than the 60 μm precipitate free zone criterion. Thus the absence of both surface diffusion and diffusion field overlap were confirmed.

The entire heat treatment schedules involved in this work were carried out in air using horizontal tube furnaces. The length of the hot zone for these furnaces was about 4 cm. Temperature control was within $\pm 1^\circ\text{C}$ for prolonged periods, checked periodically using a potentiometer. The transfer time from the furnace to the quenching bath was less than 1.5 seconds. The specimens were solution heat treated at temperatures: 458°C, 466°C, 474°C, 485°C and 494°C.

2.4 SEM : Single Precipitate Measurements

In order to study the progressive dissolution of one precipitate it was necessary to examine it at the specimen

surface. Optical microscopy would have required etching and so might have caused a change in surface conditions. Electron microscopy gives images from a flat surface and was therefore more useful.

The secondary electron mode of an ETEC Autoscan scanning electron microscope operated at 20KV excitation was used. The precipitate thickness (a_x) and edge to edge length (a_y) were measured for corresponding time increments until total dissolution.

2.4.1 Shortening Kinetics

Measurements of precipitate length were made directly on the monitor of the SEM at a fixed magnification of 1000X using vernier calipers. A ruled grating standard was employed to calibrate the microscope. It was often found necessary for the sake of precision, to obtain lengths from both secondary and backscattered electron images. The appropriate compensation in magnification was made whenever it became necessary to tilt the specimen for measurements although this was seldom done.

2.4.2 Thinning Kinetics

Precipitates were photographed on a Polaroid camera attached to the SEM console. Thickness measurements were obtained directly from the photograph using vernier calipers. Measurements were made to within 0.01 cm on the photograph corresponding to 0.01 μm on the specimen. At

longer dissolution times, precipitate resolution was greatly impaired through surface degradation from repeated heat treatment cycles.

2.5 SEM : Population Study

Six aged specimens were solution treated at 466°C for various lengths of time (0, 8, 20, 32, 48 and 60 minutes). Specimens were placed in a 5% NaOH solution to partially dissolve the matrix following the technique of Doherty et al.³² The soft reacted matrix was ultrasonically flushed in alcohol and the residue, composed of fully extracted precipitates, was dried for metallographic observation. The etchant did not appear to attack the precipitates at all; their edges appearing straight and the faces very flat. The lengths of over 250 extracted plates per specimen were measured directly on the SEM.

Measurements were made only of precipitate length. No observations were made of thickness. These measurements could not be made using the present technique since the precipitates obtained lay flat on the SEM specimen holder. However they could have been made by deep etching of the matrix causing the precipitates to stick out. Since this statistical study was just to confirm the direct kinetic results, such time consuming measurements seemed unnecessary.

The technique used is a variation to the usual method

of measuring lengths of the largest precipitates present on the plane of polish. The statistical sampling is thereby improved in that true precipitate lengths are always measured.

2.6 Electron Probe Microanalysis Profiles

Matrix concentration profiles around partially dissolved precipitates were mapped using a JEOLCO JXA-3A electron probe microanalyzer. Dissolution profiles at 485°C and 474°C were generated. In order to obtain a minimum spot size an accelerating potential of 15KV was selected to satisfy the criterion for optimum accuracy in quantitative analysis:

$$\frac{V}{V_K} = 3$$

where: V = the accelerating potential

V_K = excitation potential for $\text{AgL}\alpha$ radiation
(4.0KV).

A step-scan device attached to the microprobe micro-meter moved the specimen in 1.25 μm steps after 20 seconds counting on a spot.

Measured x-ray intensities were corrected for dead time, background, absorption, characteristic fluorescence, back-scattering losses and ionization/penetration losses using Colby's Magic Computer Program³⁴ to determine Ag percentages. The precision of the analysis was within 0.12 wt.% Ag for the

range of composition measured.

The largest precipitates were normally selected for study and rotated into position depending on the direction of scan. Dark contamination streaks marked scan traces as shown in Fig. 6.

2.6.1 Tip Profile

The electron beam had to be focussed exactly on the tip of the precipitate (dimension $< 1\mu\text{m}$), then traversed parallel to the precipitate into the matrix beyond the limits of any composition gradients. Bringing the precipitate and beam into coincidence involved three separate steps and proved quite difficult due to the small width of the precipitates:

(i) the beam spot was located on the crosswires of the eyepiece using a fluorescent sample.

(ii) the precipitate was aligned for parallel motion relative to the spot by observing the absorbed electron image.

(iii) accurate spot-specimen coincidence was obtained by monitoring changes in the specimen beam current as the beam crossed the precipitate-matrix boundary. This required suppressing the main specimen current and using a very sensitive scale reading on the beam current meter in order to pick up the small changes in current.

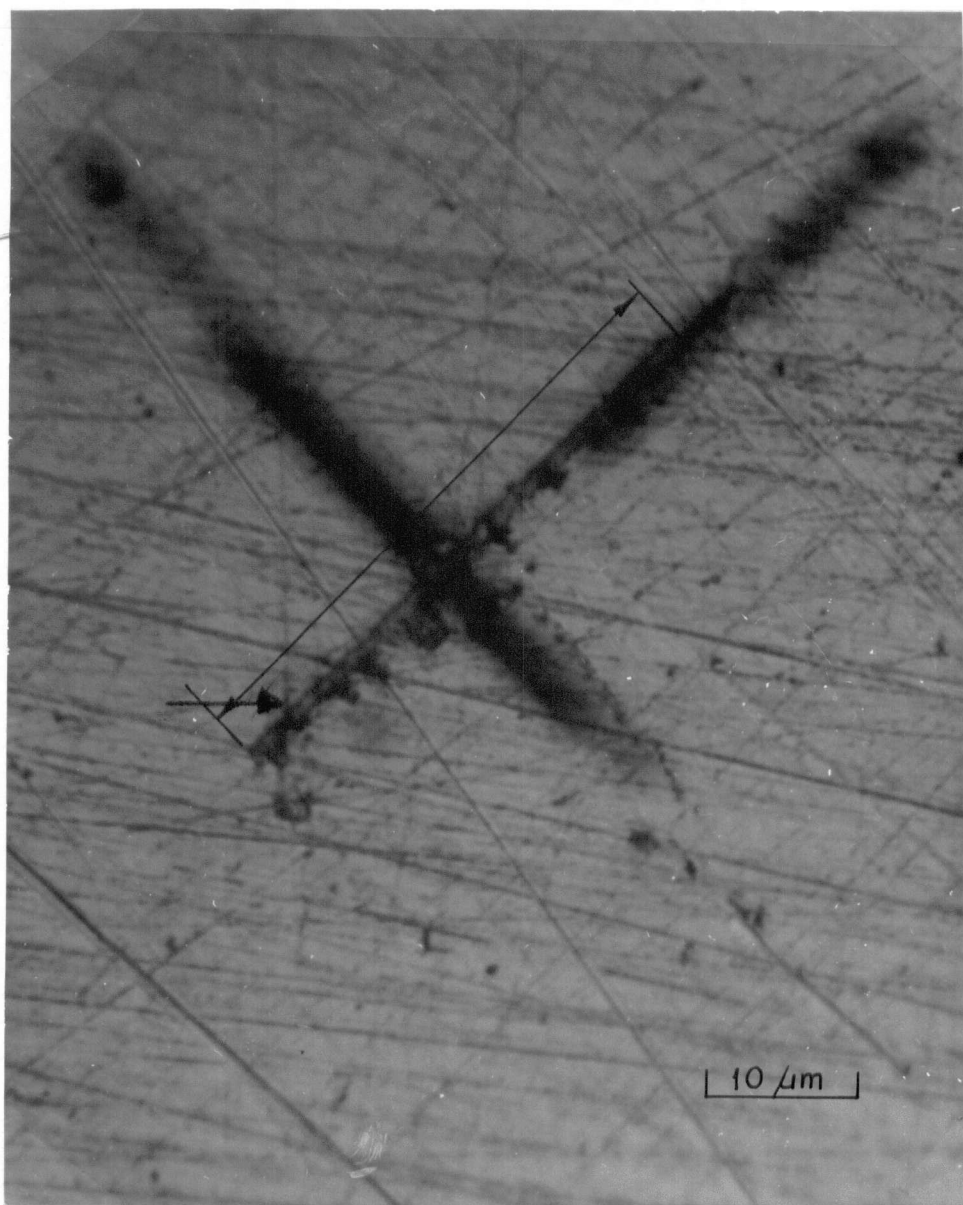


Fig. 6 Optical micrograph of a typical Widmanstätten plate (arrowed) with contamination marks showing a broadface and tip scan.

2.6.2 Broadface and Isoconcentrate Profiles

Profiles perpendicular to the broadface were generated much more readily. The precipitates had to be rotated into position, following steps (i) and (ii) above, then scanned perpendicular to the broadfaces of the precipitates.

By combining tip profiles with multiple transverse traces, contours of isoconcentrates around dissolving precipitates were mapped.

3.

RESULTS

3.1 Kinetics of Shortening3.1.1 Results

Fig. 7 shows the results of a typical dissolution experiment plotted as half-length vs time. A linear relation indicating steady state dissolution was obtained corresponding to a dissolution rate of $9.33 \times 10^{-7} \text{ cm sec}^{-1}$ at 485°C . Table II summarizes the other experiments carried out and the actual plots are given in Appendix I.

As seen from Fig. 7 and the rest of the compiled results, precipitates shorten according to a linear law until essentially complete dissolution has taken place. This implies there is no change in mechanism during dissolution. In particular it indicates an absence of diffusion field impingement from adjacent precipitates at the latter stages of diffusion. This simplifies the analysis markedly and all the theoretical models to be discussed will cover precipitate dissolution under semi-infinite conditions only.

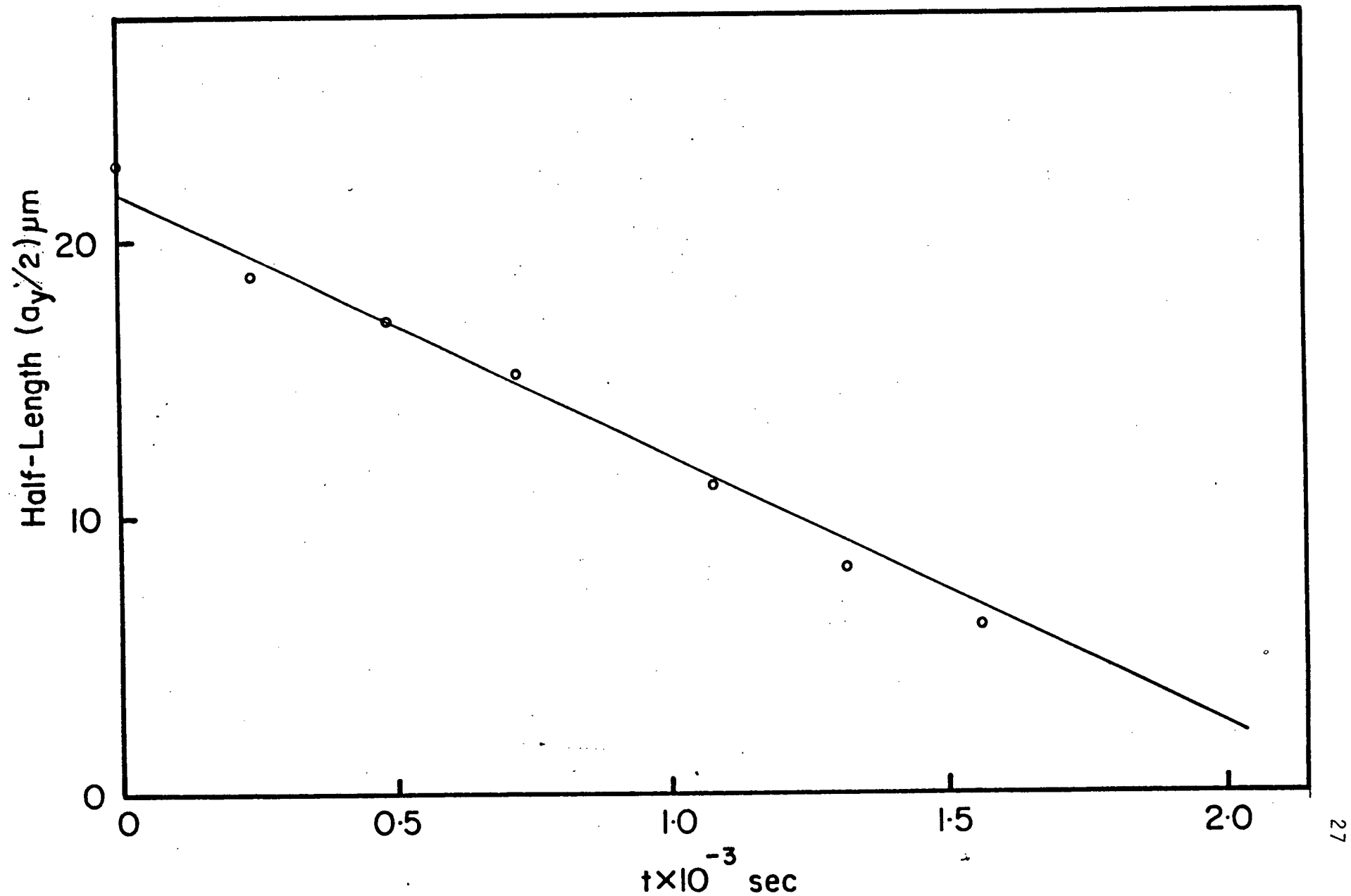


Fig. 7. Linear time plot of shortening kinetics at 485°C.

Table II. Compilation of Single Precipitate Results : Shortening

Temp. °C	Dissolution Velocity, $v \times 10^7 \text{ cm sec}^{-1}$						\bar{v} Mean Velocity $\times 10^7 \text{ cm sec}^{-1}$	Std. Dev.
	Ppt. 1	Ppt. 2	Ppt. 3	Ppt. 4	Ppt. 5	Ppt. 6		
458	0.73	1.05	0.58	0.78	0.87	0.89	0.82	0.18
466	2.05	1.61	2.41	2.11	1.83	1.88	1.98	0.27
474	4.28	5.42	4.37	4.50	4.08	4.41	4.51	0.52
485	7.8	9.17	8.33	8.17	9.00	9.20	8.62	0.58
494	13.8	18.5	14.5	17.2	15.3	15.8	15.87	1.94

3.1.2 Analysis of Results

The Ag_2Al precipitates were of large initial aspect ratio (length/thickness) averaging 96. The dissolution of the edge can therefore be considered independent of dissolution of the broadface.

There are a number of analytical models in the literature to describe growth of a tip. Most of these can be modified to account for dissolution. In this thesis, the Horvay-Cahn⁴⁹ model, the Zener-Hillert⁵⁰ model and the Jones-Trivedi⁵¹ theory will be discussed. These all involve steady state diffusion and hence it is possible to have them modified to the case of dissolution by essentially redefining the supersaturation parameter.

The Horvay-Cahn model considers the migrating tip to be a parabolic cylinder of constant size moving with constant velocity. The solution to the diffusion equation for a tip dissolving at a diffusion controlled rate yields isoconcentrate lines as shown in Fig. 8(a). The dissolution rate is related to the supersaturation parameter (f) by the equation:

$$f = \frac{\sqrt{\pi}}{2} \sqrt{p} e^p \operatorname{erfc} \sqrt{p} \quad \dots 1$$

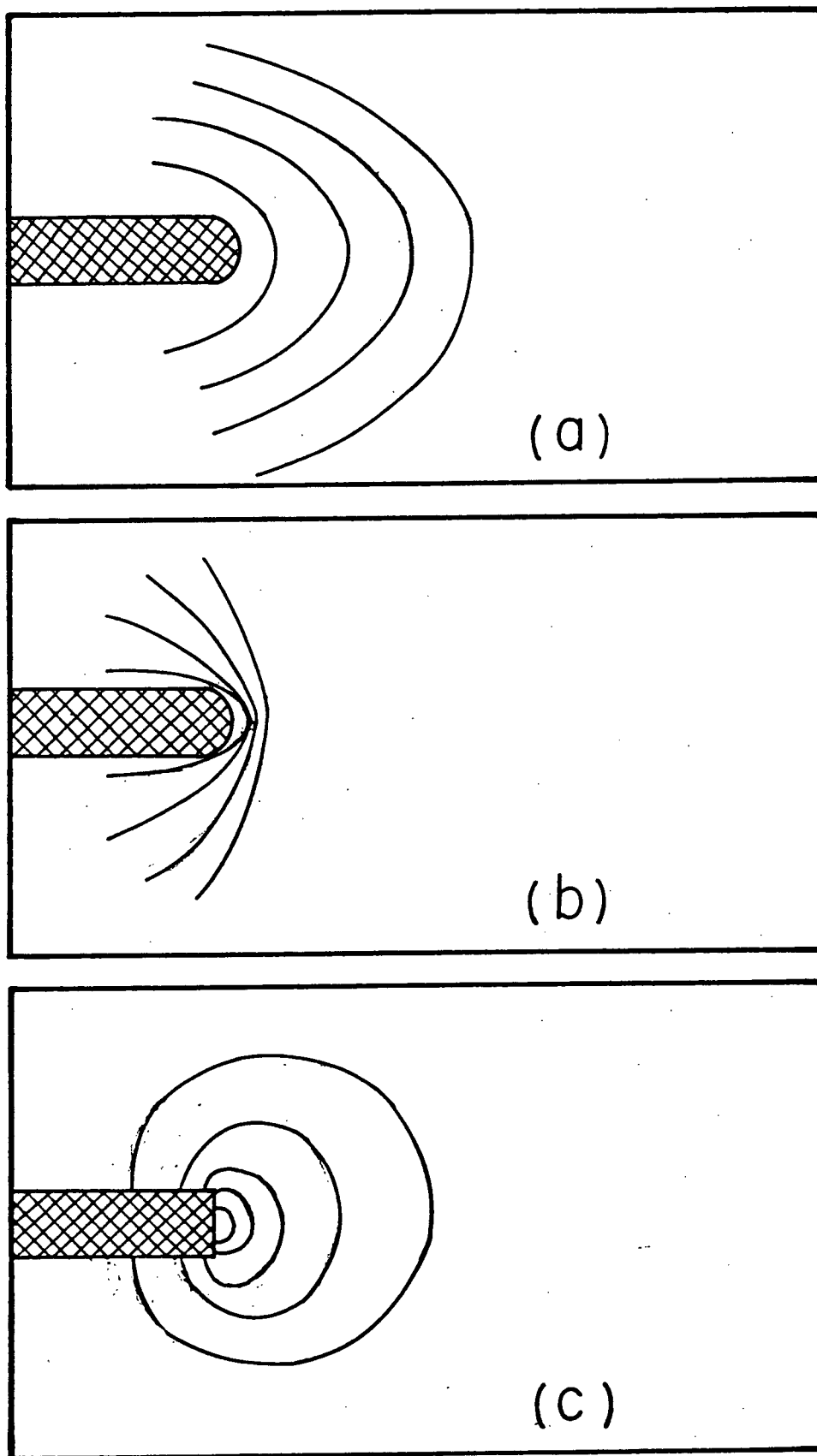


Fig.8. Schematic drawing of the steady-state diffusion field near a Widmanstatten precipitate tip according to
 (a) the Horvay-Cahn model
 (b) the Zener-Hillert model
 (c) the Jones-Trivedi model.

where the Peclet number $p = \frac{v\rho}{2D}$

with v = tip velocity

ρ = radius of curvature at the tip, and

D = diffusion coefficient.

and

$$f = \frac{C_I - C_M}{C_p - C_I}$$

In applying this theory to the present experimental results, it was necessary to make a determination of the radius, ρ . Measurements were made either intermittently during the kinetic study directly off the SEM screen or indirectly from photographic enlargements. The values of ρ determined on the screen were accurate to better than 3%. The value of ρ generally appeared to decrease during a dissolution run and indeed seemed to have a value close to the half thickness of the precipitate. The constancy of the dissolution rate measured implies that if the Horvay-Cahn theory is to be applied, a constant radius of curvature is required. Accordingly an average of the measured values was used and this would always be within a factor of 2 of the actual radius at any time. This would thus lead to a maximum error in the diffusion coefficient of 2 times. For most experiments a mean radius of 0.20 μm was used. It is realized that this procedure is not wholly satisfactory but is essential if the Horvay-Cahn model is to be used.

The results of diffusivity values thus obtained are summarized in Table III.

The Zener-Hillert model is similar to the Horvay-Cahn model except that account is taken of the capillarity effect at the tip. This has the effect of increasing the dissolution velocity at small radii of curvature. Profiles generated by their solution are shown in Fig. 8(b).

The significance of capillarity effects can be readily determined from the Gibbs-Thompson equation:

$$C_{Ir} = C_{Ip} (1 + \Gamma K) \quad \dots 2$$

where

$$\Gamma = \frac{\gamma \bar{V}}{RT}$$

with

γ = interfacial energy

\bar{V} = partial molar volume of solute atoms in precipitate

R = gas constant

T = temperature

C_{Ir} = composition in the matrix at the curved precipitate: matrix interface.

C_{Ip} = equilibrium interphase composition

In the present work the change in the interface composition is calculated to be of the order of 1% and thus the effect of capillarity is negligible. Hence the model

Table III. Comparison of Calculated Mean Diffusivities \bar{D} : Shortening

Temp. °C.	Supersaturation f	Mean Tip vel. \bar{v} $\times 10^7 \text{ cm sec}^{-1}$	\bar{D} Horvay-Cahn Model $\times 10^9 \text{ cm}^2 \text{ sec}^{-1}$	\bar{D} Zener-Hillert $\times 10^9 \text{ cm}^2 \text{ sec}^{-1}$	\bar{D} Jones-Trivedi $\times 10^9 \text{ cm}^2 \text{ sec}^{-1}$
458	0.018	0.82	0.71	0.73	0.66
466	0.034	1.98	0.76	0.91	0.54
474	0.083	4.51	0.98	0.78	0.72
485	0.132	8.62	0.88	0.96	0.23
494	0.176	15.87	0.58	1.22	0.37

should give results identical to those of the Horvay-Cahn theory.

The Zener-Hillert model is essentially valid for low supersaturation conditions i.e. $p \ll 1$, representative of the conditions of the present alloy e.g. 0.08 at 485°C. The final form of the solution based on Zener's maximum growth hypothesis is given as:

$$f = \frac{8p}{1+8p} \quad \dots 3$$

f being the supersaturation, and p the Peclet number, Equation 1. As shown in Table III, D values calculated by the Zener-Hillert model are in very good agreement with those of the Horvay-Cahn model.

The Jones-Trivedi analysis was developed for the lateral growth of a ledged boundary. It assumes the step spacing is such that each step may be considered independent and that diffusion occurs only in the parent phase. In this model, atoms leave or enter the phase only at the step face. The step has to advance and yet retain its shape. The Laplace equation is assumed and a solution to the moving boundary equation at the ledge is obtained. When diffusion is rate controlling, the final form of the equation describing the step velocity V_s is given as:

$$V_s = \frac{2Dp}{h} \quad \dots 4$$

where h is the step height and p is the Peclet number. The ledge movement analyzed by Jones and Trivedi can be applied with minor modifications to the dissolution of a tip, since the tip can be considered made up of two ledges placed side by side as shown together with resulting profiles in Fig. 8(c). The tip is therefore considered to be flat with rapid diffusion along the interface and negligible diffusion across the broadface.

Since the precipitates were in fact observed to have quite large radii at the tip, this model is a fairly good representation of the effect at the tip. The value of h used is $0.2 \mu\text{m}$ corresponding to the tip radius measurement. This obviously must be an approximation. Substituting V_s values obtained from half-length vs time plots into Equation 4 gives values of D shown in Table III.

It can be seen that the agreement with the values for the Horvay-Cahn and Zener-Hillert theories is excellent. Thus three different theories, all assuming diffusion control at the tip give similar values of D . The inherent differences in the models become noticeable at the higher dissolution temperatures. Particularly at 494°C significantly lower values are obtained for the Zener-Hillert and Jones-Trivedi models.

The experimental values of D thus determined were compared to literature values. The work of Heumann and Böhmer³⁵ was found most suitable for this purpose. They

determined the diffusivity of Ag in Al by radioactive tracer techniques and diffusion couple measurements over a wide temperature range i.e. 400°C - 650°C. Results obtained were in confirmation of those by earlier workers.^{36,37} The agreement between mean D values obtained in the present study, Table III, and literature values were always within a factor of three and in most cases better than a factor of two.

Fig. 9 shows the experimental diffusivity values obtained on the basis of the Zener-Hillert model plotted as $\log D$ vrs $\frac{1}{T}$. The values of D show some scatter but lie close to the Heumann and Bohmer line.

The present results are thus in accord with literature values. It thus appears likely that dissolution of the tip is controlled by volume diffusion of solute in the matrix.

3.2 Shape Changes and Statistical Analysis of Precipitate Shortening

An alternate method for studying precipitate shortening was by extraction of precipitates by chemical dissolution of the matrix after various ageing times.

Fig. 10 shows a representative sequence of micrographs for four solution treatment times. Perfectly hexagonal-shaped precipitates are observed at the onset of dissolution. The sharp corners become progressively rounded due to enhanced diffusion via the point effect of diffusion.

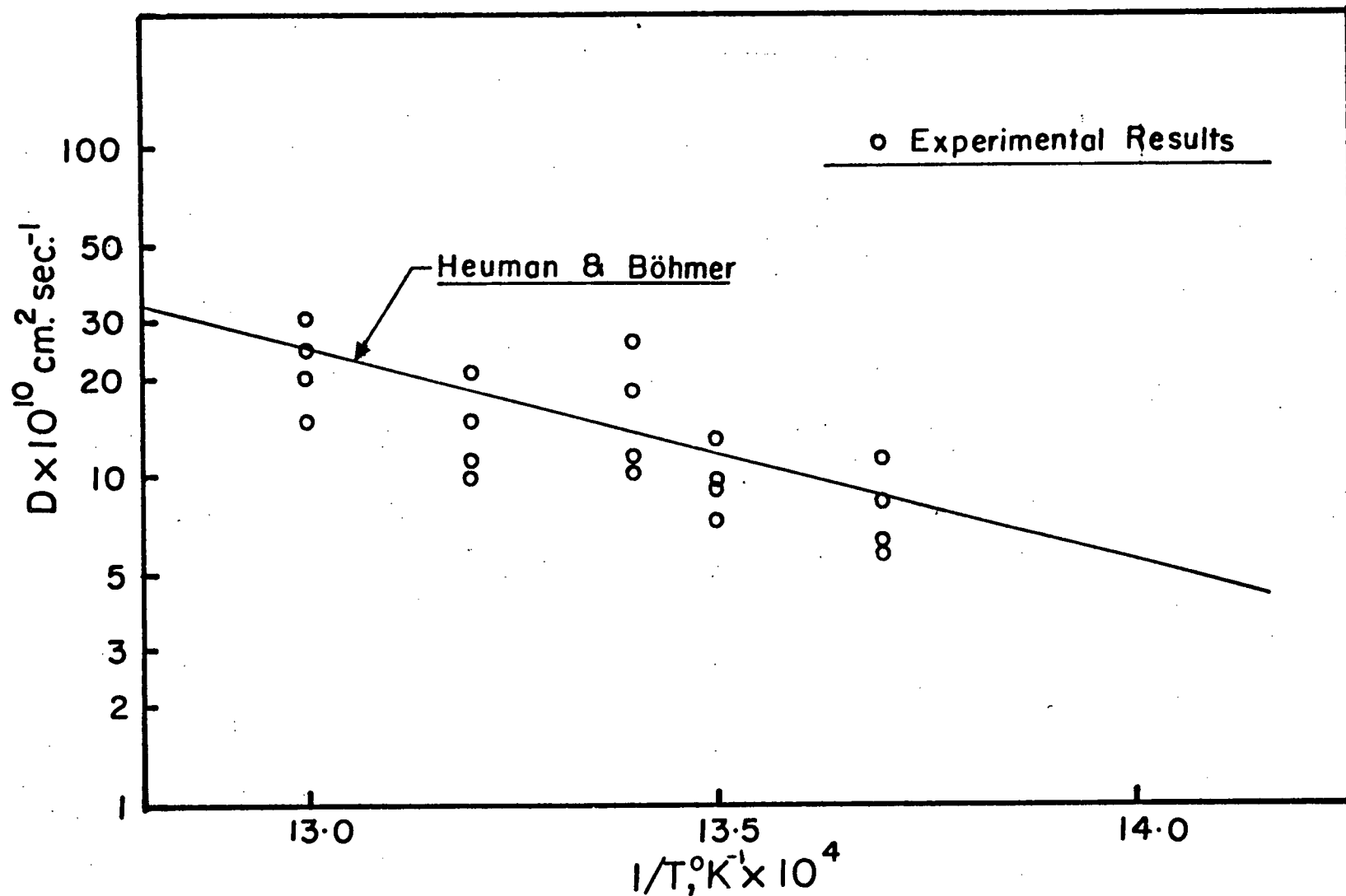
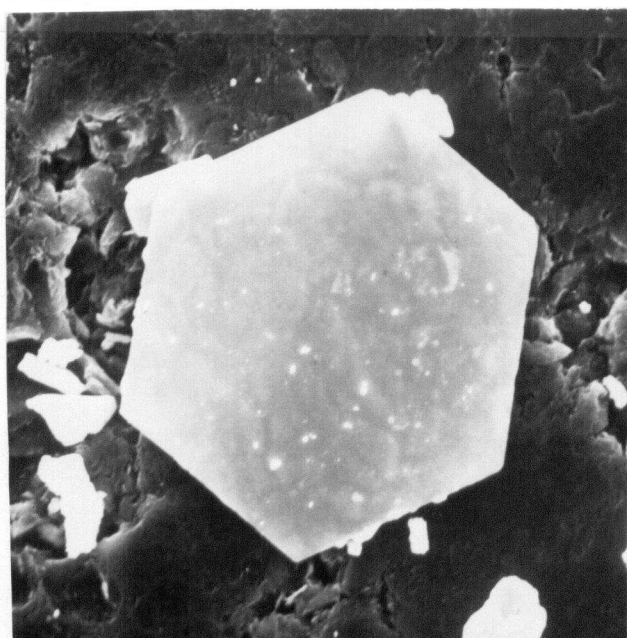
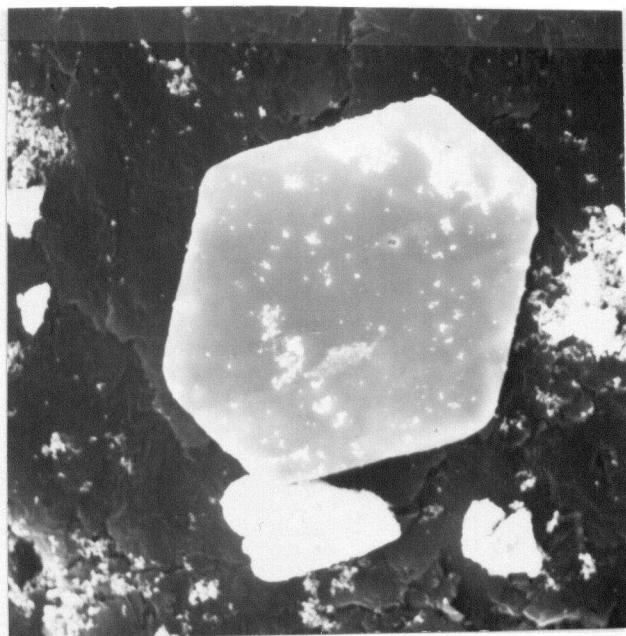


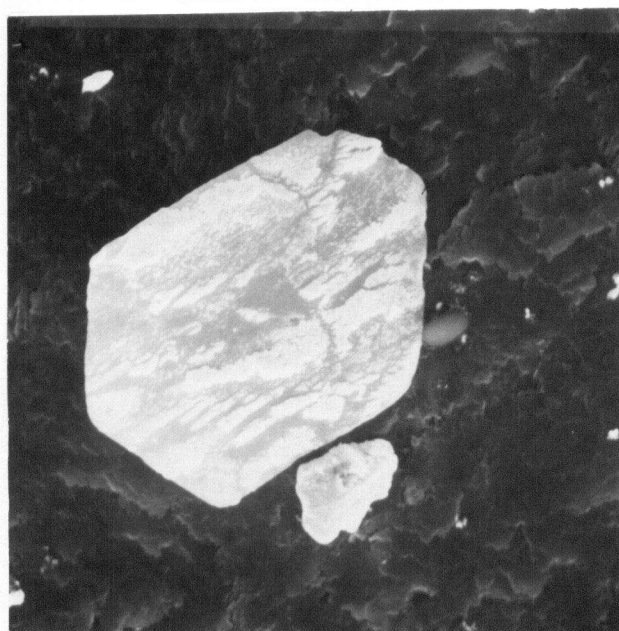
Fig.9. Arrhenius plot of D_v (Zener-Hillert) versus $\frac{1}{T}$ (K^{-1}) for dissolving Ag_2Al plates. ³⁷



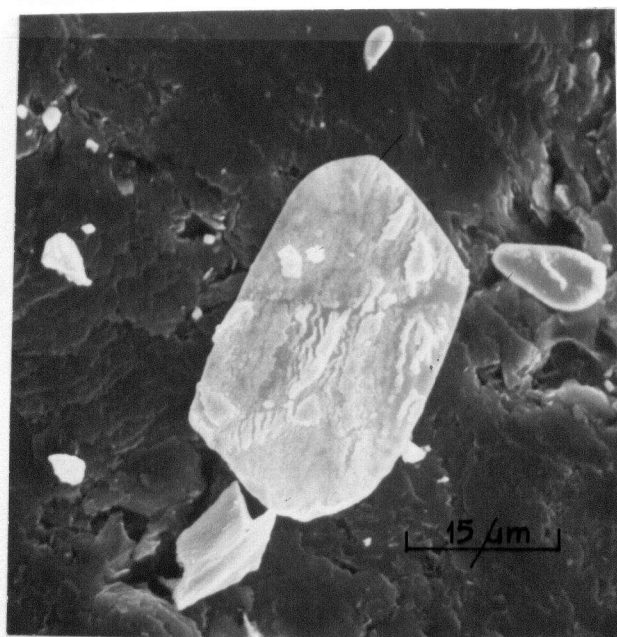
0 min



20 min



30 min



45 min

Fig. 10. Secondary electron image micrographs used to observe shape changes and population shortening kinetics of 466°C.

In the final stages of dissolution, these precipitates appear as circular discs so thin they could hardly be resolved in the microscope.

The statistical study of shortening kinetics for the Ag_2Al plates was carried out at 466°C . Fig. 11 shows the results for half-length plotted against time. Each point in Fig. 11 is the average of more than 250 measurements and the error bars correspond to the standard deviation. Mean precipitate dimensions were about 40% shorter than corresponding values for the single precipitate measurements. The difference is easily understood. Whereas the statistical measurement averages a large spectrum of lengths, precipitates selected for individual study were generally the largest sized ones.

The results followed a linear relationship as found from studies of individual precipitates. The dissolution velocity was $1.90 \times 10^{-7} \text{ cm sec}^{-1}$ in very good agreement with the mean value of $1.98 \times 10^{-7} \text{ cm sec}^{-1}$ obtained from the single precipitate plots.

The results are analyzed in a similar way to the single precipitate kinetics. Thus, diffusion coefficient values were calculated on the basis of all three theories i.e. the Horvay-Cahn, Zener-Hillert and Jones-Trivedi models. Table IV compares the present results to the equivalent mean single precipitate kinetic results and the literature value.

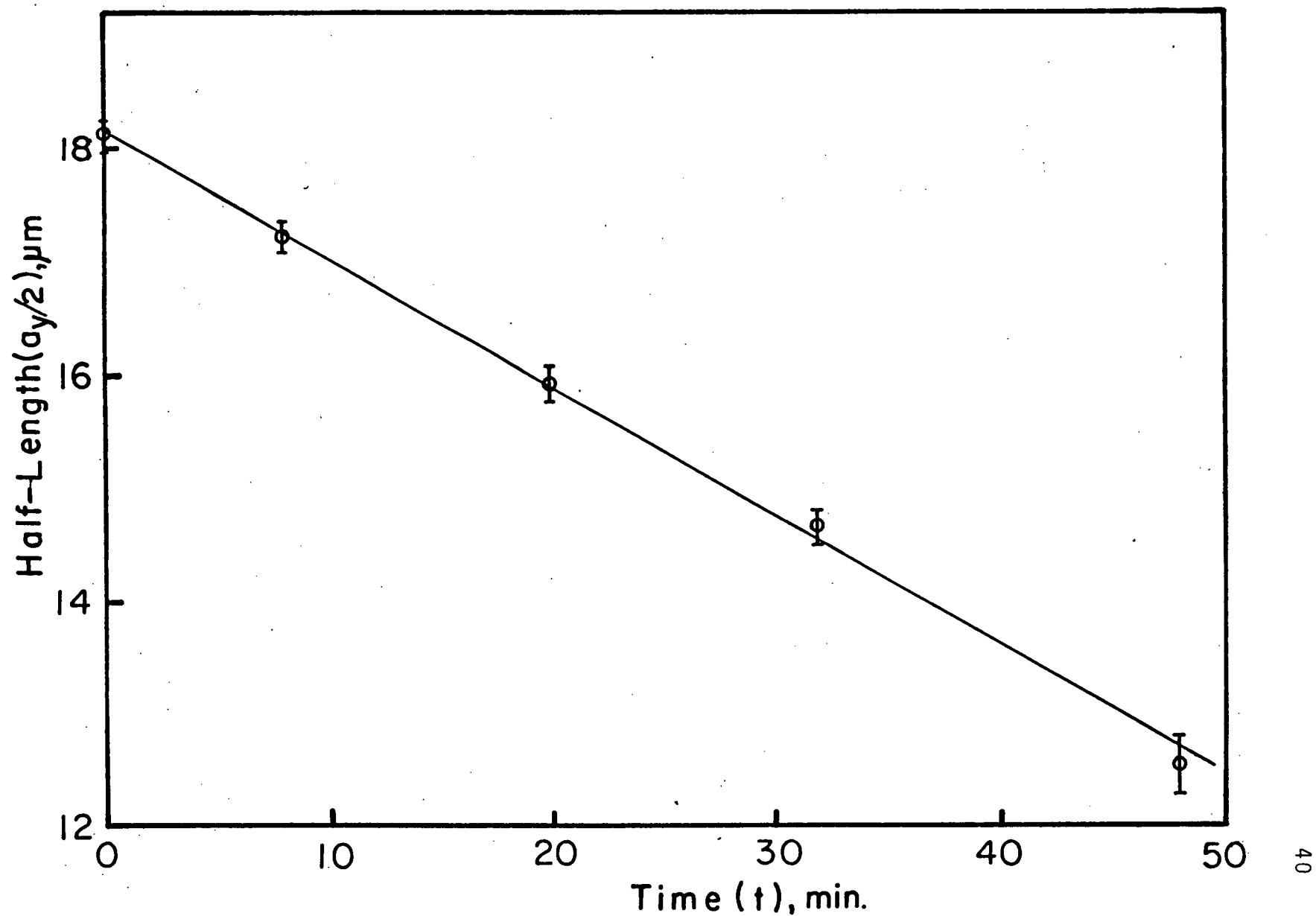


Fig.11. Shortening kinetics ($a_y/2$ -vs- t) for SEM population study.

Table IV. Population Kinetics Results

Temp: 466°C					
$D_{(lit.)}: 1.10 \times 10^{-9} \text{ cm}^2 \text{ sec}^{-1}$					
	f	tip vel. $V \times 10^7$ $\text{cm}^2 \text{ sec}^{-1}$	$(\times 10^9 \text{ cm}^2 \text{ sec}^{-1})$		
			D_{H-C}	D_{Z-H}	D_{J-T}
Population Kinetics	0.034	1.90	0.73	0.87	0.51
Mean Single Kinetics	0.034	1.98	0.76	0.91	0.54

Again very good agreement between the diffusivity values are observed, in confirmation of volume diffusion controlled dissolution of the tip.

3.3 Thinning Kinetics

A typical sequence of micrographs used to measure the thinning kinetics at 485°C is shown in Fig. 12. Fig. 13 shows the corresponding measurements.

It can be seen that the rate decreases with time but when the results are plotted against square root of time, a straight line results, Fig. 14. In general, all the results showed such parabolic behaviour with time (Appendix II). The method of least squares was used to obtain the rates, which are summarized in Table V.

The linear plot suggests that the precipitates dissolve according to the relation:

$$X = \alpha \sqrt{t} \quad \dots 5$$

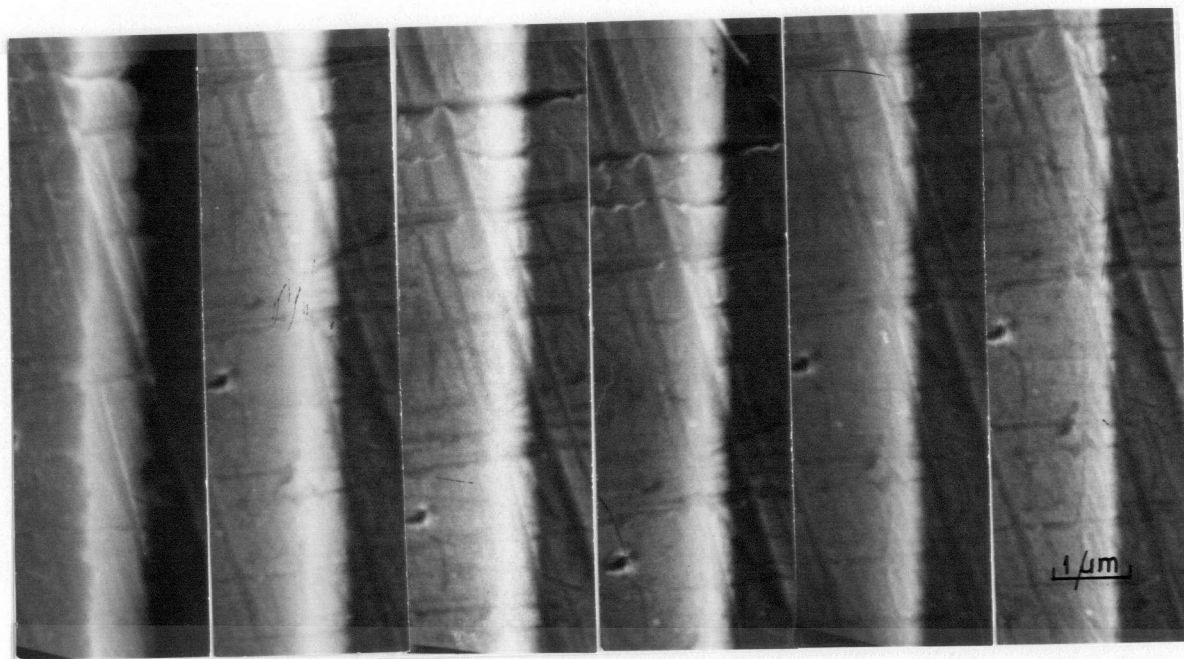


Fig. 12. Secondary electron image of thinning sequence at 485°C.

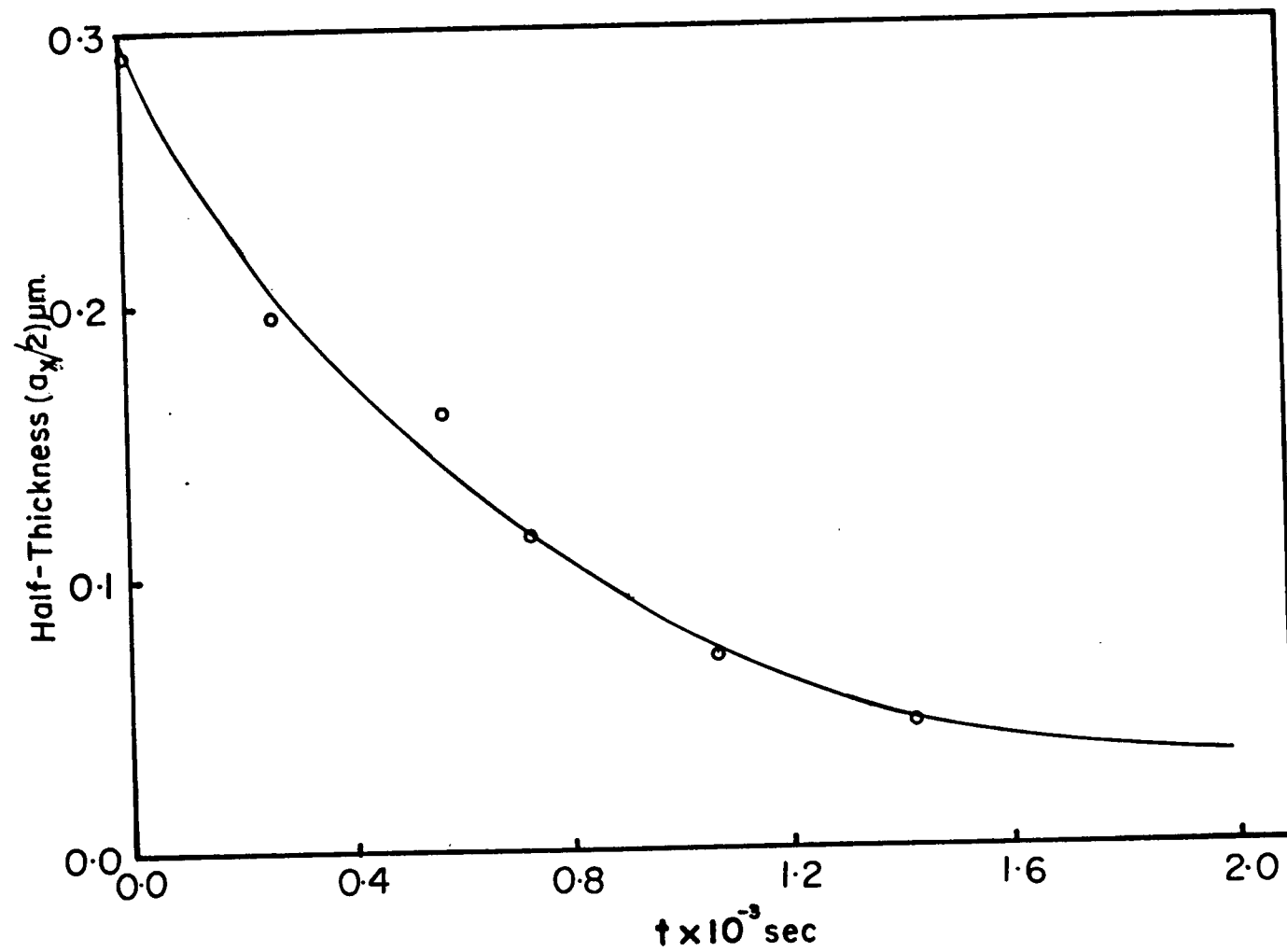


Fig. 13. Linear time plot of thinning kinetics at 485°C.

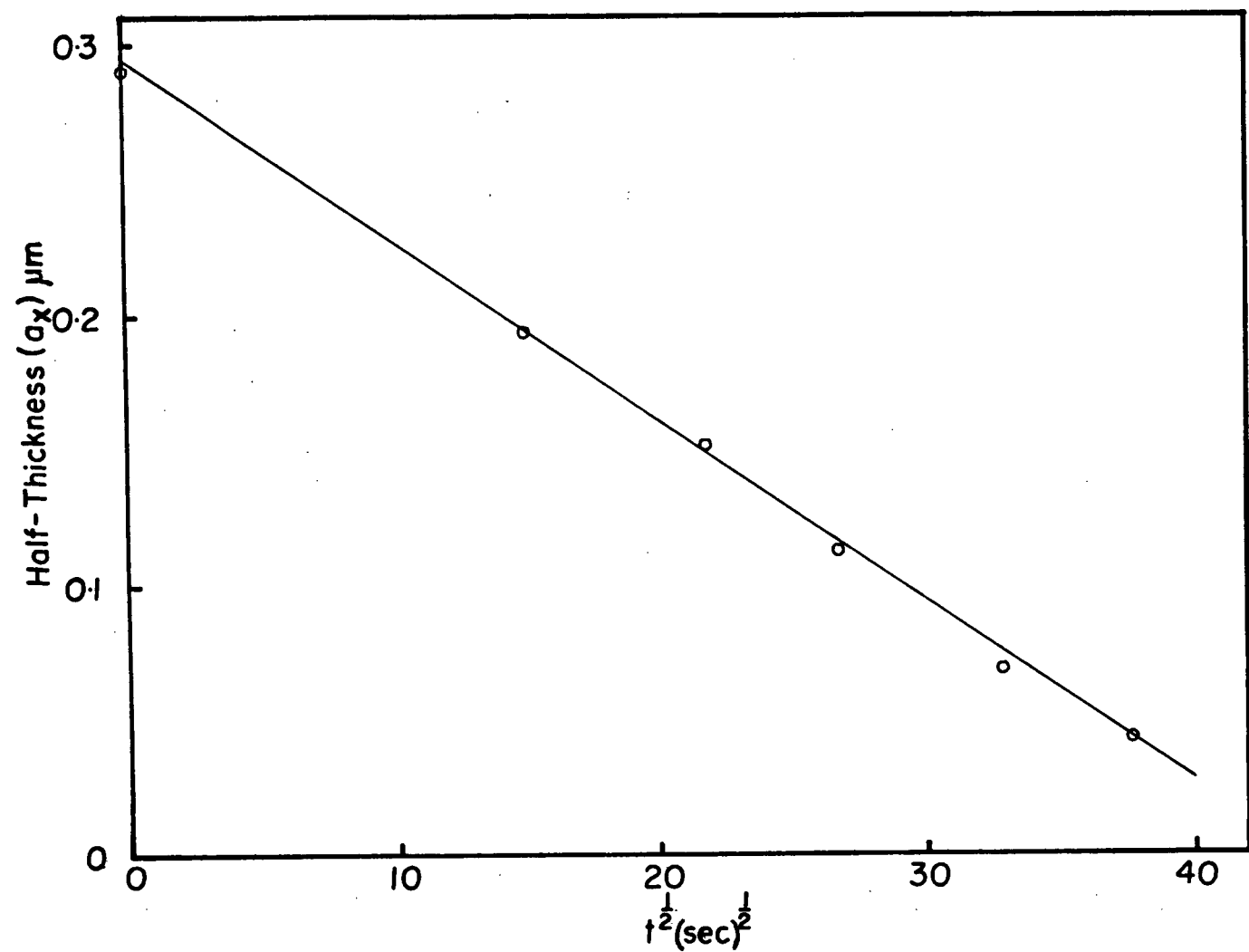


Fig. 14. Parabolic time plot of thinning kinetics at 485°C.

Table V. Compilation of Single Precipitate Results : Thinning

Temp. °C	Measured slopes, $\alpha \times 10^7 \text{ cm sec}^{-0.5}$					Mean Slope $\bar{\alpha}$ $\times 10^7$ $\text{cm sec}^{-0.5}$	Std. Dev.
	Ppt. 1	Ppt. 2	Ppt. 3	Ppt. 4	Ppt. 5		
466	1.71	2.66	2.20	1.86	1.89	2.06	0.38
474	2.13	2.80	3.52	2.40	2.55	2.68	0.53
485	6.45	8.03	9.04	7.56	8.29	7.87	0.96
494	8.65	8.87	11.30	10.52	9.27	9.72	1.14

In order to obtain a value for the rate constant, α , and hence the diffusivity, D , the Dube-Zener analysis for the migration of a planar disordered boundary was employed. For dissolution under matrix diffusion controlled conditions and with D independent of concentration, α can be obtained from the equation:

$$\pi^{0.5} \lambda e^{\lambda^2} \operatorname{erfc}(-\lambda) = f/2 \quad \dots 6(a)$$

where

$$\lambda = \alpha D^{0.5} \quad \dots 6(b)$$

and

$$f = \frac{C_I - C_M}{C_P - C_M}$$

The D values calculated using this analysis are summarized in Table VI. Also shown are the literature diffusivity values of Heumann and Bohmer.³⁵

Without exception, the diffusivity values at all temperatures were lower by two orders of magnitude compared to the literature volume diffusion rates. Such slow kinetics could only be caused by an interfacial barrier to atomic migration.

3.4 Electron-probe Microanalyzer

3.4.1 Introduction

This section deals with the direct measurement of concentration fields adjacent to dissolving precipitates. The results are presented in the following order:

Table VI. Comparison of Calculated Diffusivities : Thinning

Temp. °C	Saturation f	Mean Growth Rate $\bar{\alpha}$ $\times 10^7 \text{ cm} \cdot \text{sec}^{-0.5}$	Mean Diffusivity \bar{D} $\times 10^{11} \text{ cm}^2 \text{ sec}^{-1}$	$D_{\text{(lit.)}}$ $\times 10^9 \text{ cm}^2 \text{ sec}^{-1}$
466	0.034	2.06	2.93	0.87
474	0.083	2.68	0.81	1.37
485	0.132	7.87	2.78	1.81
494	0.176	9.72	2.38	2.27

- (i) Broadface profile.
- (ii) Tip profile.
- (iii) Isoconcentrate contours.

3.4.2 Broadface Profile

Fig. 15 shows some typical concentration profiles made before and after solution heat treatment. The blank profile taken prior to any dissolution heat treatment shows an apparent increase in Ag concentration within a region extending up to 4 μm from the particle matrix interface and is due to the finite spot size of the microanalyzer. Thus in the vicinity of a second-phase particle, a small fraction of the incident electrons are scattered by the precipitate itself. All measurements within the 4 μm range were ignored in subsequent analyses.

The boundary position was graphically ascertained to be at the midpoint of the step in the plot of Ag-L α intensity against distance.

The following assumptions were made in order to simplify analysis of the profiles:

(i) The diffusion coefficient of aluminum-silver solid solutions is independent of concentration at the dissolution temperatures. This is evidenced by the work of Heumann and Bohmer.³⁵

(ii) There is very little movement of the interface relative to the diffusion distance. (Kinetic measurements give 0.5 μm displacement.)

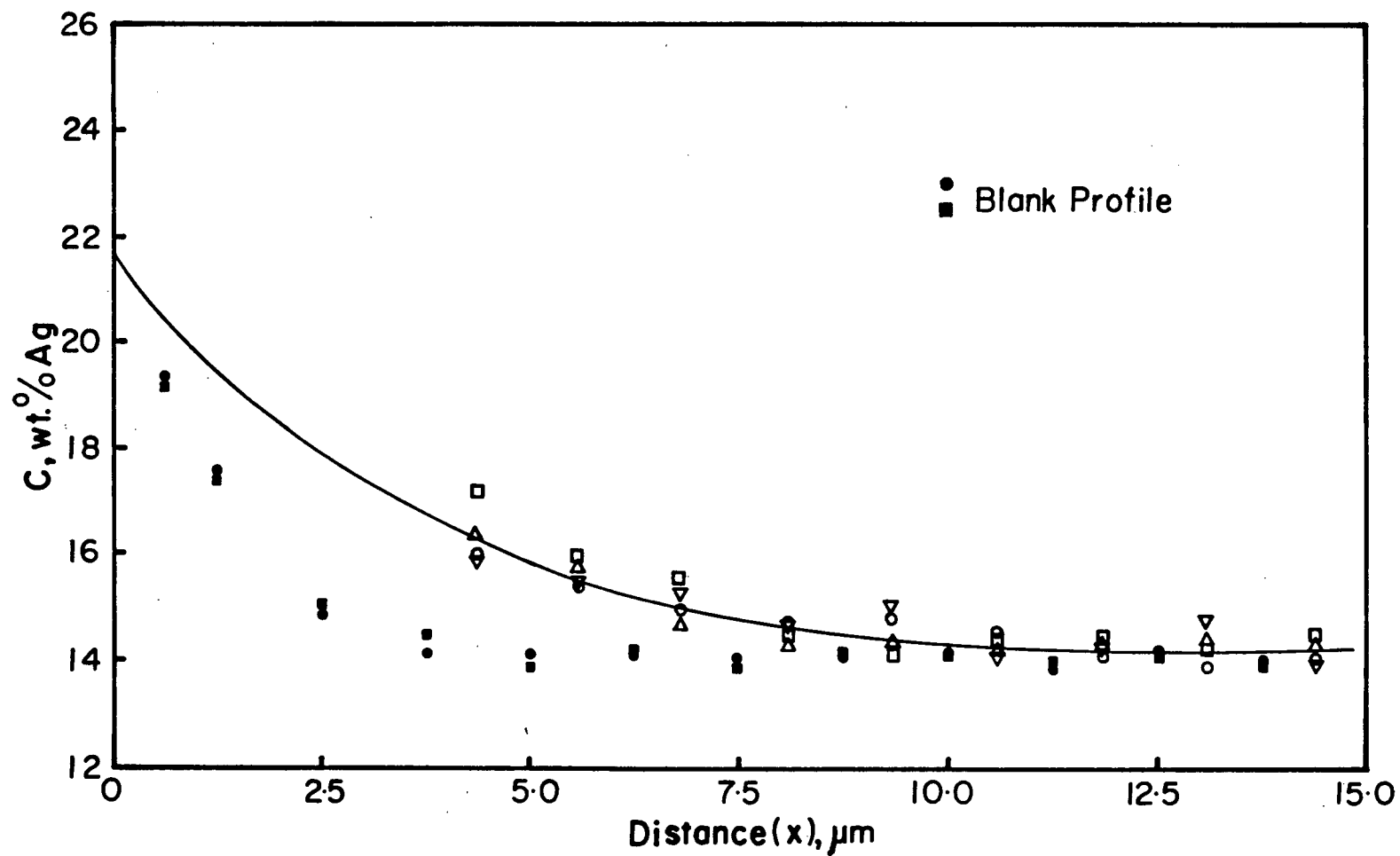


Fig. 15. Concentration profiles on both sides of two precipitates dissolved at 485°C for 10 minutes.

(iii) the diffusion fields from neighbouring precipitates do not overlap; this condition is ensured by the heat-treatment schedules adopted.

(iv) from a mathematical point of view, the planar surfaces of the precipitates are assumed to be infinite in extent and are vertical to the polished surface. Both criteria were reasonably well satisfied because of the very large aspect ratios of the Ag_2Al precipitates.

For these conditions, the concentration profile ahead of a dissolving plate is given by:

$$\frac{C(x,t) - C_M}{C_I - C_M} = 1 - \operatorname{erf} \frac{x}{2\sqrt{Dt}} \quad \dots 7$$

where: C_I is the solute concentration at the precipitate matrix interface and C_M is the matrix concentration. $C(x,t)$ is the solute content of the matrix at a distance x from the boundary and t is the duration of the solution heat treatment.

Values of C_I and D were obtained from Equation 7 using the following graphical analysis originally developed by Hall et al.:²⁰

(i) For three values of x ($x = 7.5 \mu\text{m}$, $12 \mu\text{m}$ and $18 \mu\text{m}$) the corresponding experimental values of $C(x,t)$ were obtained from Fig. 16 and were used in conjunction with a range of $(Dt)^{0.5}$ values to solve Equation 7. The graph of C_I vs. $(Dt)^{0.5}$ (Fig. 16) consists of three curves which cross at

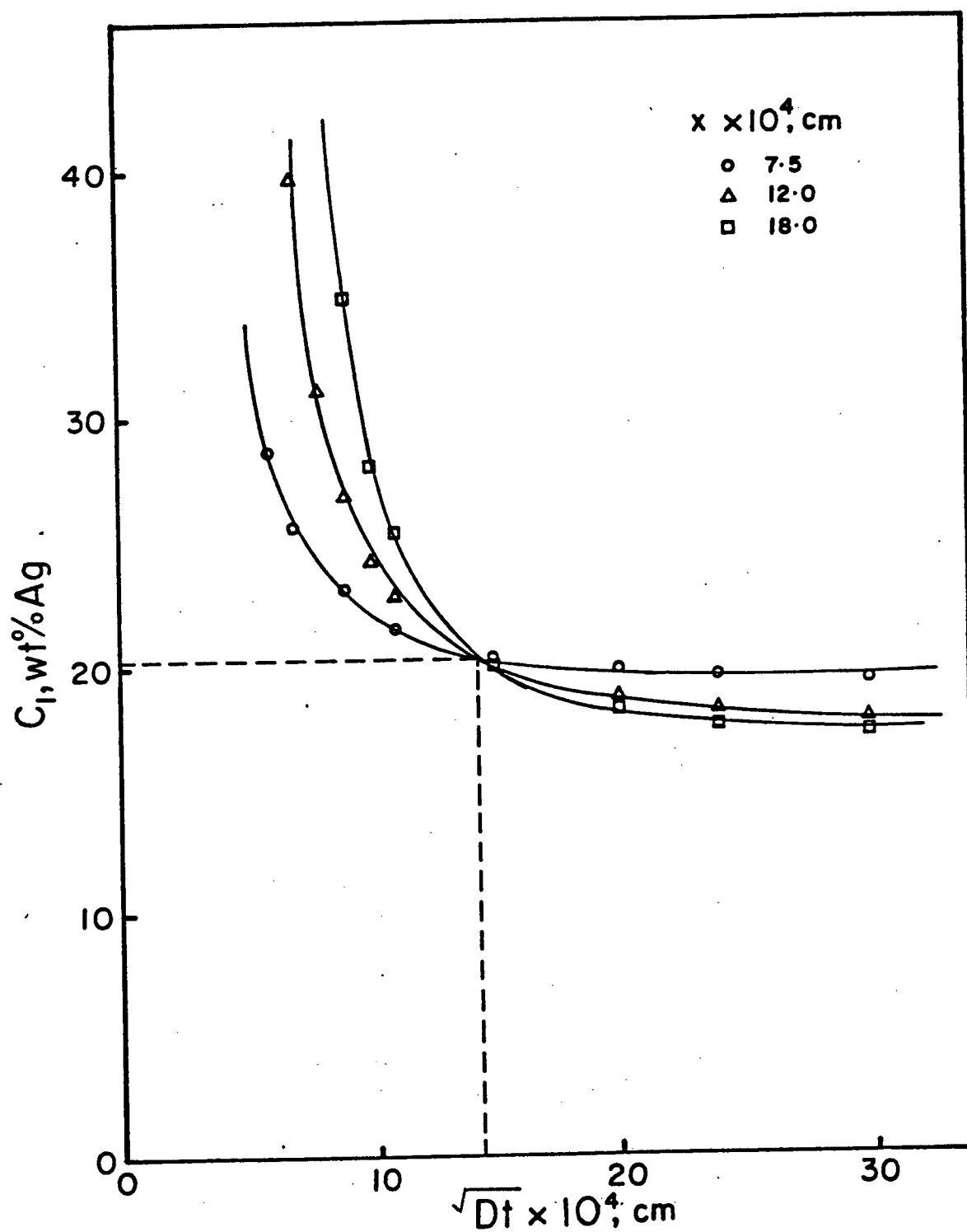


Fig. 16. Interface concentration C_I versus \sqrt{Dt} at 485°C .

a point corresponding to approximate values of C_I and $(Dt)^{0.5}$

(ii) A plot of:

$$(C_{(x,t)} \text{ versus } \operatorname{erf} \left[\frac{x}{2(Dt)^{0.5}} \right])$$

was made using the value of $(Dt)^{0.5}$ obtained from Fig. 16.

This is a linear plot which is consistent with Equation 7.

When extrapolated to

$$\operatorname{erf} \left[\frac{x}{2(Dt)^{0.5}} \right] = 0$$

a more accurate value of C_I is obtained as shown in Fig. 17.

(iii) Accurate values of D were obtained by plotting

$$\frac{C_{(x,t)} - C_M}{C_I - C_M} \text{ against } x$$

on a probability scale. D can be calculated from the slope of the line in Fig. 18 which is equal to $\frac{1}{2(Dt)^{0.5}}$

(iv) Iteration of (ii) and (iii) was used to determine more accurate values of D and C_I in some cases.

Table VII shows the values of C_I and D determined using this procedure for a number of precipitates.

In the case of the 485°C results, the C_I values shown in Table VII have a mean value of 21.88 wt.% Ag with a standard deviation of 0.10 slightly less than the equilibrium solubility value of 22.3 wt.% Ag. This consistent drop in the

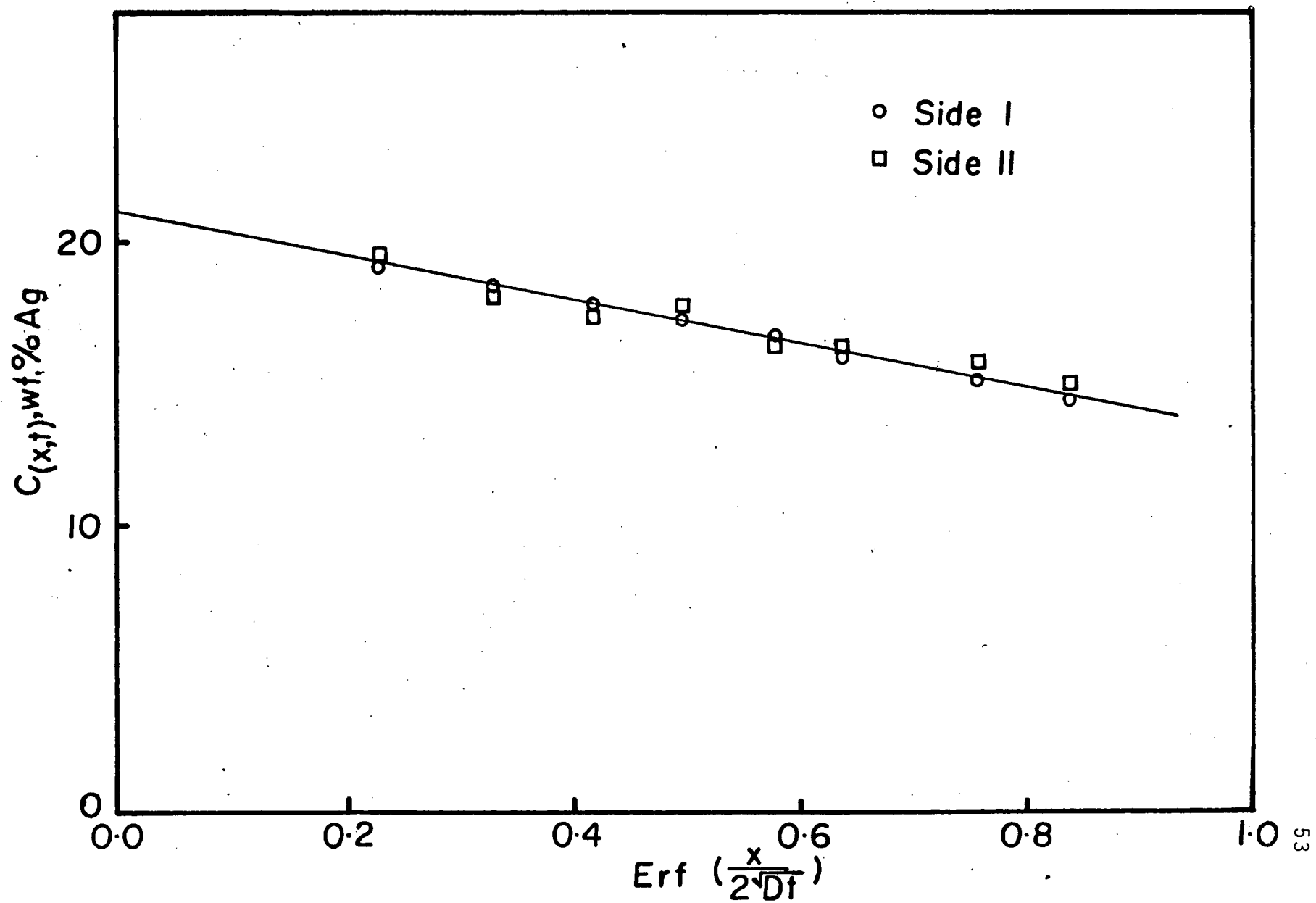


Fig. 17. C versus $\text{erf} \frac{x}{2\sqrt{Dt}}$ at 485°C .

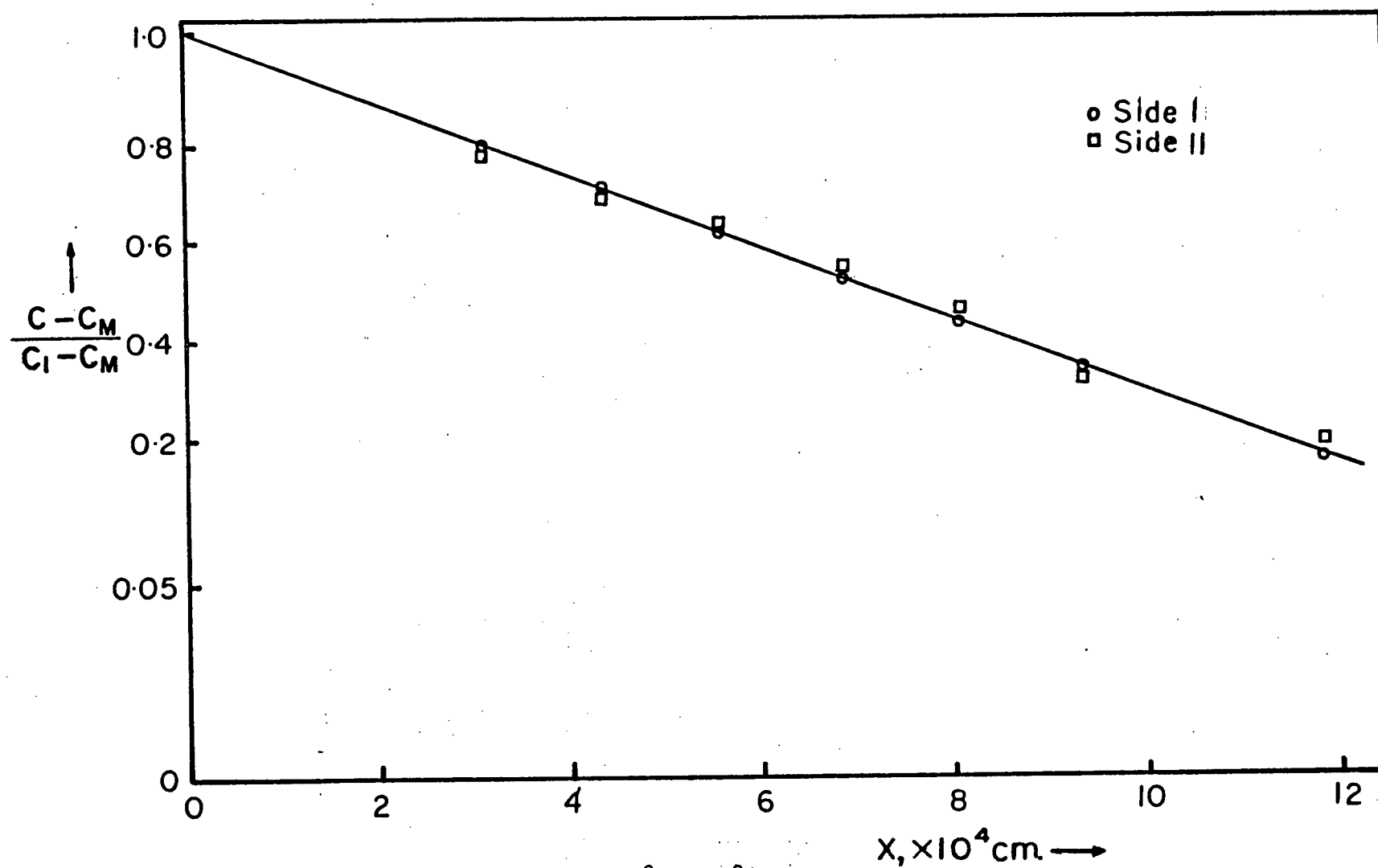


Fig. 18. Probability plot of $\frac{C(x,t) - C_M}{C_I - C_M}$ versus diffusion distance, x .

experimental C_I values though not overwhelmingly definitive does depict a clear trend. The corresponding diffusion coefficients are however in good agreement with literature bulk diffusivities, see Table VII.

Comparison of the results for the two sides of a precipitate show that C_I and D were identical in most cases (Table VII), confirming the reproducibility of the profiles. The few cases where an asymmetry of profiles was observed may be attributed to precipitates inclined to the surface of polish. Soft impingement from sub-surface precipitates could also contribute to this asymmetry.

The activation energy for volume diffusion has not been evaluated from these results, as the good correlation between individual volume diffusion coefficients and literature values reasonably demonstrates the consistency and accuracy of the measured profiles.

The deviation of C_I from equilibrium solubility values tends to indicate interface control for the reaction. If indeed the reaction were interface controlled, a varying silver concentration at the phase interface would occur. No such variation has been made evident, owing to the single solution treatment time used. For such an analysis the Linear Flux model would be most adequate. This assumes that C_I varies linearly with time. However it has been shown^{21,22} that this model gives C_I values comparable to the error function analysis adopted which assumes a constant value of C_I throughout the dissolution process.

Table VII. Electron-probe Determination of Interface Concentration (C_I) and Volume Diffusion Coefficients (D_V) for the Broadface.

Temp: 485°C			Time: 600 sec.		$C_E = 22.2\text{wt\% Ag}$	
Ppt. #	Side 1		Side 2		Mean Values	
	$C_I \text{ \% Ag}$	D ($\times 10^{-9} \text{ cm}^2 \text{ sec}^{-1}$)	$C_I \text{ \% Ag}$	D ($\times 10^{-9} \text{ cm}^2 \text{ sec}^{-1}$)	C_I	D ($\times 10^{-9} \text{ cm}^2 \text{ sec}^{-1}$)
1	21.85	0.87	21.77	0.74	21.81	0.81
2	21.81	0.92	21.93	1.06	21.87	0.99
3	21.79	0.75	21.87	0.99	21.83	0.87
4	21.73	0.91	21.75	0.97	21.74	0.94
5	22.04	1.01	22.00	0.82	22.02	0.92
6	21.90	0.73	21.96	0.77	21.93	0.75
7	21.92	0.67	21.88	0.73	21.90	0.70
Temp: 474°C Side 1			Time: 12 mins Side 2		$C_E = 19.50 \text{ wt\%}$ Mean Values C_I D	
1	18.71	0.57	18.88	0.62	18.79	0.59
2	18.82	0.76	18.69	0.81	18.75	0.79
3	19.03	0.65	18.84	0.66	18.94	0.66

Results of the measured profiles in combination with equivalent kinetic data were used to investigate the flux balance across the precipitate interface. The area underneath the concentration distance profile was first calculated and corresponded to the solute discharged from the dissolving broadface. This area is denoted region A in the schematic diagram of Fig. 19. The resulting displacement (x) of the interface was subsequently obtained by a mass-balance calculation across the boundary. For the profile of Fig. 15, corresponding to dissolution at 485°C for 10 minutes, an interface displacement of 1.45 μm was calculated.

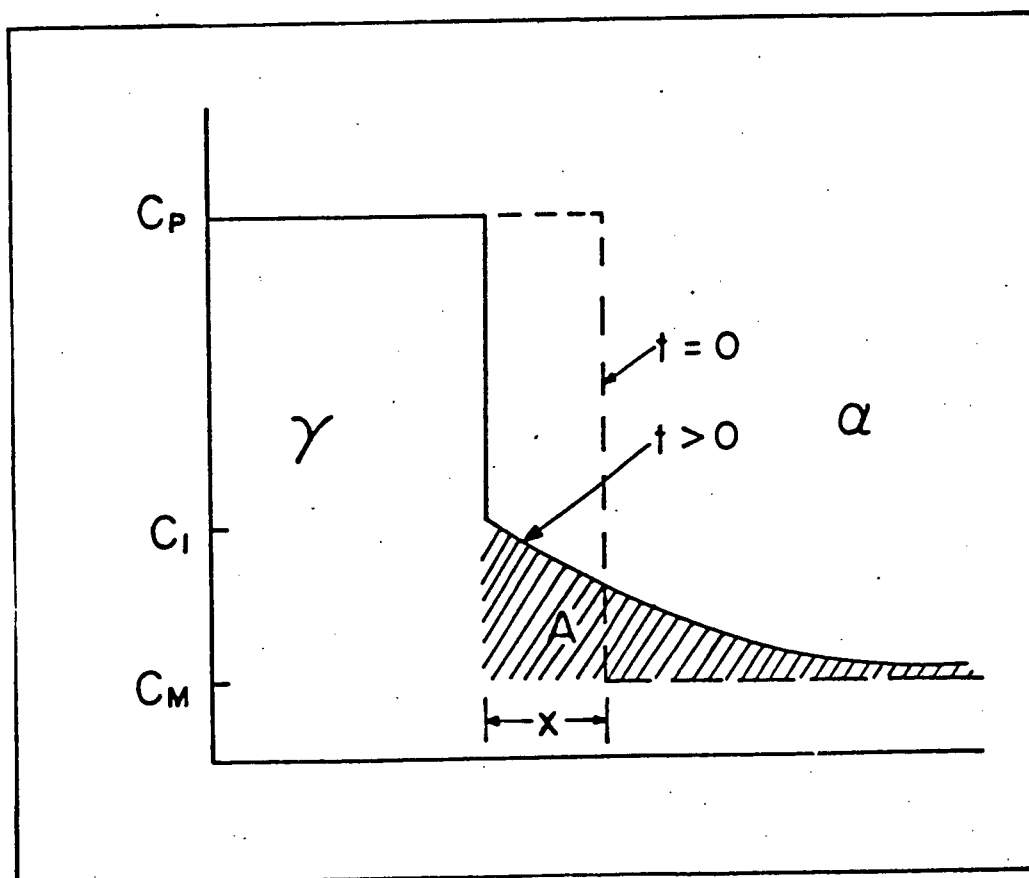


Fig. 19 Schematic diagram for the flux balance calculation.

By comparison, the actual migration of the interface measured directly in the kinetic study was 0.27 μm . This is less than $\frac{1}{5}$ of the value obtained from the composition profile. This rather striking difference clearly suggests an excess of solute adjacent to the broadface. The origin of this extra solute will be discussed shortly.

3.4.3 Tip Profile

Fig. 20 shows a typical concentration profile for dissolution at 485°C. Measurements closer than 3.5 μm to the tip have not been used because of the spot size of the beam. Profiles were fitted to the Horvay-Cahn analysis. The relevant equation from solving the steady-state diffusion equation is given as:

$$\frac{C_{(x,t)} - C_M}{C_I - C_M} = \frac{\text{erfc} \left(\frac{vx}{2D} \right)^{0.5}}{\text{erfc} \left(\frac{vx_1}{2D} \right)^{0.5}} \quad \dots 8$$

where x_1 = radius of curvature at the tip

x = distance from the origin

and v = velocity of the moving tip.

A concentration ($C_{(x,t)}$) versus distance (x) plot calculated on the basis of Equation 8 was superimposed on a measured profile at 485°C, see Fig. 20. The data used for this purpose were taken from the kinetic study and are:

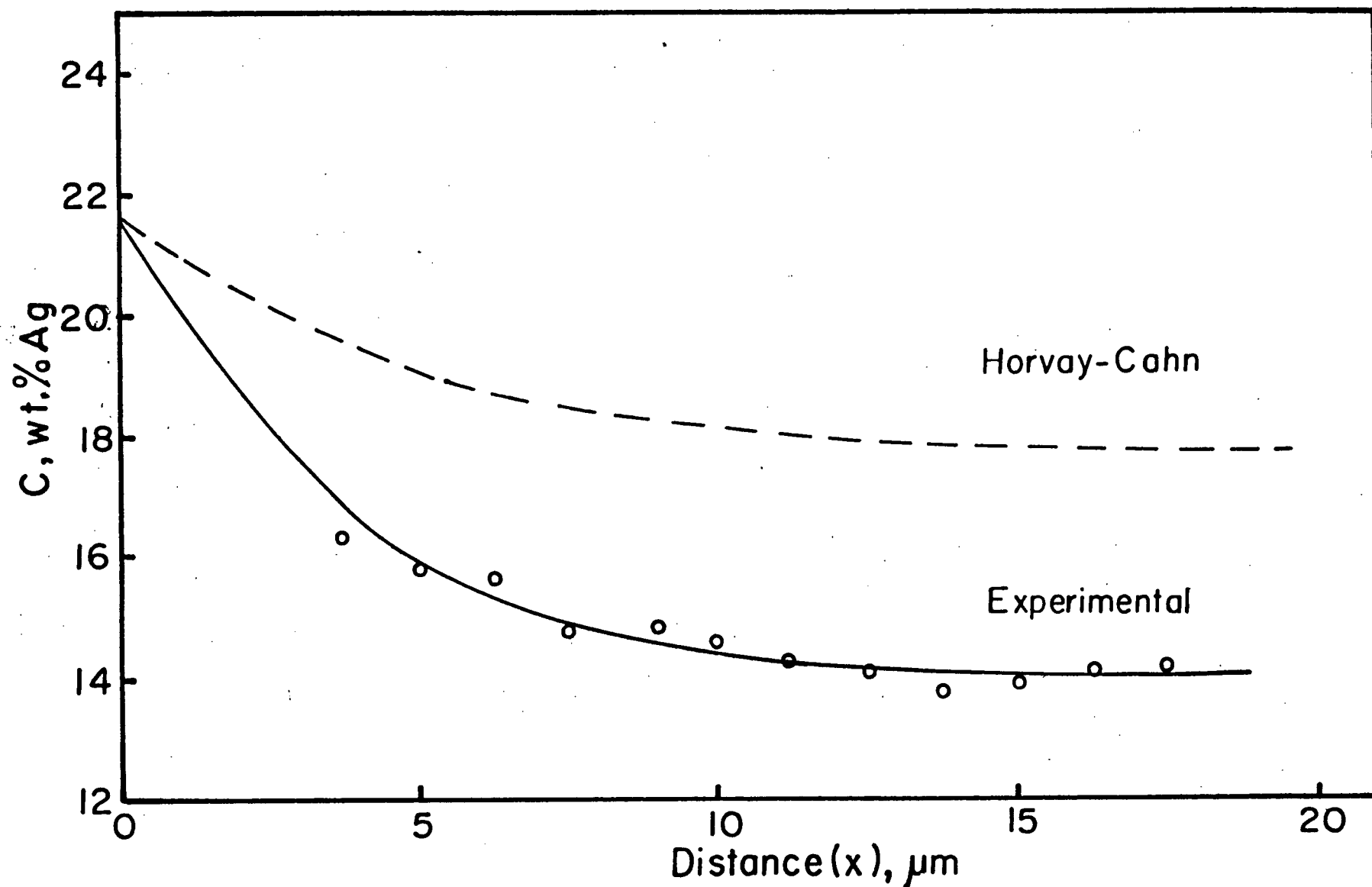


Fig. 20. Comparison of experimental and calculated (Horvay-Cahn) profile for a tip (solution treated at 485°C for 10 minutes).

$$v = 9.3 \times 10^{-7} \text{ cm sec}^{-1}$$

$$x_1 = 4.0 \times 10^{-5} \text{ cm}$$

$$x = 6 \times 10^{-4} \text{ cm}$$

$$\text{and } D = 1.81 \times 10^{-9} \text{ cm sec}^{-1}$$

It can be seen that the fit is poor. Very notable is the fact that much less solute than expected is present at larger distances from the tip.

A fit to the infinite planar Error Function model was attempted as was done for the broadface analysis. The assumptions entailed in this analysis are obviously inappropriate in view of the fact that the tip is significantly displaced and that there is curvature. The fit was surprisingly good however. Bulk diffusivities calculated were identical to literature values. C_I values obtained were slightly lower than equilibrium values and similar to those obtained at the broadface.

Very little weight can be placed on the results of this latter analyses for obvious reasons. However the overall poor fit to the Horvay-Cahn analysis cannot be easily explained. One would expect on the basis of the successful fit to the kinetic data that it would be equally applicable to the profiles. However the diffusion fields have seemingly been altered by some form of solute transport away from the tip.

3.4.4 Isoconcentrate Contours

Representative isoconcentrate contours at two temperatures 474°C and 485°C are plotted in Fig. 21. The contours correspond to the diffusion field surrounding the half length of a precipitate. The contours all run at approximately constant distances from the surface of the precipitate and clearly show the comparable diffusion distances at the tip and at the broadface discussed above.

Because of the poor agreement of the composition profiles with those expected from the kinetic measurement it was felt necessary to confirm the experimental results by carrying out an overall solute balance.

First the total amount of solute discharged into the matrix from the dissolving precipitate was calculated, taking the relevant data from the kinetic study. This corresponds to the single hatched area of Fig. 22. The solute transported into the matrix was measured from the area under the concentration-distance curve, summed over the entire precipitate surface. This area is described by the broken line contours of Fig. 22. The details of the calculation are presented in Appendix III.

It was found that the total extra solute present in the matrix was within 6% of the solute lost from the dissolving precipitate, thus confirming the experimental results.

It thus appears that the measured composition profiles

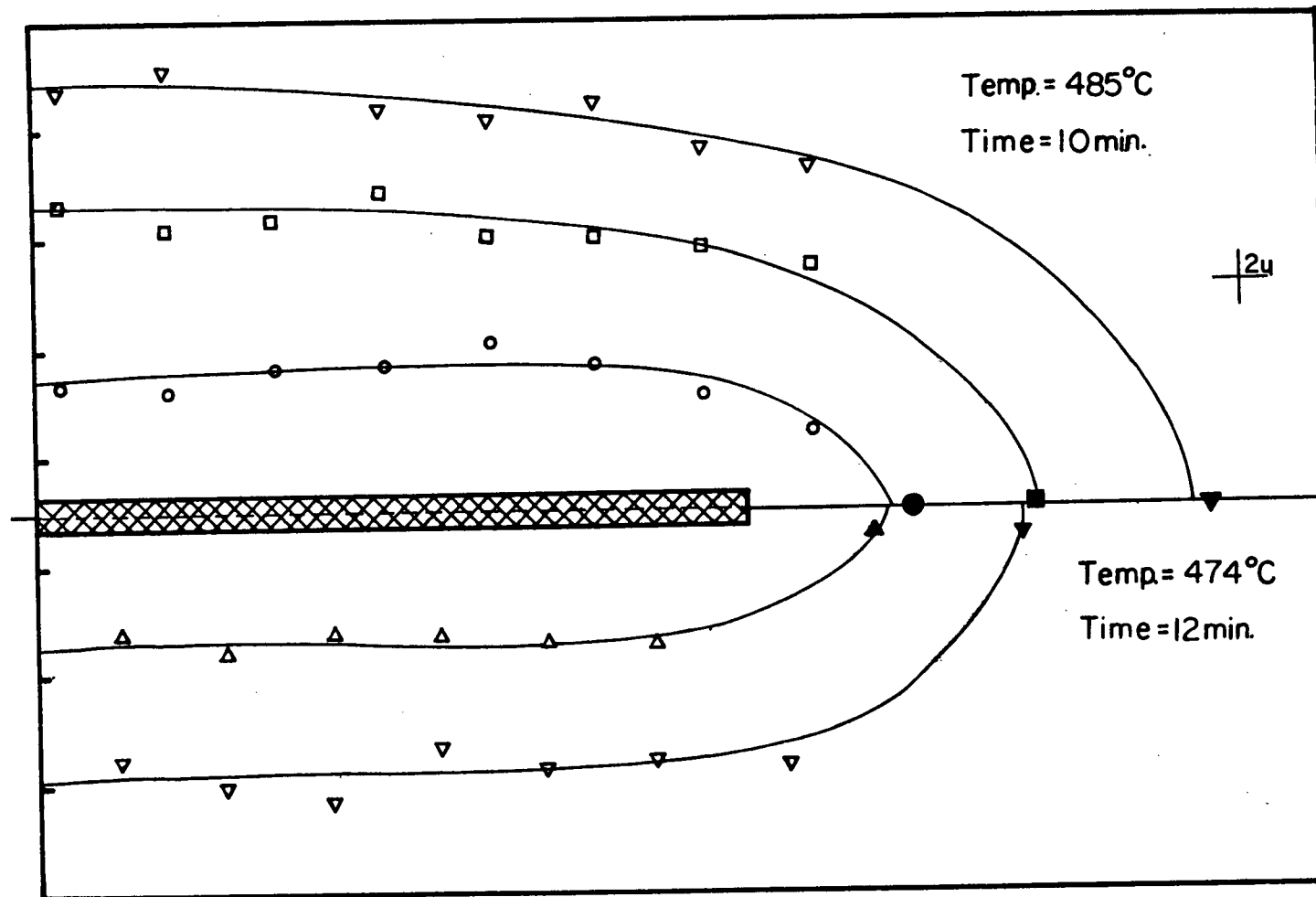


Fig. 21. Isoconcentration contours at 485°C and 474°C.

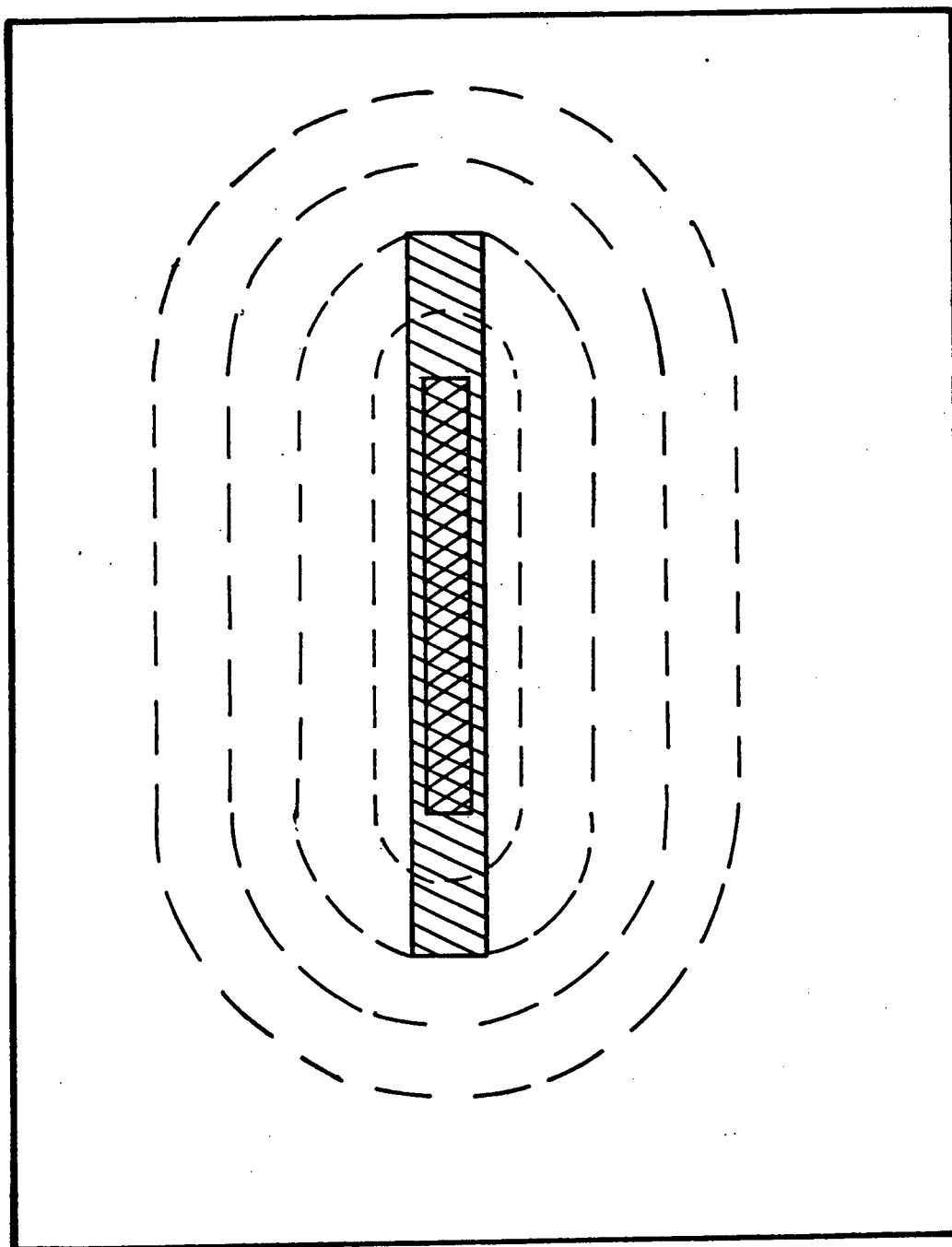


Fig. 22. Schematic diagram for solute conservation calculation. The single hatched lines represent the initial shape of the precipitate. The broken lines represent composition contours round the precipitate.

are correct and that the lack of agreement with the kinetic results is due to flux of solute not anticipated in the kinetic theories. In particular, it indicates a transfer of solute from in front of the tip to the broadface thus giving less solute at the tip and more solute adjacent to the broadface than expected. The details of this suggested mechanism will be presented in the discussion section.

4. SUMMARY AND DISCUSSION OF RESULTS

4.1 Introduction

It has been shown that Widmanstätten Ag_2Al plates shorten at a linear rate which according to the Horvay-Cahn, Zener-Hillert and Jones-Trivedi theories is volume diffusion controlled. Agreement between all three models were found to be remarkably good. Laird et al.¹⁷ have studied the growth kinetics of γ plates in Al-15 wt.% Ag using transmission electron microscopy. They find a linear growth rate which is in good agreement with volume diffusion control. Thus the mechanism of lengthening and shortening in γ Ag_2Al appear to be similar.

As discussed in the introduction there are no measurements of shortening in the literature. There are however a number of observations of precipitate edge growth. Simonen et al.²⁴ demonstrated that the lengthening of Fe_3C plates in low carbon steel, α_1 plates in Cu-Zn and α plates in Ti - Cr could all be described by the Jones-Trivedi equation.

The situation is different in several other cases however θ' plates in Al-4% Cu,^{25,27} α_1 plates in β' Cu-Zn^{38,39} grow more rapidly than Trivedi's equations predict, whereas bainite and ferrite plates in Fe-C⁴⁰ and Ti - Cr⁴¹ grow more slowly than expected.

The kinetics of thinning were found to be much slower than volume diffusion rates throughout the entire life of the precipitates. This again is in agreement with the growth results of Laird et al.¹⁷ who find thickening slower than volume diffusion rates by more than an order of magnitude.

This it is again found that the mechanisms of growth and dissolution in γ are similar. The tendency for kinetics to be less than volume-diffusion controlled rates appears to be rather general. Slow growth rates have been observed for ferrite plates¹⁸ and Cu-Si plates.²⁸ Observation of volume diffusion controlled thickening^{30,31} is very limited indeed.

Analysis of the composition profiles measured adjacent to the dissolving γ plates indicated interface concentration values slightly lower than equilibrium values. This deviation from local equilibrium has been reported previously²³ for the broadface in dissolving γ Ag₂Al precipitates. It has not been measured heretofore at the precipitate tip. Deviations from local equilibrium have also been reported at the broadface of dissolving Si plates in Al-Si.²² The composition profiles adjacent to the broadface of the precipitate

give diffusion distances expected theoretically from a volume diffusion controlled boundary. Much shorter distances were anticipated on the basis of the kinetic results. It has therefore been suggested that the altered solute field adjacent to the broadface arise from solute transferred from the area of the dissolving tip, the tip concentration profile is found to have less solute than expected from the kinetic measurements.

This transfer of solute can be explained most clearly by comparing the observed composition contours Fig. 23(a) with those that would be anticipated on the basis of the kinetic results. This would suggest a very small diffusion field adjacent to the broadface and a much larger diffusion field adjacent to the tip. This would lead to a dumbbell pattern as shown in Fig. 23(b). It is perhaps not surprising that such a pattern is not observed and that the contours are less curved.

It is interesting to note that the measured contours do not show any point effect of diffusion at the tip. This would be seen as a shorter diffusion distance at the tip compared with the broadface Fig. 23(c). This is what would be expected if dissolution at all points of the precipitate were volume diffusion controlled which is certainly not the case here.

The mechanism for the transport of solute atoms from the front of the precipitate tip to the centre of the broadface will now be discussed. The diffusion distances required are at least 40 μm . The volume diffusion distance can be calculated approximately using $x^2 = 2Dt$. Taking D at 485°C to be equal to

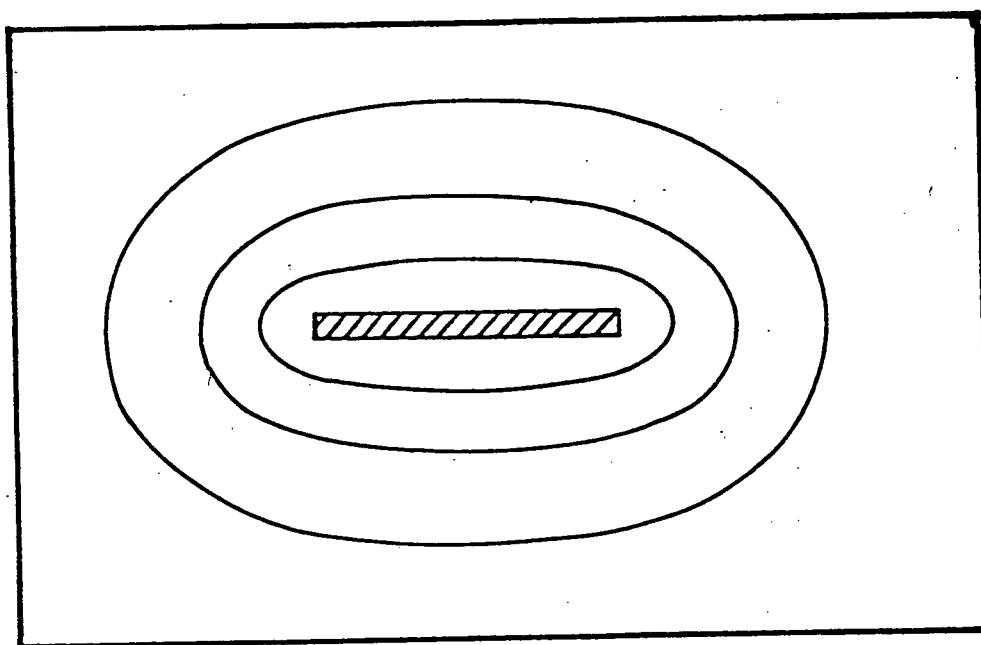


Fig. 23. Schematic concentration profiles associated with dissolving Ag_2Al precipitates

(a) experimentally observed profile.

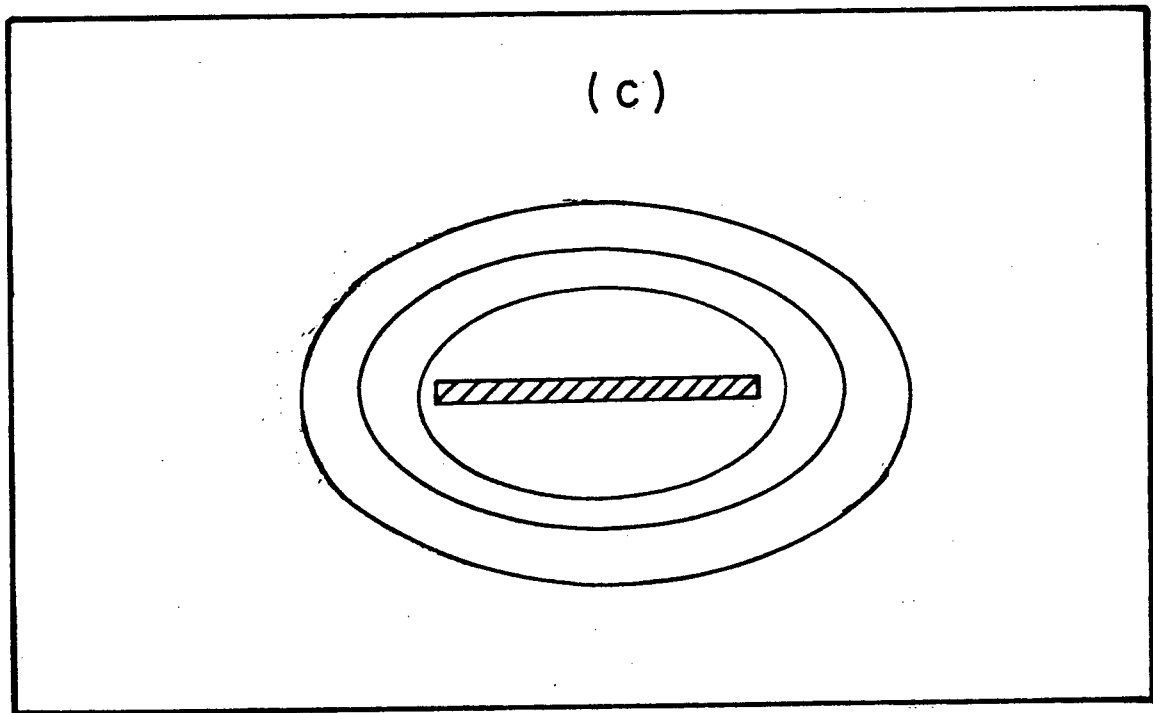
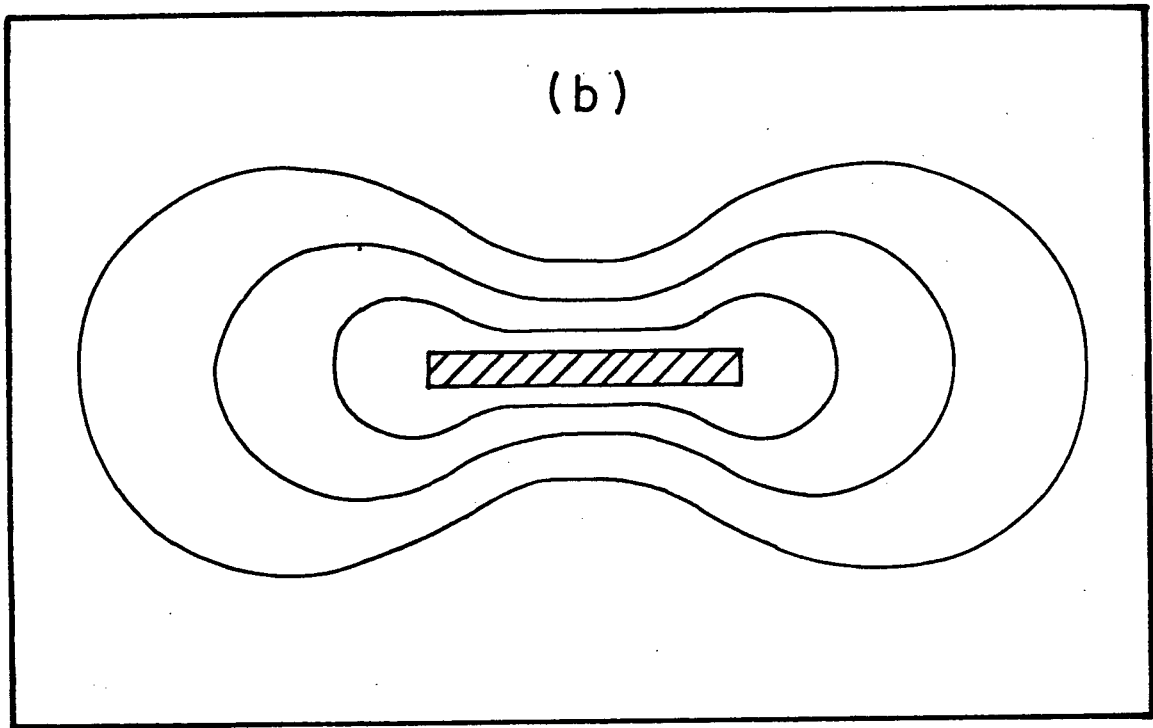


Fig. 23 (b) predicted from kinetic measurements- Dumbbell shaped.

(c) due to the point effect of diffusion- spheroidal shaped.

$1.81 \times 10^{-9} \text{ cm}^2 \text{ sec}^{-1}$ and $t = 10$ minutes, gives a diffusion distance of $15 \text{ }\mu\text{m}$, much less than that required. Thus some mechanism other than volume diffusion appears to be involved for solute transport.

The precipitate : matrix interface seems to be the most natural path. Solute from the dissolving tip is rapidly transferred along the broadface and then moves laterally out into the matrix. Provided the lateral diffusion is fast the diffusion distance at all points on the precipitate i.e. broadface and tip will be the same, as observed experimentally. If any point on the surface were to have a smaller diffusion field adjacent to it, solute would immediately be transferred to the point to eliminate the steep composition gradient. Details of this short circuit diffusion mechanism will be discussed shortly.

4.2 Physical Mechanism of Interface Migration - The Ledge Theory^{5,6}

In the present work, kinetic studies indicate that there is a barrier to diffusional migration on the broadface and so the ledge mechanism may be relevant here. A detailed description of the ledge mechanism now follows.

According to the ledge mechanism, a barrier to normal diffusional migration is present when there is a partial or fully coherent boundary. Partially coherent boundaries contain misfit dislocations, Fig. 24(a). Fully coherent boundaries do not and are equivalent to an extension

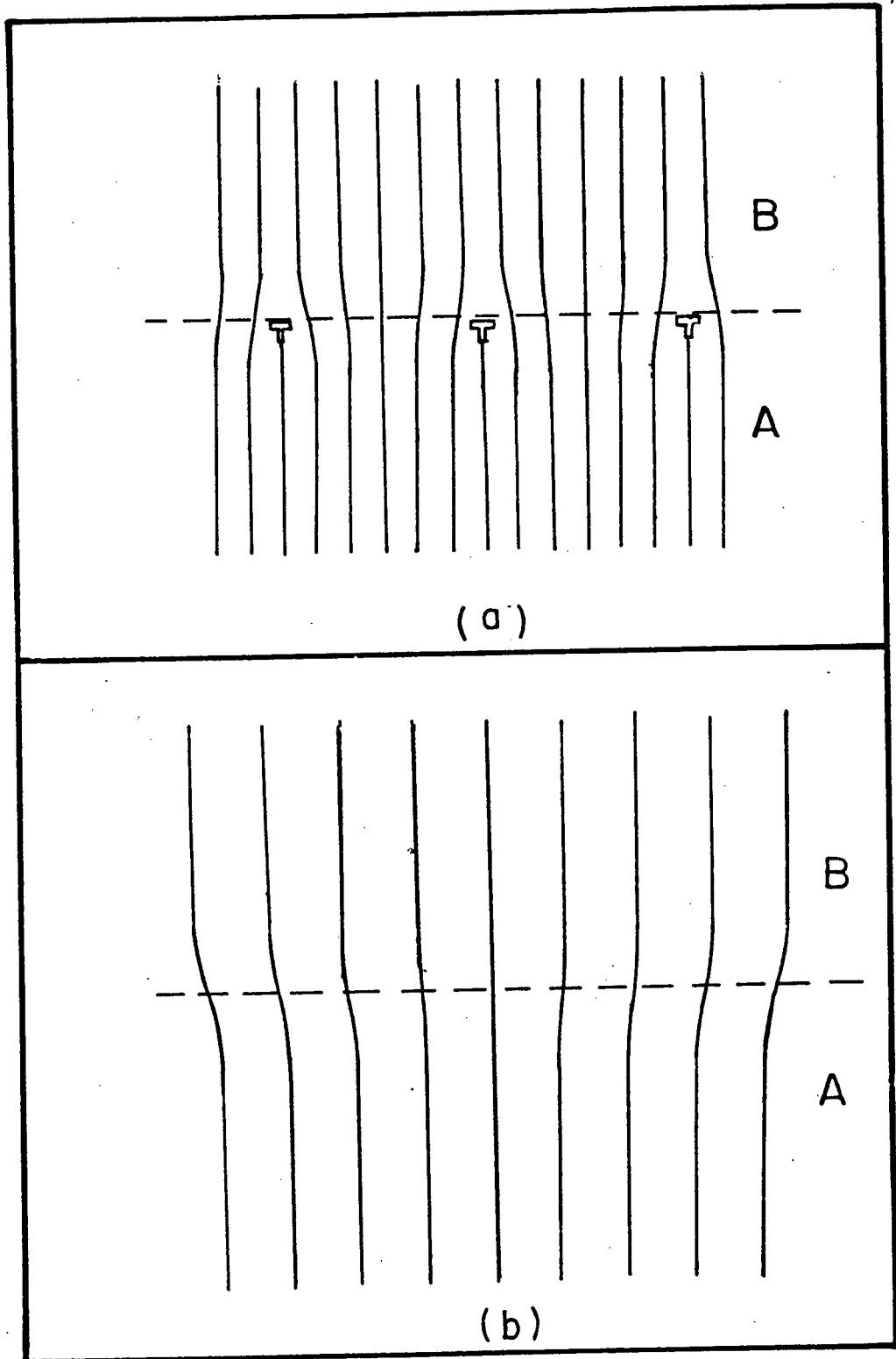


Fig.24 Schematic representation of
(a) semi-coherent interface containing some dislocations and some strain.
(b) coherent interface maintained by elastic strain.

of the stacking sequence of one crystal into the first layer of the other with no more than elastic distortions in the vicinity of the interface, Fig. 24(b).

The barrier to migration arises when the crystal and matrix have different crystal structures. Displacement of the boundary would then involve a change in the order of atom stacking across the interphase. This can only be accomplished by fitting atoms of the migrating phase bound for substitutional sites into the interstices of the other phase, Fig. 24(c). This is energetically unfavourable and therefore the boundary remains immobile.

Migration of such interfaces can be envisaged as taking place by means of ledges, a familiar phenomenon previously associated with vapour-solid and liquid-solid phase transformations.

Ledges found on the interphase boundary have semi-coherent flat faces to enable good atom matching across the interface but the step faces are usually considered incoherent. This means that atoms leave or enter the precipitate phase only at the step and no passage of solute occurs across the broadface. Thus the growth velocity of the face (G) is determined by the lateral velocity (v), height (h) and spacing (λ) of individual steps according to the relation

$$G = av/\lambda$$

The edge always moves at volume diffusion rates.

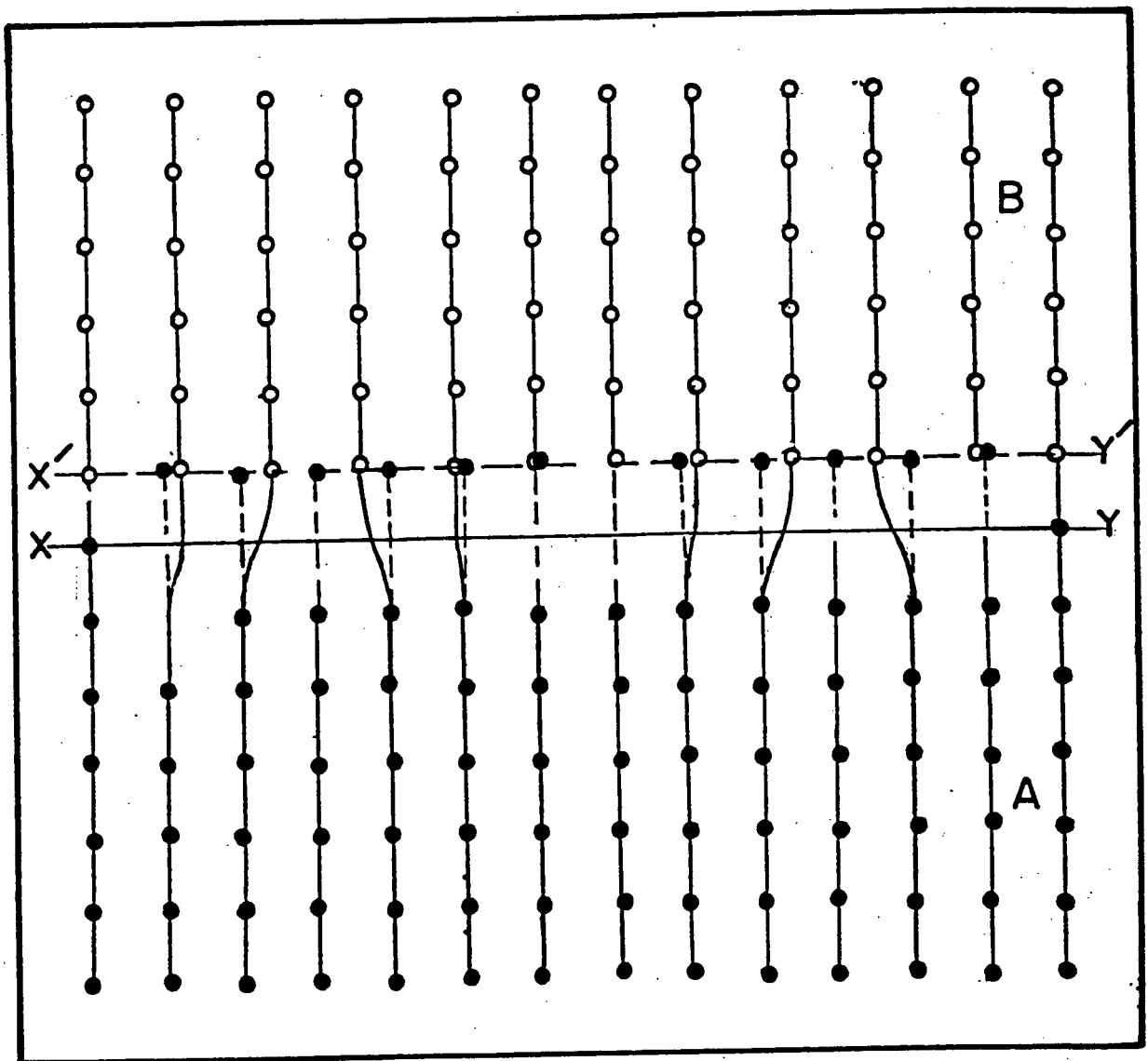
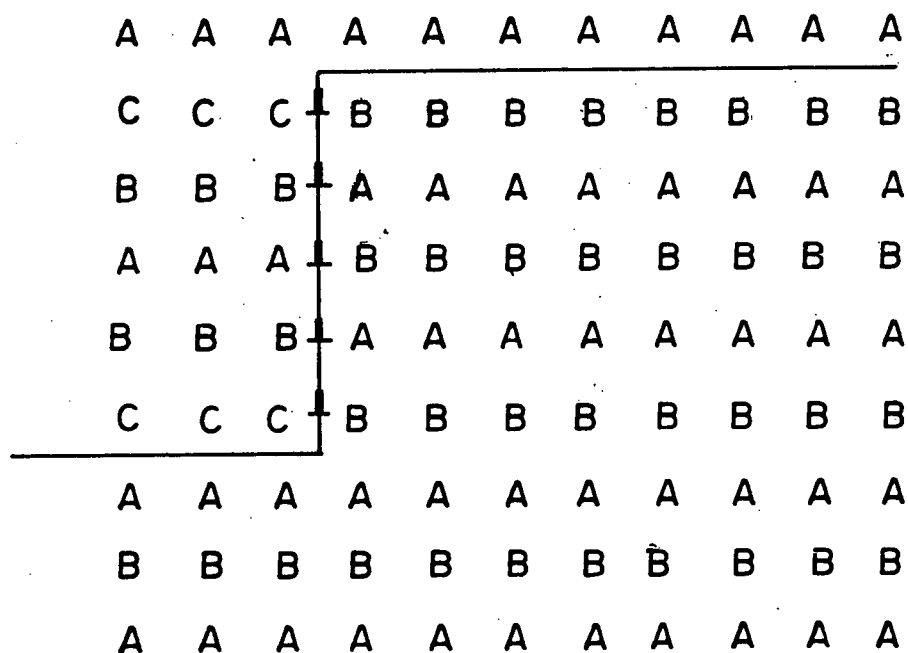
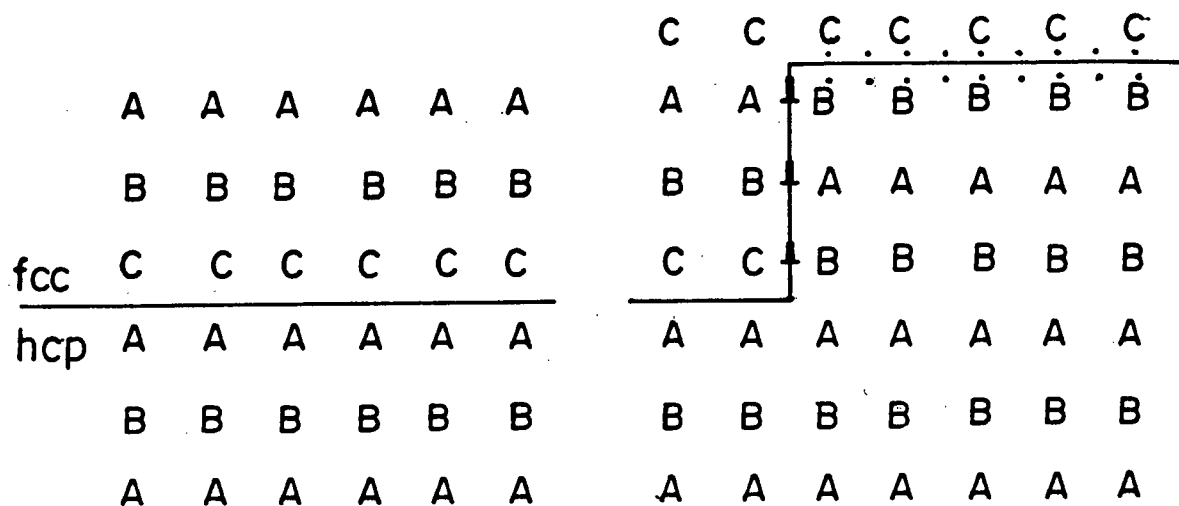


Fig. 24 (c) semi-coherent boundary migrating from XY to $X'Y'$ showing A atoms(\bullet) lodging in the interstices of B

There are a number of models for the detailed structure of ledges. Fig. 25 shows the possible structure at a fcc-cph interface. An unstable packing situation arises for a single and double layered ledges, the three and five layered ledges being more stable.

On the basis of this mechanism, migration can occur at coherent and semicoherent interfaces only with the aid of ledges and if these ledges are not available in a sufficient density, migration is inhibited. It is worth mentioning at this point that growth or dissolution ledges described above differ from structural ledges^{42,43} which appear at boundaries across which good matching is not initially obvious e.g. an fcc : bcc interface.

Much of the discussion on ledges so far has been theoretical in nature. The experimental evidence for ledge growth is less complete. Weatherly¹⁵ has shown some strong evidence for the presence of ledges on θ' plates in Al-Cu. A summary of ledge observations has been given by Aaronson.⁴⁴ There is relatively little direct evidence for nucleation of ledges and whether they in fact have incoherent edges. Weatherly,¹⁵ for example, shows that the strain fields associated with the edge of ledges indicate a partially coherent boundary and one that would be immobile. Laird et al.⁴⁵ have shown growth kinetics in a number of precipitates which appear to follow a step-wise growth. They postulate that



Stacking fault.



Interface between hexagonal and face centered cubic phases.



Array of partial dislocations.

Fig. 25. Growth of lower cph phase from upper fcc by random atomic jumps.

each increment of growth is associated with passage of a ledge past the point of measurement. These, however, have to be superledges and their relationship with the atomic sized ledge expected theoretically is unsure.

4.3 Kinetics of Dissolution of $\gamma(\text{Ag}_2\text{I})$ -

The Ledge Mechanism

Laird et al.⁴⁵ observed parallel arrays of dislocations at the edge of γ' plates using transmission electron microscopy. Their results together with kinetic studies of others (see Section 4.1) have led to the general belief that the plate edges are indeed partially coherent. One would therefore expect ledges to control edge migration. For a smoothly curved edge there will be a very high ledge density and so dissolution can occur at volume diffusion rates (Fig. 26) as observed experimentally.

The kinetics at the broadface are slower than volume diffusion controlled rates and this implies a deficiency in ledge supply. Laird and Aaronson⁴⁶ have shown experimentally that the nature of ledges at the broadface of the transition γ' plates appear to be identical during thickening and thinning. A similar condition appears plausible for the equilibrium γ plates. However, there does not seem to be any ready justification for the dearth of ledges in thinning which would be necessary to explain the slow dissolution kinetics. Plate edges have been known¹⁵ to serve as prolific

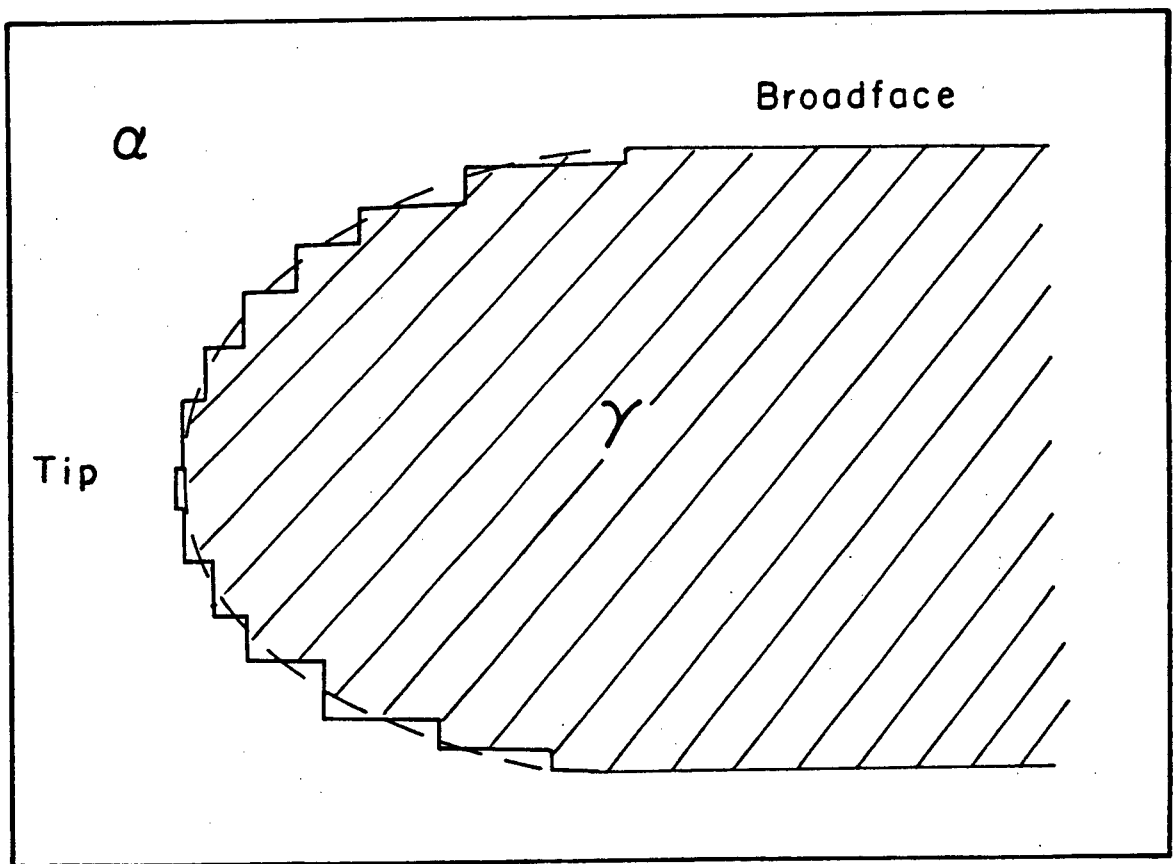


Fig. 26. Ledge structure at the edge of a precipitate.

sources during dissolution since ledge nucleation occurs readily at these locations and the ledges then migrate inwards towards the centre of the plate. It can be seen that it is hard to apply the ledge mechanism in the present situation. Certainly there is a barrier to the migration of the broadface and this could be explained assuming that there are three layer high ledges of the type shown in Fig. 25(b) located about 600\AA apart. However it is not at all obvious why they do not approach one another more closely to give a faster dissolution rate since there should be no shortage of ledges due to nucleation. It may perhaps be related to strain field interaction between ledges. However it is not possible to discuss this in detail.

4.4 Overall Mechanism of Dissolution

It has been established in the present study that the diffusion fields adjacent to the tip and broadface interact. The ledge and misfit dislocation networks known to exist at the interface serve as short circuit diffusion paths for solute transport from the edges to the broadface. The solute atoms on reaching a suitable point on the broadface disperse into the matrix by the normal volume diffusion process. It has been observed that γ plates have intricate interface dislocation networks⁴⁴ and these would be expected to act as short circuit diffusion paths.

The suggested mechanism fits the observed results very satisfactorily. However there are two potential problem areas which will now be considered.

Interfacial diffusion is generally considered to be similar to grain boundary diffusion. However, boundary diffusion studies indicate that it only becomes a dominant mechanism of transport at relatively low homologous temperatures (T_H). Pasparakis and Brown⁴⁷ for example, find in the dissolution of grain boundary allotriomorphs in Al-Cu alloys that grain boundary diffusion predominate only at temperatures $T_H < 0.72$. In the present work dissolution occurs at high temperatures corresponding to $T_H = 0.82$ and thus interfacial diffusion might not be expected to occur here. However so little is known about interfacial diffusion the analogy with grain boundary diffusion may not be correct.

A second problem is that the suggested mechanism requires a large fraction of the solute from the tip to disperse by interfacial diffusion. However the shortening kinetics were analyzed by the Horvay-Cahn, Zener-Hillert and Jones-Trivedi models which all assume only volume diffusion at the tip. They are therefore not immediately applicable in the present case. It is perhaps surprising that the models used give such excellent agreement with literature values of the diffusion coefficient. The agreement is too good to be just fortuitous. It must be

remembered however that ultimately solute from the tip is dispersed by a volume diffusion process and so qualitatively the models used may still be applicable.

The present mechanism in which misfit dislocations girdling the plates serve as "rejection lines" is analogous to the "rejection plate" mechanism for grain boundary allotriomorphs. In this model, the grain boundary allotriomorphs dissolve via a three step process.

- (i) diffusion of rejected solute along the interphase boundary of the allotriomorphs to the grain boundary.
- (ii) diffusion of solute along the grain boundaries, and
- (iii) volume diffusion of solute from the grain boundaries into the matrix.

Aaronson et al.²⁷ have made use of a similar mechanism to explain observed accelerated lengthening of θ' plates in Al-Cu. The general concept of interfacial diffusion has been used in many more systems in reference to Widmanstätten plates, but there is yet to be a direct study of this effect. Sankaran et al.'s²⁹ study on θ' (Al-Cu) needs mentioning in this regard. They observed that plates whose broadfaces are fully coherent exhibit accelerated interface diffusion and that those whose broadfaces are partially coherent do not.

5. CONCLUSIONS

The results of the present study of the dissolution behaviour of Widmanstätten Ag_2Al precipitates yield the following conclusions:

1. Widmanstätten Ag_2Al precipitates shorten at volume diffusion controlled rates.
2. The thinning kinetics at the broadface indicate an interface controlled reaction.
3. The precipitate : matrix interface dislocation network serves as a conduit for solute transport from the tip to the broadface of dissolving precipitates.
4. An elliptical disc diffusion contour of equal length in front of the tip and across the broadface was obtained for the dissolving plates.
5. The ledge mechanism may be used to describe the dissolution of both the precipitate tip and broadface. The apparent dearth of ledges at the broadface is however not readily justifiable.
6. A similar mechanism seems to govern both growth and dissolution of Ag_2Al precipitates.

7. The overall mechanism of dissolution can only be properly understood by complementing kinetic measurements with electron-probe studies.

BIBLIOGRAPHY

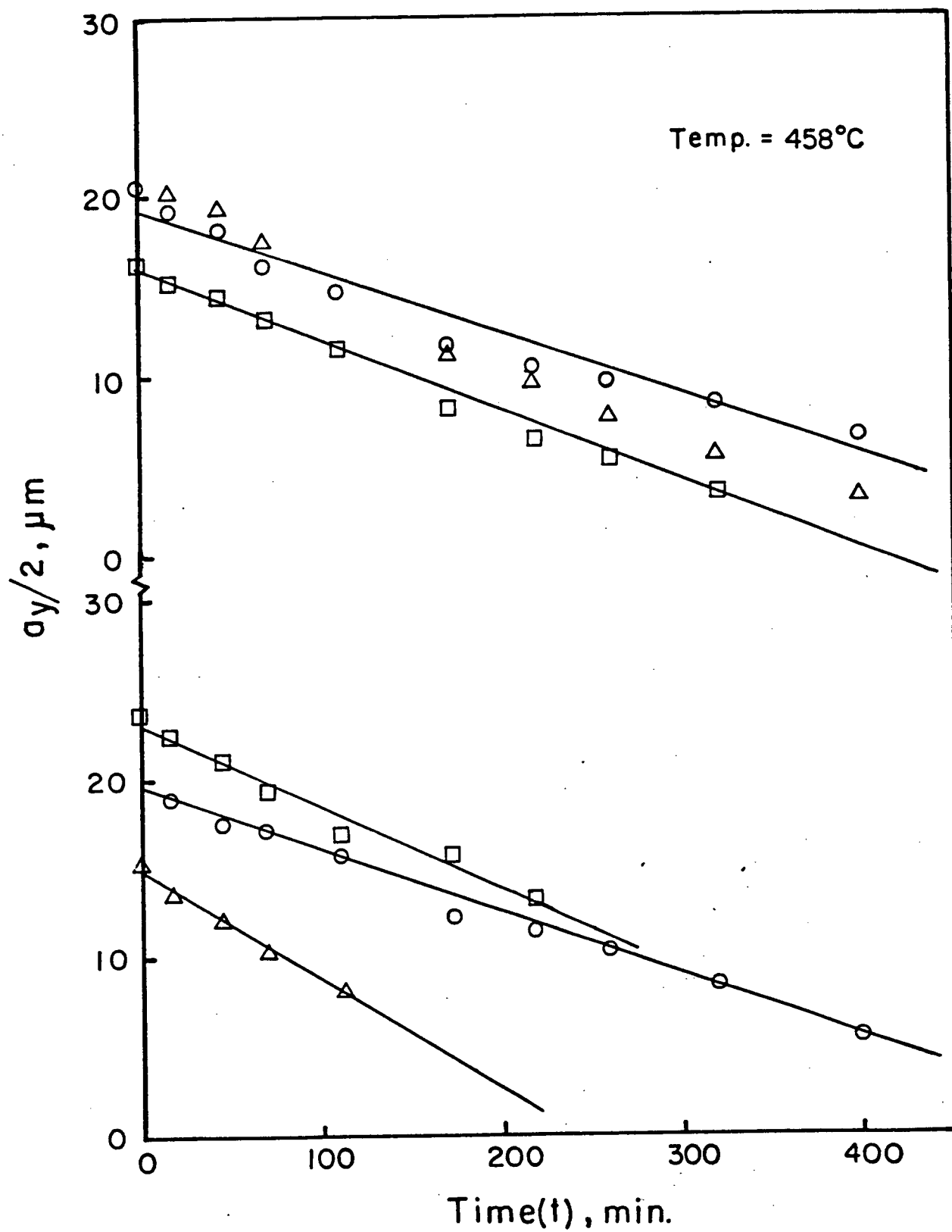
1. Dube', C.A., Ph.D. Thesis, Carnegie Inst. of Technology,
Dube', C.A., Aaronson, H.I. and Mehl, R.F., Rev. Met.,
55, 201, (1958).
2. Aaronson, H.I., The Mechanism of Phase Transformation
in Metals, Inst. of Metals Monograph 18, 47 (1956).
3. Lieberman, D.S. in Phase Transformations, ASM, 1 (1970).
4. Clark, H.M. and Wayman, C.M., *ibid*, 59.
5. Aaronson, H.I., Laird, C. and Kinsman, K.R. in Phase
Transformations, ASM, 313 (1970).
6. Aaronson, H.I. in Decomposition of Austenite by Dif-
fusional Processes, Interscience, 387 (1962).
7. Wechsler, M.S., Lieberman, D.S., and Read, T.A., Trans.
AIME 194, 1503 (1953).
8. Gaunt, P. and Christian, J.W., Acta Met., 7, 529, 534
(1959).
9. Liu, Y.C. and Aaronson, H.I., *ibid*, 18, 845 (1970).
10. Smith, R. and Bowles, J.S., Acta Met., 8, 405 (1960).
11. Hunt, A.M. and Pashley, D.W., Jne. Aust. Inst. Metals,
8, 61 (1963).
12. Cornelius, I. and Wayman, C.M., Acta Met., 22, 301
(1974).
13. Cornelius, I. and Wayman, C.M., *ibid*, 22, 291 (1974).
14. Aaronson, H.I. and Lorimer, G.W., *ibid*, 6, 1091 (1972).
15. Weatherly, G.C., Acta Met., 19, 181 (1971).
16. Baro, B. and Gleiter, H., Acta Met., 22, 141 (1974).
17. Laird, C. and Aaronson, H.I., Acta Met., 17, 505 (1969).
18. Kinsman, K.R., Eichen, E. and Aaronson, H.I., Met. Trans.,
6A, 303 (1975).

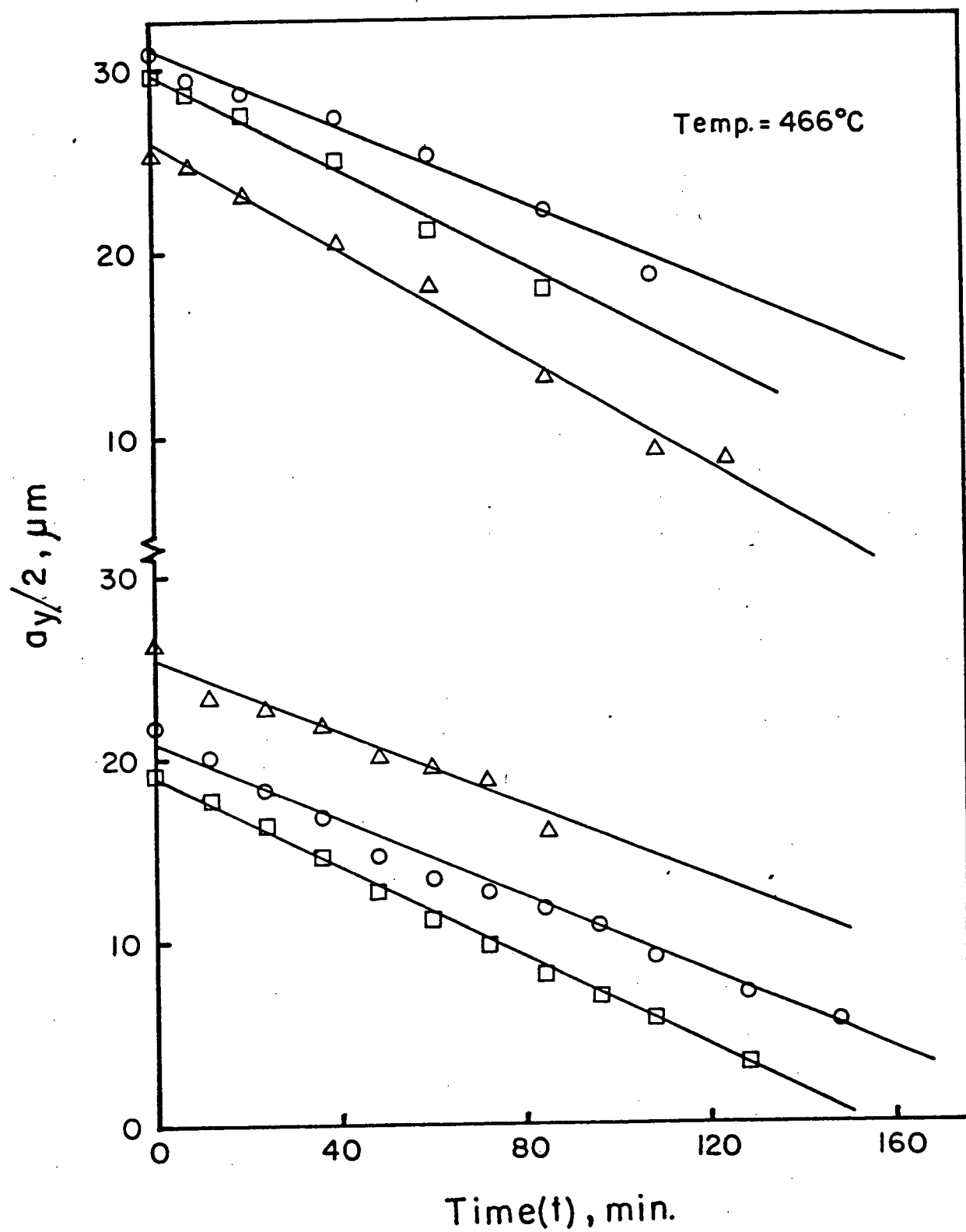
19. Eifert, J.R., Chatfield, D.A., Powell, G.W. and Spretnack, J.W., Trans A.I.M.E., 242, 66 (1968).
20. Hall, M.G., and Haworth, C.W., Acta Met., 18, 331 (1970).
21. Abbot, K. and Haworth, C.W., Acta Met., 21, 951 (1973).
22. Pabi, S.K., Mat. Sc. Eng., 43, 151 (1980).
23. Thomas, G., and Whelan, M.J., Phil. Mag., 6, 1103 (1961).
24. Simonen, E. P. and Trivedi, R., Report to U.S.A.E.C., Aug. 1972.
25. Aaronson, H.I., Lee, J.K., and Russel, K.C., Precipitation Processes in Solids (Ed. K.C. Russel and H.I. Aaronson) AIME, 31 (1976).
26. Kinsman, K.R., Eichen, E. and Aaronson, H.I., Met. Trans. 6A, 303 (1975).
27. Aaronson, H.I. and Laird, C. Trans. AIME, 242, 1437 (1968).
28. Kinsman, K.R., Aaronson, H.I. and Eichen, E., Met. Trans., 2, 1041 (1971).
29. Sankaran, R. and Laird, C., Acta Met., 22, 957 (1974).
30. Doherty, R.D., Ferrante, M. and Chen, Y.A., *ibid*, 11, 733 (1975).
31. Chen, Y.H. and Doherty, R.D., *ibid*, 11, 725 (1977).
32. Ferrante, M. and Doherty, R.D., Scripta Met., 10, 1059 (1976).
33. Aaronson, H.I., Clark, J.B., and Laird, C., Met. Sci. J., 2, 155 (1968).
34. Colby, J.W., Bell Laboratory Reports, 1973.
35. Heumann, Th., and Bohmer, H., J. Phys. Chem. Solids, 29, 237 (1968).
36. Beyeler, M., Maurice, F. and Seguin, R., Mem. Sci. Rev. Met., 67, No. 4, 295 (1970).
37. Kuzmenko, P.P. and Ostrovskii, L.F., Ukr. Fiz. Zhur, 6 525 (1961).

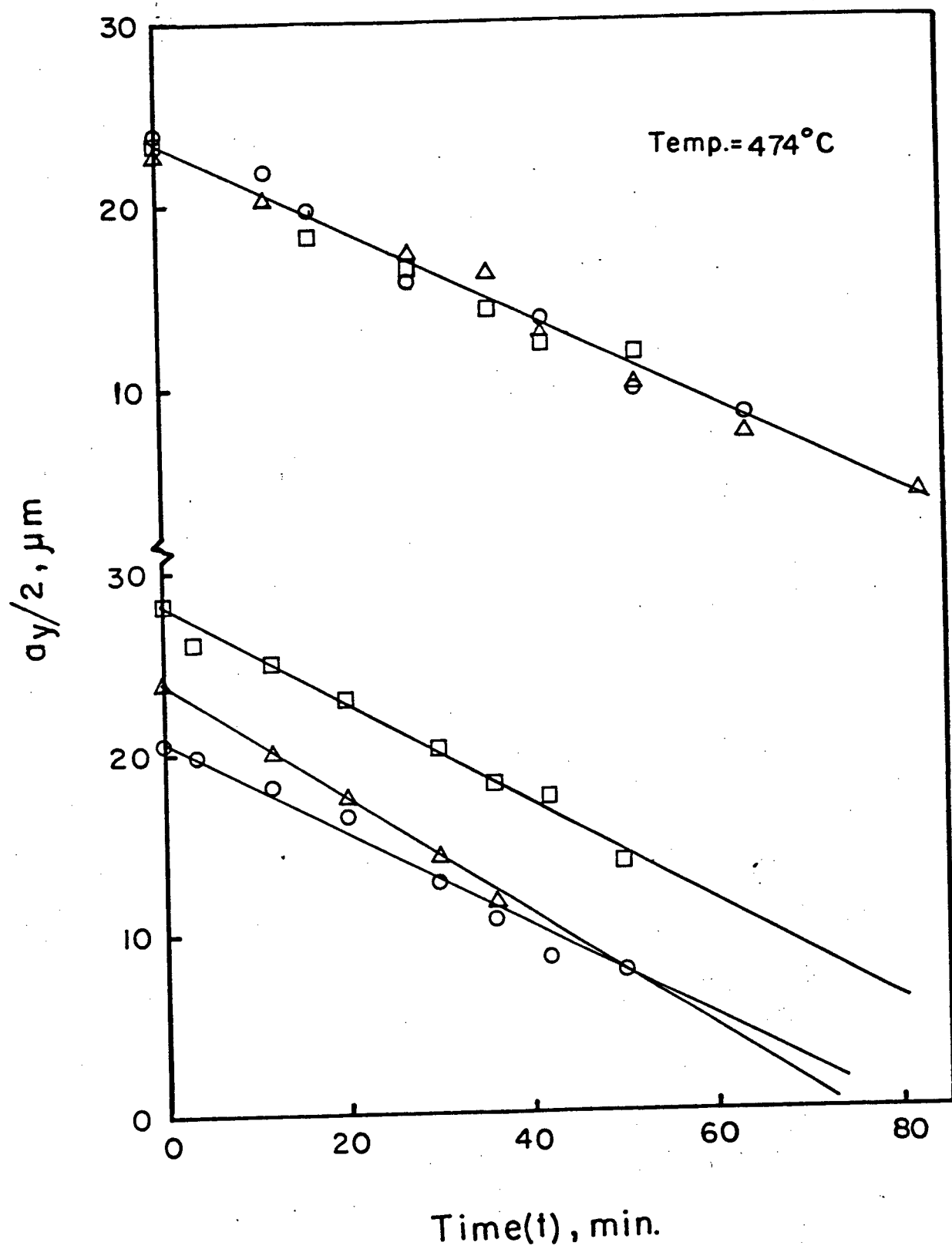
38. Repas, P.E. and Heheman, R.F., Tech. Rep. No. 6, Office of Naval Research, June, 1967.
39. Simonen, E.P. and Trivedi, R., Acta Met., 95, 273 (1973).
40. Simonen, E.P., Aaronson, H.I. and Trivedi, R., Met. Trans., 4, 1239 (1974).
41. Aaronson, H.I., Trans TMS-AIME, 224, 693 (1963).
42. Hall, M.G., Aaronson, H.I. and Kinsman, K.R., Surface Science, 31, 247 (1972).
43. Rigsbee, J.M. and Aaronson, H.I., Acta Met., 27, 365 (1979).
44. Aaronson, H.I., Jnl. of Microscopy, 102, 275 (1974).
45. Laird, C. and Aaronson, H.I., Acta Met., 15, 73 (1967).
46. Laird, C. and Aaronson, H.I., Jnl. Inst. Metals, 96, 222 (1968).
47. Pasparakis, A., Coates, D.E. and Brown, L.C., Acta Met., 21, 991 (1973).
48. Hansen, M., "Constitution of Binary Alloys" 2nd Ed., McGraw-Hill Book Co., N.Y. (1958), p.2.
49. Horvay, G., and Cahn, J.W., Acta Met., 9, 695 (1971).
50. Hillert, M., Jernkontorets Ann., 141, 757 (1957).
51. Jones, G.J. and Trivedi, R.K., J. App. Phys., 42, 4299, 1971.

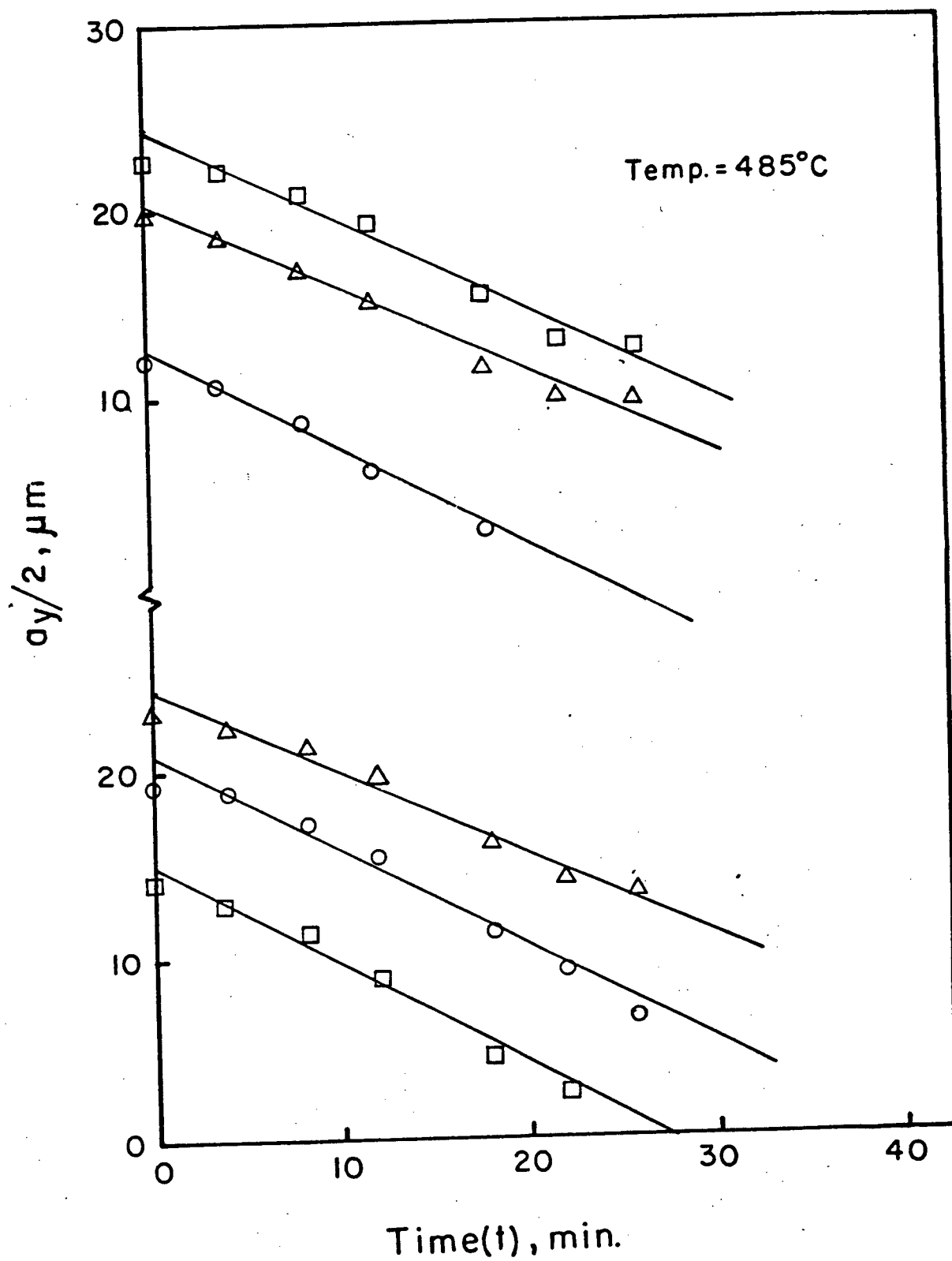
Appendix I

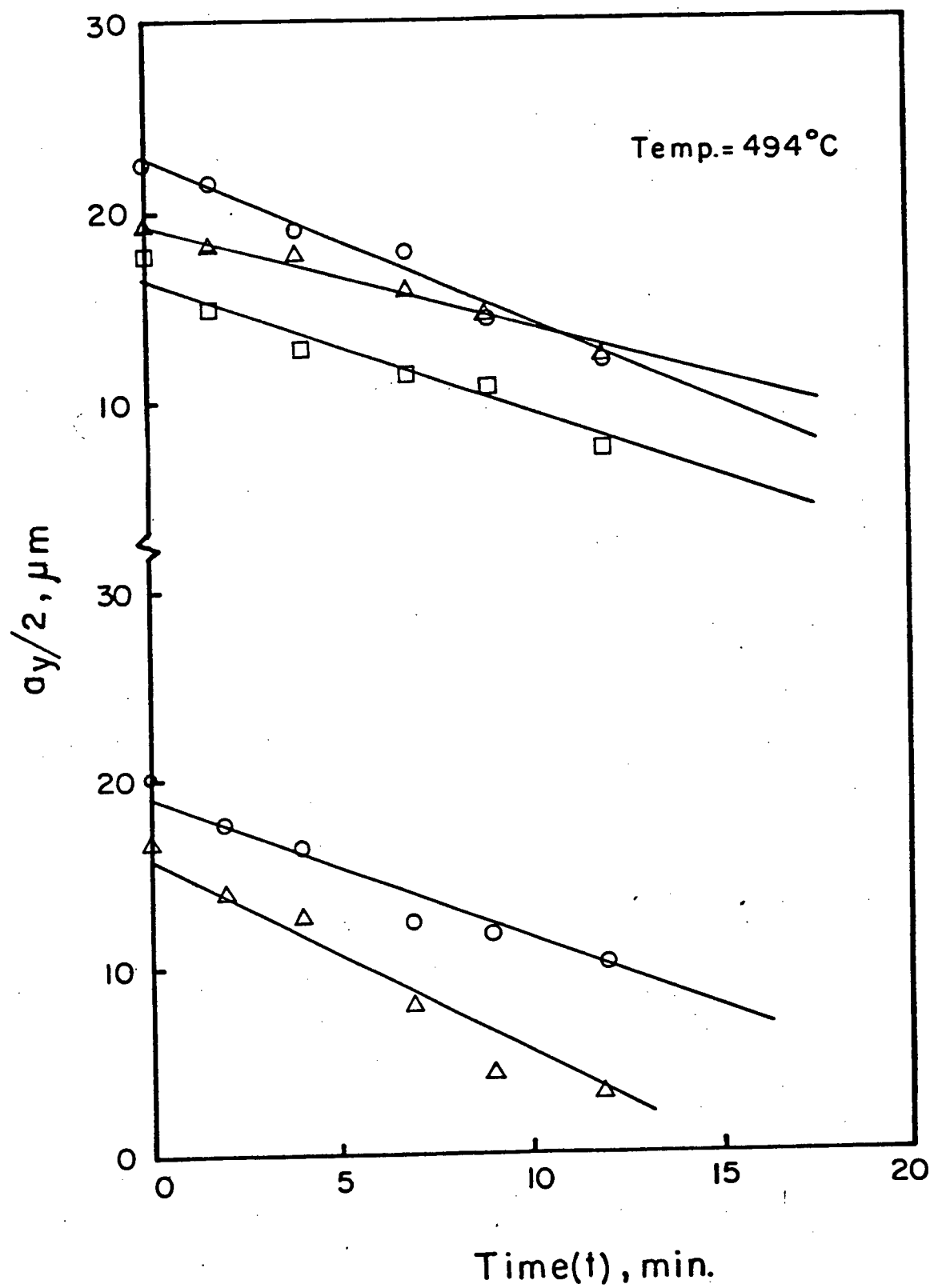
COMPILATION OF KINETIC RESULTS : SHORTENING





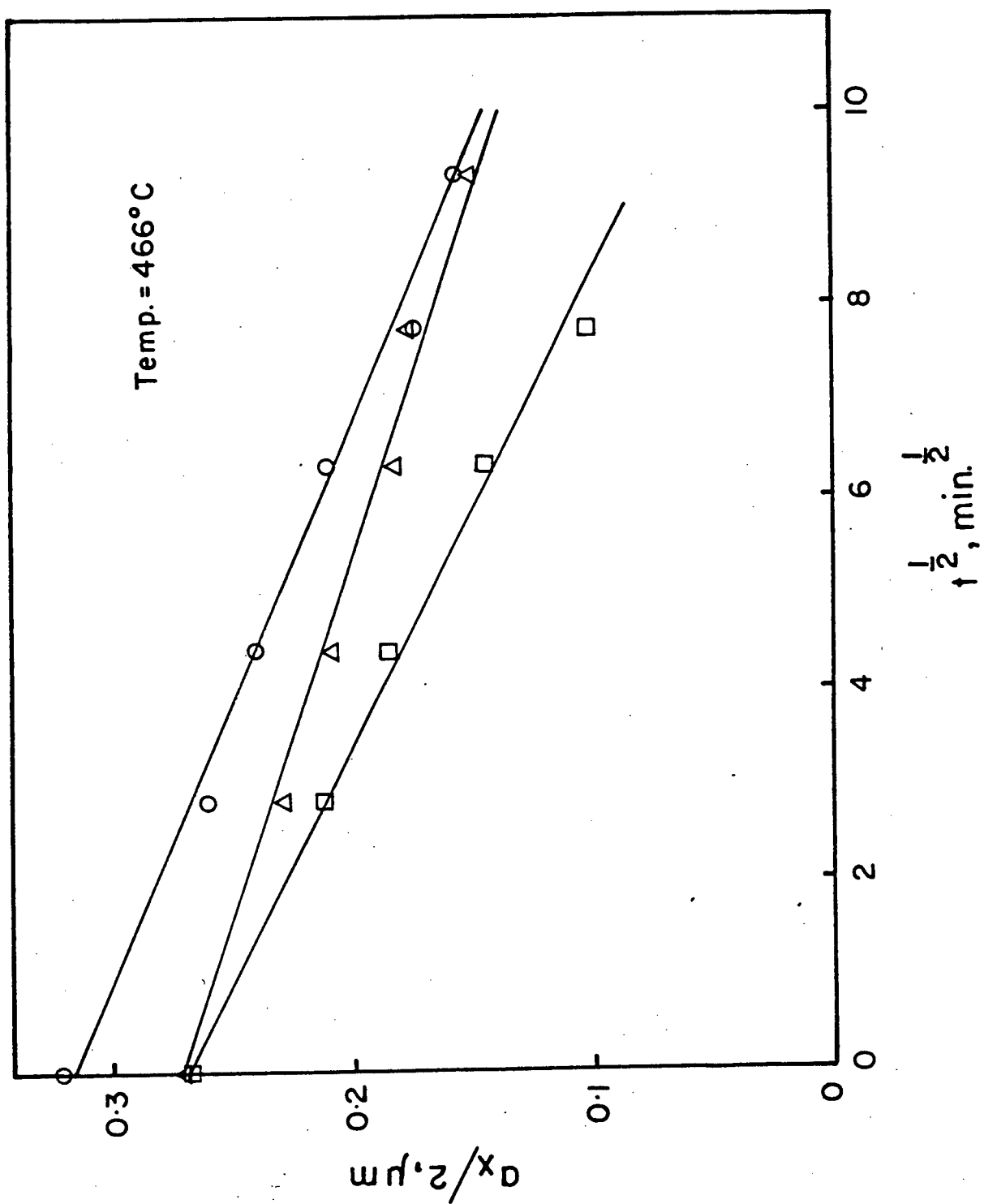


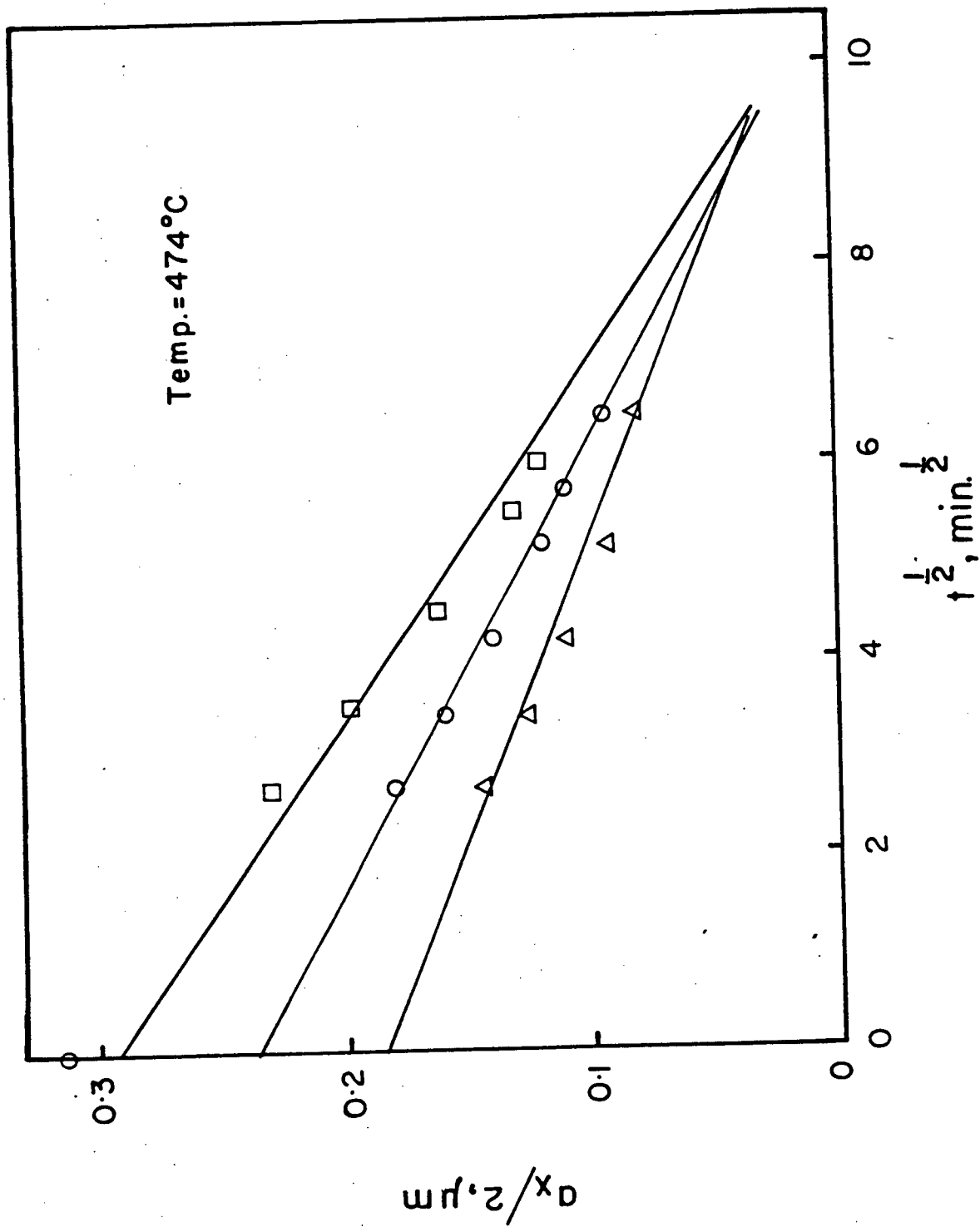


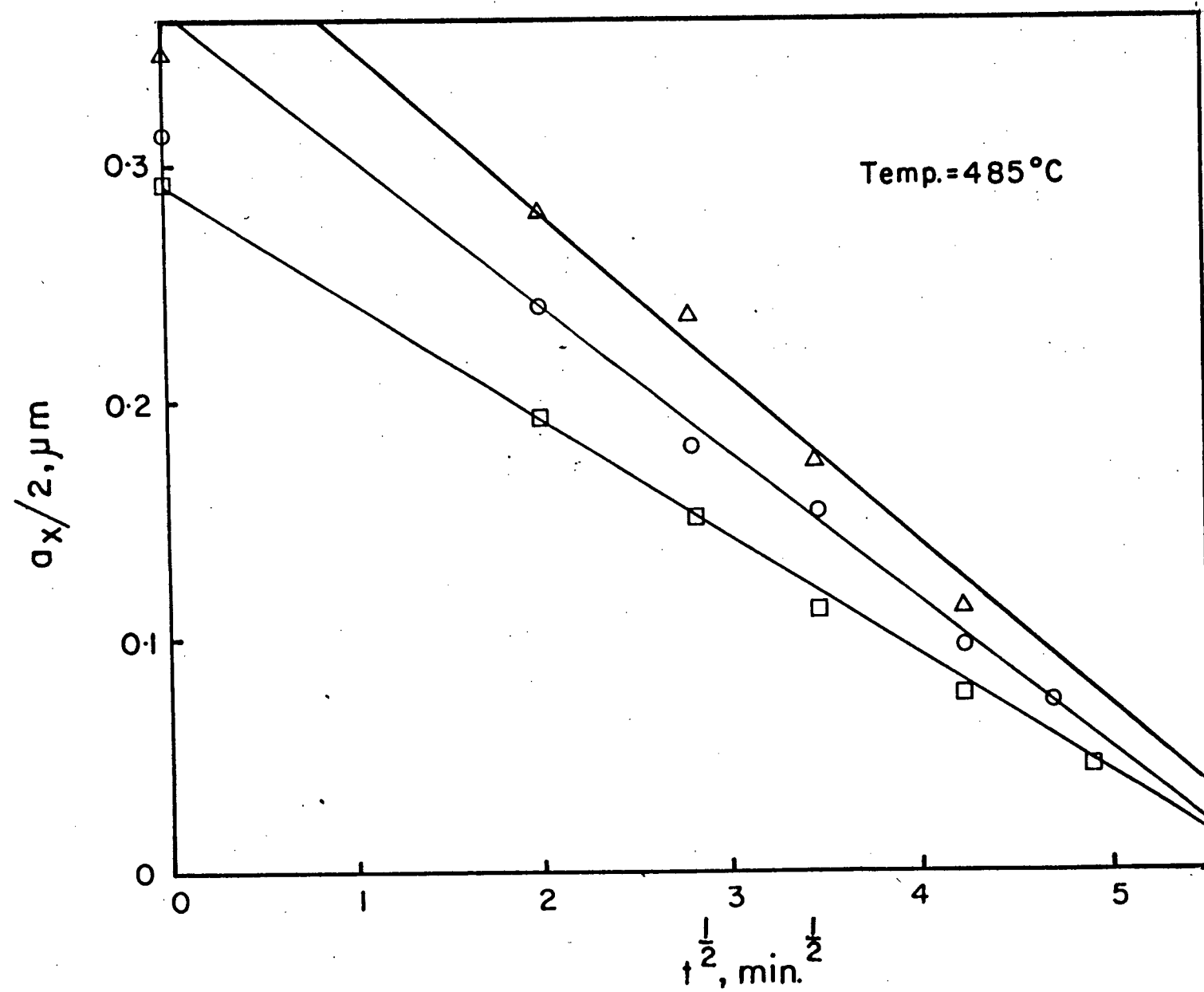


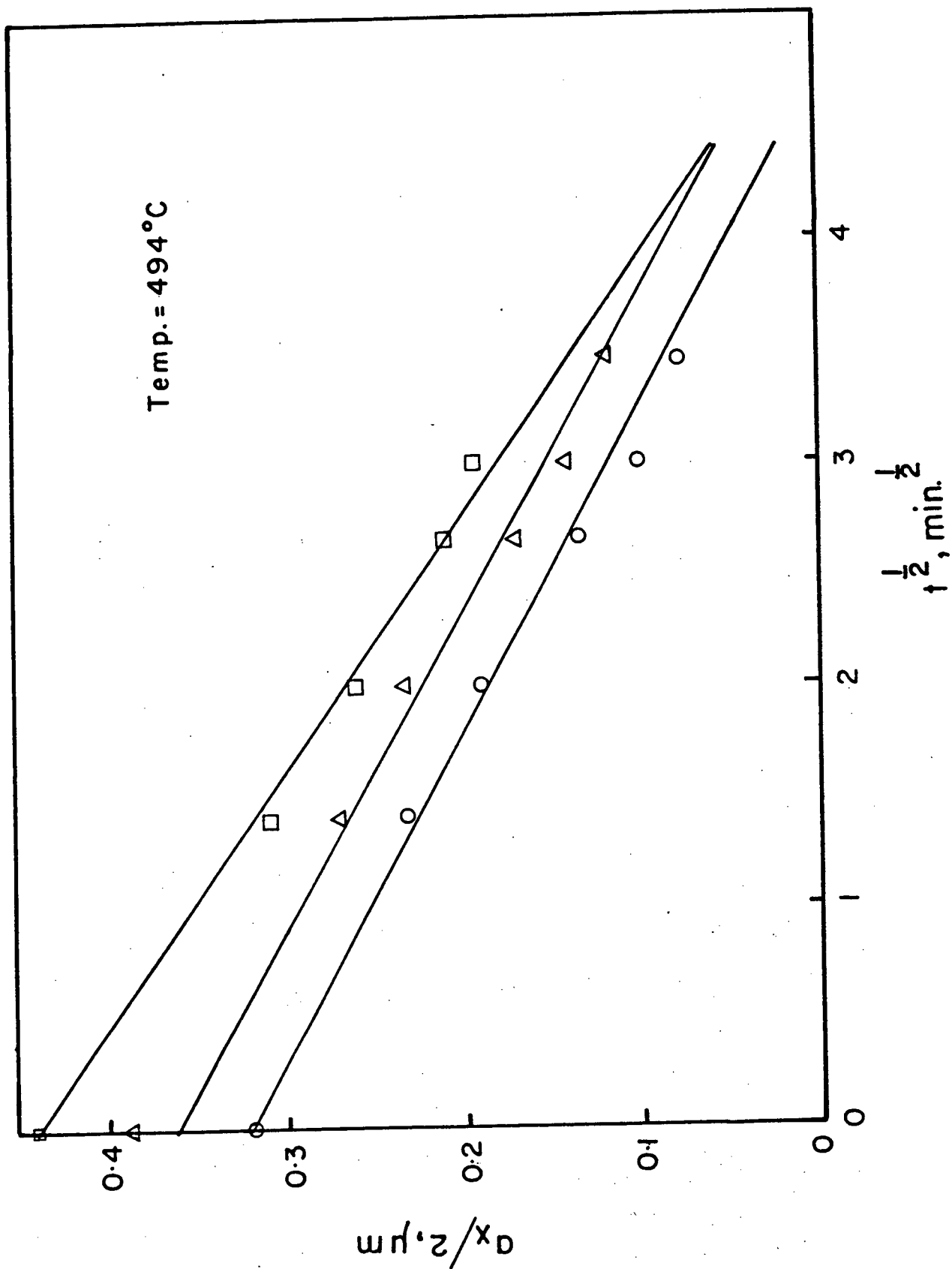
Appendix II

COMPILATION OF KINETIC RESULTS : THINNING









Appendix III

SOLUTE BALANCE CALCULATION

Appendix III

Overall Solute Balance Calculation

Fig. III-1 shows the schematic diagram of a dissolving precipitate solution treated at 485°C for 10 minutes used in the present calculation.

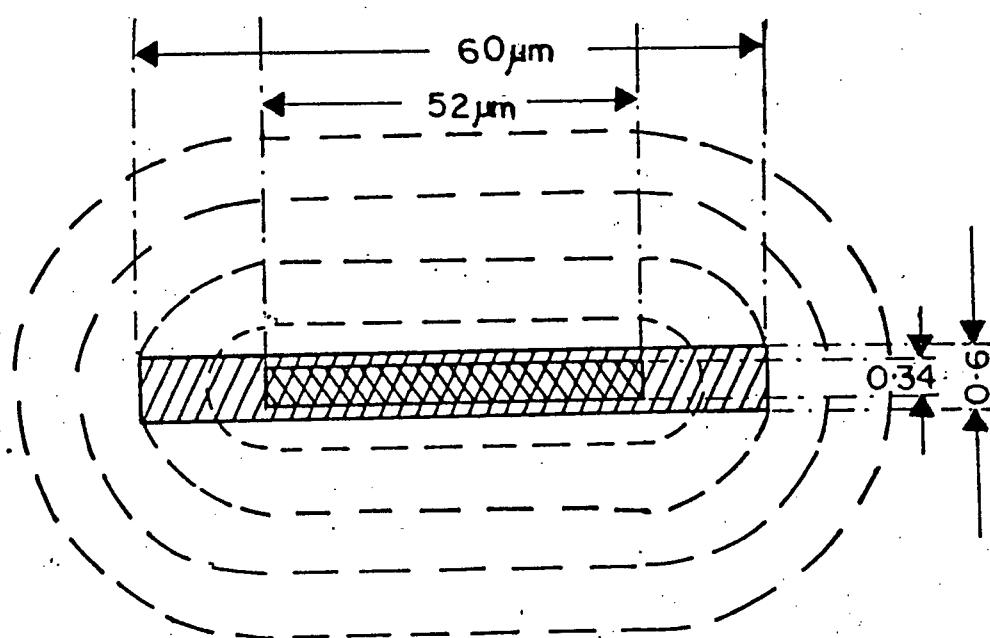


Fig. III-1. Schematic diagram of partially dissolved precipitate and surrounding solute distribution.

Amount of Solute Dissolved From Kinetic Data

The fractional change in precipitate dimension from the initial to the final size over the concentration range of

57 at.% Ag for the precipitate to a matrix concentration of 4.10 at.% Ag is:

$$[(52 \times 0.26) + (8 \times 0.47)] (57 - 4.10) = 914 \text{ at.\% } \mu^2$$

Amount of Solute in Solid Solution:

The amount of solute corresponding to the area under the concentration-distance profile, see Fig. III-2, was obtained by the Trapezoidal Rule at 10.8 μm at.%.

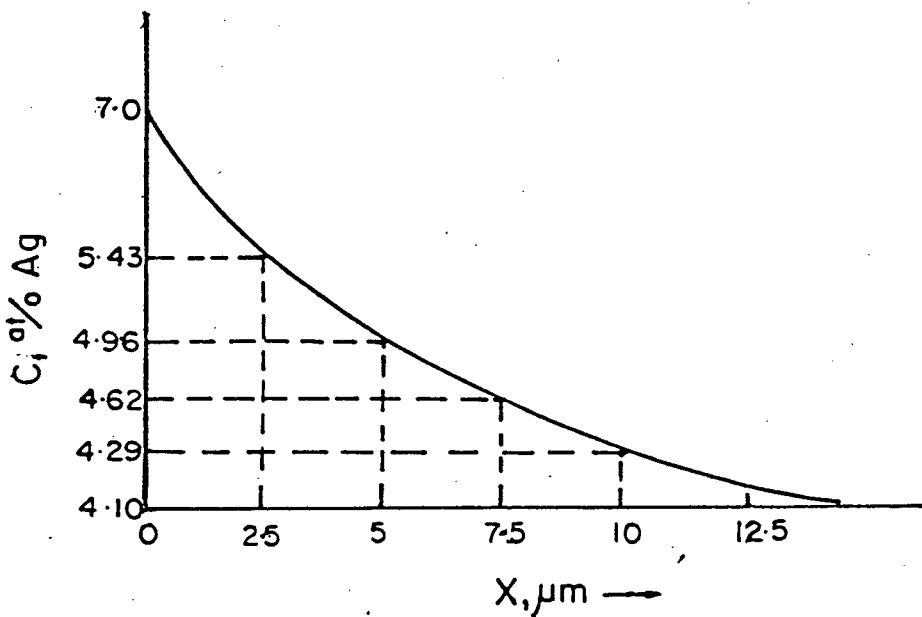


Fig. III-2 Schematic Diagram of solute distribution profile (485°C for 10 minutes).

Thus the solute from the flat face is equal to:

$$(10.8 \mu\text{m at.\%} \times 52.68 \mu) = 571 \text{ at.\% } \mu^2$$

Solute present at the corner was obtained by summing over the five sectors of Fig. III-3 as follows:

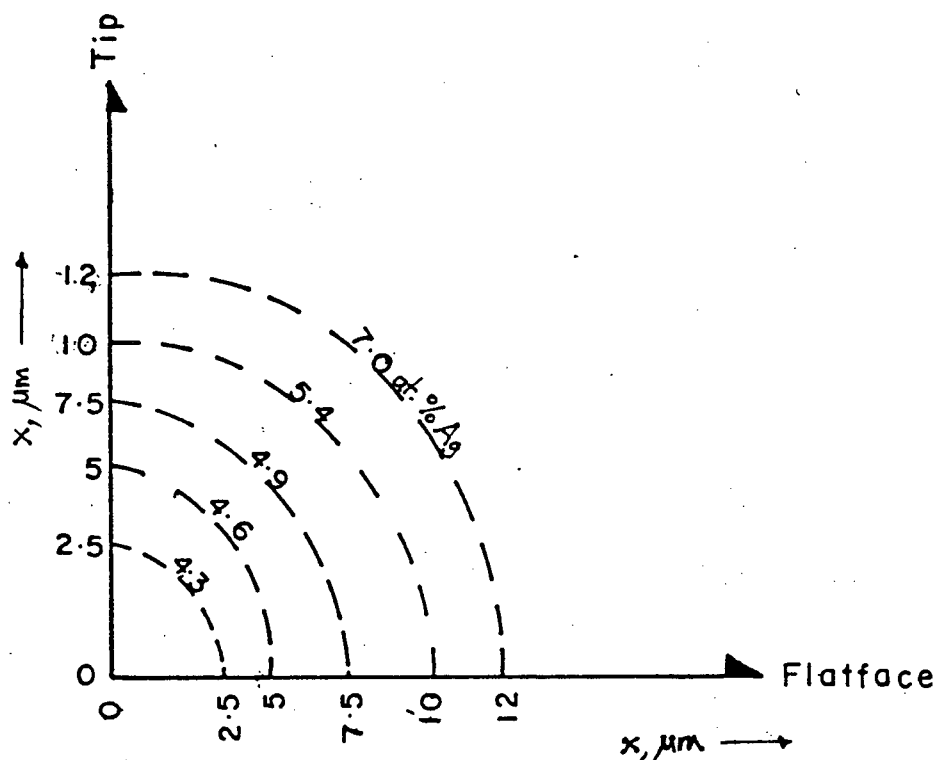


Fig. III-3 Solute distribution profiles representing the corners of Fig. III-1.

$$\begin{aligned} & \frac{\pi}{4} [92.5)^2 \times (7-5.43)] + [(5.0)^2 \times (5.43-4.96)] + \\ & [(7.5)^2 \times (4.96-4.62)] + [(10)^2 \times (4.63-4.26)] + \\ & [(12.5)^2 \times (4.29-4.10)] = 80.98 \text{ at.\% } \mu^2 \end{aligned}$$

For the total of four corners = 323.9 at.% μ^2 . Hence the total solute in solution equals;

$$(324 \text{ at.\% } \mu^2 + 571 \text{ at.\% } \mu^2) = 895 \text{ at.\% } \mu^2.$$

This is to be compared with the value of 914 at.% μ^2 obtained from the kinetic data. The difference is 2% which is within the uncertainty of the calculation.